SYSTEMS ANALYSIS IN MAMMALIAN CELL BIOMANUFACTURING - LINKING ENERGY METABOLISM AND GLYCOSYLATION

A DISSERTATION

SUBMITTED TO THE FACULTY OF THE

UNIVERSITY OF MINNESOTA

BY

Tung Sy Le

IN PARTIAL FULFILLMENT OF THE REQUIREMENTS

FOR THE DEGREE OF

DOCTOR OF PHILOSOPHY

Adviser: Professor Wei-Shou Hu

May 2018

ACKNOWLEDGMENT

First and foremost, I would like to express my deepest gratitude to my advisor, Professor Wei-Shou Hu for his tremendous support from the first day I came to the U.S. His patience and mentorship have been invaluable for both my academic and personal development.

I would like to thank my thesis committee members, Professor Prodromos Daoutidis, Professor Friedrich Srienc, and Professor Douglas Mashek for taking the time to serve on my committee and for their precious advice.

I would like to thank all members of the Hu lab: Kathryn Johnson, Nandita Vishwanathan, Ravali Raju, Liang Zhao, Kyongho Lee, Hsu-Yuan Fu, Haiyun Pei, Yonsil Park, Dong Seong Cho, Che-Chi Shu, Conor O'Brien, Hansol Kim, Sofie O'Brien, Jen One, Kevin Ortiz-Rivera, Meghan McCann, Zion Lee, Thu Phan and many others. You have made my life in Minnesota memorable. Thanks, David Chau for being a friend, in need. Your help since my very first day in the U.S is wholeheartedly appreciated. Thanks, Arpan Bandyopadhyay, for being a comrade with constant support. Thanks, Andrew Yongky for silently teaching me mathematical modeling, metabolism and many others. Thanks, Hyunki Kim for teaching me basic cell culture techniques. A special thanks to Huong Le for her great support in every step of the way during my Ph.D. study.

I also would like to thank other alumni of the Hu lab: Gargi Seth, Bhanu Mulukutla, Nitya Jacob, Siguang Sui, Katie Wlaschin, Patrick Hossler, Ziomara Gerdtzen Hakim, and many others, for sharing your Ph.D. experience with me.

I also would like to thank all of the undergraduate students that I worked with over the years: Guilherme Costa de Sousa, Edward Liu, and Alicia Zhang. I was inspired by the energy of your youth and by your inquisitiveness.

I would not come to this point without great support from the Vietnam Education Foundation. Thank you for providing me such an invaluable opportunity to study in the US, which has transformed my life.

Thanks, Van-Anh Do, Hien Nguyen, Khanh-Hoa Nguyen and many others in the USGuide community. Without your great encouragement and mentorship, I never would have thought that I am capable of pursuing graduate studies in the U.S. A special thanks to Hiep Nguyen for teaching me humility and being my “brother-in-arms”.

Thanks, my undergraduate research advisors in Hanoi University of Science and Technology, Professor Chau Phan and Professor Huong Tran, for your continued and enthusiastic support since I was a college student.

Finally, I would like to thank my family in Vietnam for their unconditional love since the day I was born. Thank you, Grandpa and Grandma, for teaching me the ancient wisdom of our country, without which I will not able to withstand challenges in my life. Thank you, my mother and my late father, for bringing me into the world and for nurturing me. Thanks, my little sister for your silent support in every step of my life.

DEDICATION

Dedicated to my beloved mother and

In memory of my late father.

ABSTRACT

Recombinant protein therapeutics have transformed modern medicine in the past decade and will continue to provide treatments for a wide range of life-threatening illnesses. Mammalian cells have been the major workhorse to produce therapeutic proteins owing to their capability to perform complex post-translation modifications that are essential to the pharmacological activities of these proteins. The performance of mammalian cell culture is greatly affected by cell metabolism, while the robustness of glycosylation patterns of the product proteins still needs improvement. A meta-analysis of cell culture bioprocess data revealed a correlation between lactate metabolism, productivity, and glycosylation patterns. Using the system biology approach that integrates computational modeling with transcriptomic resources, we explored different behaviors of energy metabolism and glycosylation in mammalian cells, contrived strategies for more robust control of cells physiology to achieve desired process outcomes.

In a continuous culture of mammalian cells, different steady states have been observed even under the same operating conditions. Some cultures reach a high glycolysis flux state whereas others reach a low flux state. The two steady states exhibit different cell concentrations. A multi-scale model was constructed, integrating the intracellular metabolism with macroscopic cell growth. Using the model, we demonstrate that multiple steady states exist in a certain range of dilution rate. At a high flux state, most of the glucose consumed is converted to lactate whereas, at a low flux state, glucose is mainly utilized for biomass synthesis. The difference in the steady state of glycolysis flux is marked by different cell concentrations due to their distinct metabolic efficiencies.

Cultured mammalian cells during growth consume glucose at a high rate and convert most of it to lactate. As the growth rate tapers, cells may switch to a state of low glucose consumption and low lactate production, some cells even start to consume lactate. Among cultures that have reduced lactate production, some may resume its high lactate production rate during the late stage of culture. Cultures with a switch-up from a low to a high lactate production state have been correlated with low productivity. The metabolic model is used to explain the mechanism behind this switch-up. We show that the switch-up behavior changes as the lactate and glucose concentration vary. Importantly, AMPK-mediated stress response also alters the switch-up behavior. Cells in culture may undertake a switch-up or not, depending on the concentrations of glucose and lactate and the stress level of the cells.

During hepatocyte differentiation, a metabolic switch from a high to a low glycolytic flux occurred. Using gene expression microarray data of stem cell-derived hepatocytes, we examine changes in the transcript levels of key glycolysis enzymes and incorporate such change to the kinetic model of energy metabolism in mammalian cells. Model predictions reveal the role of isoform levels of glycolysis isozymes in the switch of metabolism.

Obtaining proper and consistent glycosylation of the protein products is of high importance in cell culture process. It has been known that N-glycans affect the efficacy of protein therapeutics and mucin-type O-glycans influence the structure and stability of glycoproteins. The synthetic pathway of O-glycans involves a large number of enzymes whose expression pattern is cell specific. We develop an integrated platform to study the O-glycosylation network in a cell-specific fashion. The versatility of this platform can facilitate the development of strategies in glycoengineering.

TABLE OF CONTENTS

LIST OF TABLES

LIST OF FIGURES

LIST OF EQUATIONS

1 INTRODUCTION

1.1 MAMMALIAN CELL CULTURE

Recombinant protein therapeutics (also known as biologics) had a profound impact on modern medicine by providing innovative and effective treatments for a wide range of life-threatening diseases. These recombinant proteins are mainly produced in mammalian cells because of their capability to perform complex post-translation modifications that are essential to the pharmacological activities of the proteins. A number of mammalian cells have been used to produce biologics; among those, Chinese hamster ovary (CHO) cells are the major workhorse, accounting for nearly 70% of therapeutic proteins produced today.

The performance of mammalian cell culture is greatly affected by cell metabolism, while the robustness of glycosylation patterns of the product proteins still needs improvement. A meta-analysis of cell culture bioprocess data revealed a correlation between lactate metabolism, productivity, and glycosylation patterns. In this study, we use various modeling techniques to understand the behavior of cell metabolism and the O-glycosylation patterns of protein therapeutics. Mathematical modeling of energy metabolism of mammalian cells provides us with a more holistic understanding of the cell physiology and reveals the underlying mechanism of the somewhat erratic behavior of cell metabolism. In addition, we combined a rule-based network generator with a network visualization tool to explore the highly complex reaction network of O-glycan synthesis. Insights from the current study can be employed to devise strategies for robust control of cell physiology to achieve desired process outcomes.

1.2 SCOPE OF THESIS

This thesis research focuses on the development and application of mathematical modeling approaches to understanding the physiology of the cells. Two types of models were considered in the current study: a kinetic model and a rule-based model.

In the first part of the thesis, we focus on explaining the mechanism behind the steady state multiplicity in continuous culture. Besides fed-batch culture, continuous culture is another cultivation method practiced in the industry. In continuous culture, nutrients are fed continuously to the culture and the reactor content is withdrawn at the same rate. The working volume of reactor thus remains constant throughout the culture. Under seemingly identical operating conditions, some cultures reside at a high glycolysis flux state whereas some others reside at a low glycolysis flux state. Different metabolic states of glycolysis lead to distinct outcomes of the culture. At a high flux state, most of the glucose consumed is converted to lactate, leading to a low cell concentration and thus low productivity. At a low flux state, most of the glucose consumed is utilized for biomass synthesis, which results in high cell concentration and high productivity. Understanding the conditions at which culture can be steered towards a desired steady state is of high interest. In this section, we develop a multi-scale model that links the intracellular metabolism with macroscopic cell growth in the reactor and use the model to explain the nature of multiple steady states in continuous culture.

The second part of this thesis is devoted to conceiving the mechanism of a somewhat erratic behavior of glucose metabolism in the fed-batch culture of mammalian cells. Fed-batch culture is the prevailing method for cell cultivation. In fed-batch cultures, glucose is regularly added to the medium to sustain its concentration within a certain range. During

growth, cells consume glucose at a high rate and convert the majority of glucose consumed to lactate. Once the growth phase is over, lactate production rate may vary; some cultures have a transition to a state of low lactate production or even start to consume lactate whereas others continue to produce lactate towards the end. Among cultures that have a reduced lactate production rate, some resume high lactate production after a period of time. Cultures that exhibit metabolic switch from low to high lactate production have been correlated with decreased viability and low productivity [1, 2]. The diversity of metabolic switches discussed above has been observed even for the same cell line, under seemingly identical culture conditions and using the same standard operating protocol. The underlying mechanism of such metabolic switches has been of interest for decades yet not well understood. We have previously studied the mechanism of a switch from lactate production to lactate consumption [3]. In this study, we aim at identifying the mechanism of the other switch in which cell changes from a low to a high lactate production state. Insights from this study will help contrive strategies for robust control of metabolism and prevent an unfavorable switch from occurring.

In the third part of this thesis, we demonstrate the mechanism of a switch in glucose metabolism occurred during hepatocyte differentiation from human embryonic stem cells (hESCs). Using gene expression microarray data of stem cell-derived hepatocytes, we examine changes in the transcript levels of key glycolysis enzymes and incorporate such change to the kinetic model of energy metabolism in mammalian cells. Using this model, we reveal the potential association between the levels of glycolysis isozymes and the behavior of glycolysis flux during differentiation.

In the final part of this thesis, we focus on studying the mucin-type O-glycosylation network. Obtaining proper and consistent glycosylation of the protein products is of high importance in cell culture process. N-glycans have been known to affect the biologics efficacy; mucin-type O-glycans, on the other hand, have profound effects on the structure and stability of glycoproteins. The synthetic pathway of O-glycans involves a large number of enzymes with diverse substrate specificity. The expression pattern of these enzymes is cell specific, thus making the pathway highly diverse. To facilitate the analysis of the pathway in a cell-specific fashion, we develop an integrated platform of a rule input network generator and a network visualization program. We use the platform to generate the O-glycosylation networks of different cell lines, compare the predicted network with the reported O-glycan profiles of the same cell lines, and then predict the synthetic route for each reported glycan species. The versatility of this platform in projecting the network and tracing the reaction path can facilitate the development of strategies in glycoengineering.

1.3 THESIS ORGANIZATION

This thesis is organized into five chapters. Chapter 2 focuses on development and application of a multi-scale kinetic model to the analysis of multiple steady states in continuous culture of mammalian cells. The multiple steady states behavior of glycolysis flux is exploited to devise strategies to guide cells towards the desired flux state with higher cell concentration. Chapter 3 examines the mechanism of the metabolic switch to high lactate production in fed-batch cultures of mammalian cells. We also investigated the important parameters for stimulating the switch. Chapter 4 discusses the effect of isoform composition of key glycolysis enzymes on the glycolysis activity. Chapter 5 presents an

integrated platform for generation and visualization of the O-glycosylation network. Finally, chapter 6 provides a brief conclusion of this study and future directions.

2 MECHANISM FOR MULTIPLICITY OF STEADY STATES WITH DISTINCT CELL CONCENTRATION IN CONTINUOUS CULTURE OF MAMMALIAN CELLS

Reproduced from: Yongky A, Lee J, Le T, Mulukutla BC, Daoutidis P, Hu WS, *Mechanism for multiplicity of steady states with distinct cell concentration in continuous culture of mammalian cells.* Biotechnology and Bioengineering, 2015. **112**(7): p. 1437-1445.

TL constructed the ODE model. AY derived the algebraic model from the ODE model. AY and TL performed simulations and analyzed the results.

2.1 SUMMARY

Continuous culture for the production of recombinant proteins enables steady state operations, which provides more consistent product quality and increased productivity. The multiplicity of steady states has been observed in continuous cultures of mammalian cells. With the same dilution rate and feed nutrient composition, steady states with very different cell and product concentrations may be reached; in a high glycolysis flux state, cells produce lactate with a high specific rate and have low cell concentration, whereas cells at a low flux state have a lower rate of lactate production and higher cell concentration. These different steady states also have different productivity. A mechanistic understanding of the multiple steady states behavior in continuous culture facilitate the development of strategies to guide the culture toward the desired steady state. We established a multi-scale kinetic model that links the intracellular metabolism with the cultivation conditions in a continuous bioreactor. We showed that the bistable behavior of glycolysis flux leads to the

occurrence of steady state multiplicity in a range of dilution rate. The model was also used to devise strategies to steer the culture toward the desired steady state.

2.2 INTRODUCTION

Mammalian cells are the predominant host cells for the production of therapeutic recombinant proteins. In the past three decades, fed-batch culture, wherein feed containing nutrients are regularly added to the culture to replenish those consumed to sustain longer cell growth and production period, has become the prevailing form of process. While the continuous process has been explored as a process technology and for kinetic studies of cell growth and metabolism [4-13], its industrial applications are mostly in the case that the product is labile or is produced at a rather low concentration, such as Factor VIII and Protein C.

Continuous cell culture processes operated at steady states allow a stable cell concentration and productivity to be sustained in the reactor for an extended period. The increased productivity also allows a small manufacturing facility to be used. In addition, continuous cell culture processes offer the advantage of a steady state operation, where none of the parameters such as the concentrations and rates of glucose, lactate and cell changes throughout time. Such steady state operation possibly enables a better control of the cells' physiological state, thereby enhancing our ability to control product quality. Because of this potential benefit and the increasing emphasis on product quality in biopharmaceutical processes, there has been increasing interest in exploring continuous culture for mammalian cell culture [14].

However, the growth and metabolic behavior of mammalian cells differ significantly from those of most microbial cells. The growth of microorganisms can often be adequately

described by a Monod growth model and be shown experimentally to have a unique steady state where the concentration of cells, nutrients and other process parameters such as growth and metabolic rates all reach a unique set of steady state values under a set of nutrient input conditions and at a fixed dilution rate. In contrast, under identical operating conditions, mammalian cells can metabolize glucose differently depending on their physiological states. Such capability was demonstrated in the form of a metabolic shift of glucose catabolism in many types of cultured cells [15, 16]. Under those different metabolic states, cells may consume glucose at a high rate and convert a large proportion of glucose to lactate or consume glucose at a low rate and produce little lactate. The metabolic shift resulted in a lower proportion of carbon sources being directed toward lactate, redirecting more carbon sources to cell growth. Through the control of glucose at low levels to shift cell metabolism prior to the initiation of continuous culture, the culture reached a steady state with higher cell concentration compared to the culture started from batch mode without alteration in cell metabolism [17, 18]. Those continuous cultures reached distinct steady state marked by distinct cell concentration, even though the feed and operating dilution rate were the same, thus suggesting the existence of steady state multiplicity. Similar demonstrations of steady state multiplicity in continuous culture were reported in other studies [19, 20].

This steady state multiplicity was experimentally attained by exploiting the plurality of the flux of glycolysis observed in cultured cells. The cause of steady state multiplicity and the range of conditions that multiplicity exists were not known. Those multiple steady states are marked not only by different glycolysis fluxes but also by different cell concentrations and thus the productivity. The ability to control the culture to consistently reach the desired

steady state, usually the one with higher cell concentration, will be critical for production processes. Therefore, a better understanding of the root cause of such steady state multiplicity and ways to control the culture trajectory is essential.

We have previously shown that steady state multiplicity exists in the glycolysis of mammalian cells as a result of the feedback and feed-forward regulations imparted by the set of isozymes they express [21]. The glycolysis flux increases with increasing extracellular glucose concentration as in most metabolic pathways, but in a range of glucose concentrations, multiple steady states exist for a given glucose concentration. In the bistable region, the glycolysis flux may be at either a high flux state or a low flux state. In the late growth phase of a fed-batch culture, the culture can transit from a high flux state to a low flux state as a result of reduced AKT activation due to slower growth rate and lactate inhibition of glycolysis [3]. The glycolysis behavior predicted by the metabolic model is supported by experimental observations in fed-batch cultures and in continuous cultures, providing a mechanistic foundation for the metabolic shift.

In this study, we constructed a multi-scale model that integrates the intracellular metabolic model with the macroscopic cell growth model in a continuous bioreactor. Through model simulations, we show that multiplicity of steady states is present in a range of dilution rates in continuous culture and demonstrate the trajectory that one can employ to guide the culture to the desired steady state.

2.3 MATERIALS AND METHODS

2.3.1 Multi-Scale Model

A kinetic metabolic model of mammalian metabolism including glycolysis, pentose phosphate pathway (PPP), tricarboxylic acid (TCA) cycle, malate-aspartate shuttle pathway and citrate shuttle between the cytosolic and the mitochondrial compartments was constructed as described previously [3, 21]. The rate expressions for all enzymatic reactions were based on mechanistic derivation [22, 23]. The allosteric regulations of the enzymes phosphofructokinase (PFK), pyruvate kinase (PK) and 6-phosphofructo-2-kinase/fructose-2,6-bisphosphatase (PFKFB) have been considered in detail based on the Monod-Wyman-Changeaux method [24]. For cases where multiple isozymes are expressed in the mouse-mouse hybridoma cell line, MAK, the dominant form based on microarray data [25] namely the muscle isoform of PFK (PFKM), the M2 isoform of PK (PKM2) and PFKFB3 isoform of PFKFB, were considered. In this study, the model was extended to include the macroscopic cell growth and mass balances for extracellular glucose and lactate in the reactor in a continuous operation (Figure 1)

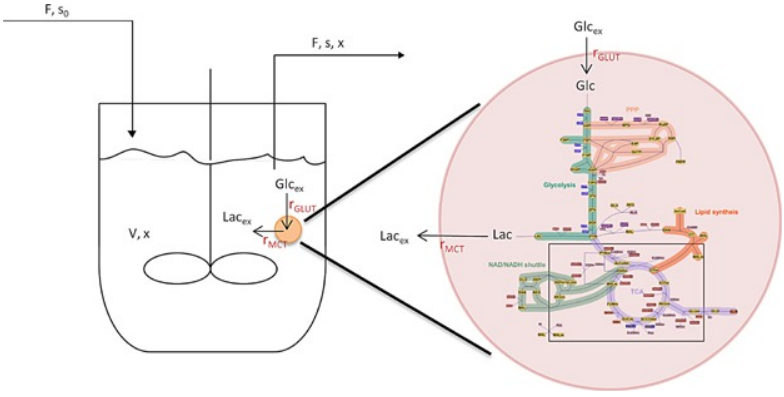

Figure 1. Schematic of the multi-scale model.
The model takes into account the intracellular metabolism of the cell and substrate utilization for macroscopic cell growth in the reactor. Notations: V, reactor volume; F, volumetric flowrate; Glc_{ex}, glucose; Lac_{ex}, lactate; x, cell concentration.

The multi-scale ordinary differential equation (ODE) model consists of mass balance equations for 37 reaction intermediates of the intracellular metabolism as well as three macroscopic mass balance equations. The rate expressions for the intracellular enzyme kinetics and the differential equations for those intracellular metabolic intermediates have been described previously [3, 21]. The equations describing macroscopic cell growth, glucose and lactate concentrations in the bioreactor are as follow:

Equation 1. The rate of change of extracellular glucose concentration.

$$\frac{dGlc_{ex}}{dt} = D(Glc_{feed} - Glc_{ex}) - r_{GLUT} \times x$$

Equation 2. The rate of change of extracellular lactate concentration.

$$\frac{dLac_{ex}}{dt} = -D \times Lac_{ex} + r_{MCT} \times x$$

Equation 3. The rate of change of cell concentration.

$$\frac{dx}{dt} = (\mu - \mathrm{D}) \times x$$

Equation 4. The specific growth rate of the cells.

$$\mu = \mu_{\max} \times \frac{Glc_{ex}}{K_{m,Glc} + Glc_{ex}} \times \frac{K_{i,Lac}}{K_{i,Lac} + \left(Lac_{ex}\right)^2}$$

The reactor balance model shown above is linked to the intracellular metabolic model through the rates of consumption of glucose (r_{GLUT}) and production of lactate (r_{MCT}). r_{MCT} and r_{GLUT} (i.e the glycolysis flux) are related to the concentrations of glucose (Glc_{ex}) and lactate (Lac_{ex}). The specific growth rate of the cells is assumed to follow Monod type kinetics with respect to glucose concentration and an inhibitory effect of lactate in Equation 4 as described previously [26]. Thus, the cell growth rate is indirectly affected by the

intracellular metabolism through glucose and lactate. One of the major determinants of the rate of intracellular metabolism is the AKT signaling pathway activity which modulates the kinase-to-phosphatase ratio (K/P) of the PFKFB [27-29]. AKT phosphorylation of PFKFB positively affects the rate of glycolysis. AKT activity is correlated to the growth rate of the cells. However, for the range of dilution rates considered in this study, the growth rate is high and AKT is assumed to be fully active in all dilution rates.

2.3.2 Model Simulation

An algebraic model comprising of steady state mass balance equations for the cell concentration, extracellular glucose and lactate concentrations and all the intracellular metabolites concentrations was derived from the multi-scale ODE model. The steady state solutions were obtained from the algebraic model using numerical solver *fsolve* in Matlab (Mathworks, Inc.). Positive and real-valued solutions were calculated using initial guesses, which were pseudorandom values drawn from the standard uniform distribution. All the possible steady states and the corresponding eigenvalues were calculated initially at fixed feed glucose concentration of $5\,\mathrm{mM}$ and dilution rate of $0.033\,\mathrm{h}^{-1}$. The feed glucose concentration and dilution rate were then expanded to find other steady state conditions. The steady state concentrations of the cell and all metabolites were examined to ensure they are within the same order of magnitude as the physiological range. The local stability of a steady state was investigated using the standard approach of calculating the eigenvalues of the Jacobian evaluated at the steady state. The Jacobian matrix was calculated as part of the output of Matlab's *fsolve* function. The eigenvalues of the Jacobian matrix were evaluated using Matlab's *eig* function. If all the eigenvalues have a negative real part, the steady state is stable, if not it is unstable.

Transient simulations of the ODE model were performed using the implicit numerical ODE solver *ode15* in Matlab (Mathworks, Inc). Initial cell and lactate concentrations were 1.5×10^5 cells/mL and 0 mM, respectively. For the batch culture simulation, the dilution rate was set to zero and the initial glucose concentration used was 15 mM. For the fed-batch culture, the dilution rate was set to zero and the extracellular glucose concentration was fixed at 0.5 mM by setting the right-hand side of the differential equation for extracellular glucose Equation 1 to zero. Upon switching to continuous mode, the dilution rate was set at $0.033\ h^{-1}$ and the feed glucose concentration was 7 mM. Changes in the extracellular concentrations of glucose, lactate, and cell and the intracellular concentrations of all metabolites were followed.

2.4 RESULTS

2.4.1 Multiplicity of Steady States in Continuous Culture

The multi-scale model was used to first simulate the steady state reached in continuous culture. Figure 2 depicts the steady state concentrations of cells, glucose, and lactate as well as the fluxes (i.e. specific consumption rate) of glucose and lactate at different dilution rates. The glucose concentration in the feed was fixed at 5 mM (Figure 2A–C). The figures show classical bistable behavior where two stable metabolic steady states exist in the dilution rate ranging from 0.029 to $0.039\ h^{-1}$. The middle steady states are unstable and cannot be realized in the culture. The glucose flux and lactate flux data in the bistable region indicate that a set of stable steady states corresponds to high flux state and the other set correspond to low flux state. At high flux states, glucose is mostly converted towards lactate as indicated by the ratio of lactate flux and glucose flux into glycolysis (J_L/J_G) which is in the range of 1.45-1.6 mol/mol. In contrast, the low flux states have (J_L/J_G)

<0.8 mol/mol. In addition, the high flux states have lower cell concentrations and higher lactate levels, while the low flux states have higher cell concentrations and lower lactate levels. Thus, glucose is more efficiently metabolized to support cell proliferation at low flux states. Outside of the bistable region, only one steady state exists for a given dilution rate: at dilution rate <0.029 h^{-1} only the low metabolic flux state (high cell concentration) exists whereas at dilution rate >0.039 h^{-1} only the high metabolic flux state (low cell concentration) exists.

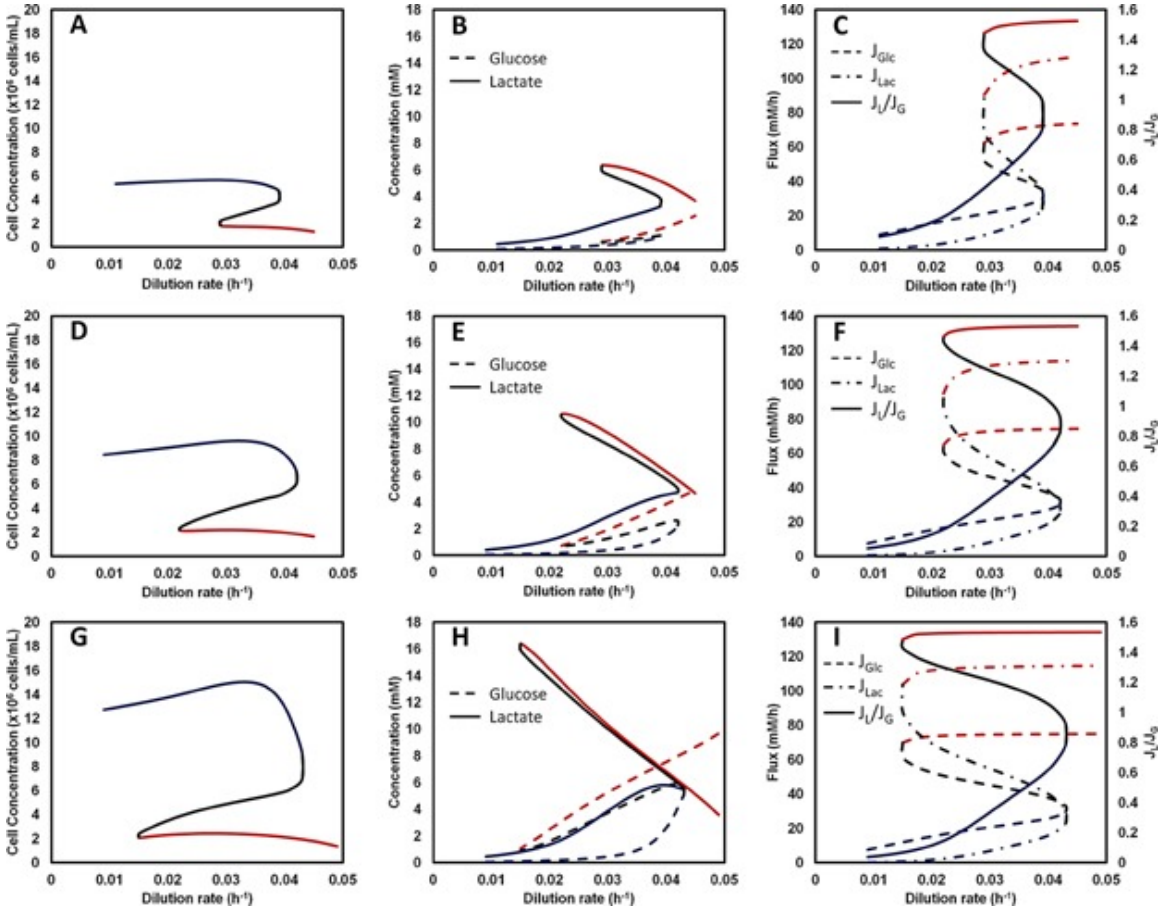

Figure 2. Multiple steady states in continuous culture.
Bistability is observed in the profiles of cell concentration (A, D, G), extracellular concentrations of glucose and lactate (B, E, H), rates of glucose consumption and lactate production and the ratio of the two rates(C, F, I). Feed glucose concentration was 5 mM (A-C), 8 mM (D-F) and 12 mM (G-I), respectively. The steady states corresponding to low metabolic flux are in blue, while those corresponding to the high metabolic flux are in red.

The unstable steady states are in black. Note that the steady states with low metabolic flux confer high cell concentration and vice versa.

The effect of increasing the feed glucose concentration on the steady state behavior was then investigated by varying the feed glucose concentrations from 5 mM to 8 mM (Figure 2D–F) and 12 mM (Figure 2G–I), respectively. At a low flux steady state increasing feed glucose concentration gives rise to a higher steady state cell concentrations as well as somewhat elevated residual glucose and lactate concentrations (comparing Figure 2B,E,H), although the extent of cell concentration increase diminishes somewhat at the high dilution rate region at a feed glucose concentration of 12 mM. This is due to the higher levels of residual glucose concentration (thus lower amounts of glucose taken up by cells) at those steady states. In contrast, increasing feed glucose concentration at high flux states does not increase the cell concentration substantially, rather the residual lactate concentration increases significantly. At the low feed glucose concentration of 5 mM, the high flux state extends only to a dilution rate of 0.029 h^{-1}, below that only the low flux state is observed. Whereas at higher feed glucose concentrations the high flux metabolic steady states reach into lower dilution rate range.

2.4.2 Effect of Feed Lactate on Steady State

Consumption of lactate typically occurs in the late stage of fed-batch cultures. It happens when the glycolysis flux is low [30]. In continuous culture, while steady states with low lactate production rate are possible under normal feed condition as seen above, steady states with lactate consumption do not occur unless lactate is present in the feed.

The steady state profiles of continuous cultures with a feed glucose concentration of 5 mM and lactate supplemented at 2 mM and 5 mM are shown in Figure 3. In both cases, lactate consumption only occurs at dilution rate <0.021 h^{-1}. Glucose is still being consumed even

when lactate consumption occurs at dilution rate <0.021 h^{-1}, resulting in negative values for J_L/J_G ratio (Figure 3C&F). In this range of dilution rate in which lactate consumption is observed, cell concentration is hardly affected compared to the case of no lactate supplementation (Figure 2A). In the lactate consumption state a significant residual lactate concentration is present in order to drive lactate uptake by cells; thus the net amount of lactate consumed is too small to substantially change cell concentration.

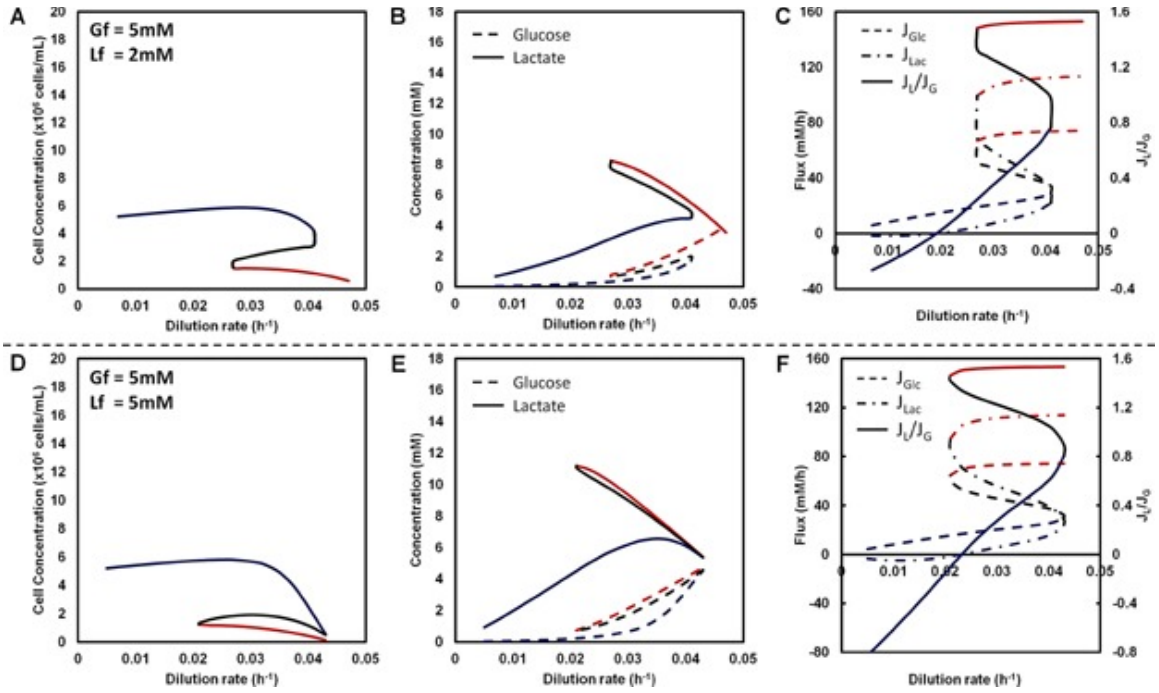

Figure 3. Effect of feed lactate on the bistable behavior in continuous culture.
Lactate concentration in the feed was 2 mM (A-C) and 5 mM (D-F), respectively. Lactate is consumed only at dilution rate <0.021 h^{-1}.

2.4.3 Trajectory to Steady State in Continuous Culture

We next ask the question of how to direct a continuous culture to a different steady state in the bistable region. The key is to "guide" cells to the desired flux state before it reaches the steady state. For increasing the productivity, the desired steady state is the low flux state with a higher cell concentration compared to the high flux state. In a batch culture of

mammalian cells the default steady state is always the high flux state as cells in culture, without intervention, always consume glucose at a high rate and convert a large portion of glucose to lactate. To "guide" the system toward a low flux steady state in continuous culture, one strategy is to first culture them in fed-batch with glucose maintained at low concentration. Such strategy allows the culture to move to a region in which only the low flux state exists (Appendix Figure 1). Once the metabolic state is in a low flux state, one can switch the culture to a continuous mode.

This scenario is illustrated by two simulated cultures: in one case a batch culture is switched to a continuous mode without guiding cells to a low flux state; in the other, a low glucose concentration is imposed in fed-batch culture to first guide cells to a low flux state (Fig. 4). The initial conditions used are 1.5×10^5 cells/mL and 0 mM lactate in both cases. Upon switching to continuous mode, the dilution rate is 0.033 h^{-1} and feed glucose concentration is 7 mM in both.

The batch culture is initiated with a glucose concentration of 15 mM. It consumes glucose and produces lactate at very high rates and reached 11.8 mM and 4.9 mM of glucose and lactate respectively at 50 h (Figure 4A&B). The ratio of glucose to lactate conversion (J_L/J_G) is 1.55 mol/mol, indicating that the culture operated at high metabolic flux state. At this time, with a cell concentration of 1.8×10^6 cells/mL, the culture is switched to a continuous mode. The culture continues at a high flux state (J_L/J_G) is 1.53 mol/mol) to reach a steady state with a relatively low cell concentration of 3.2×10^6 cells/mL.

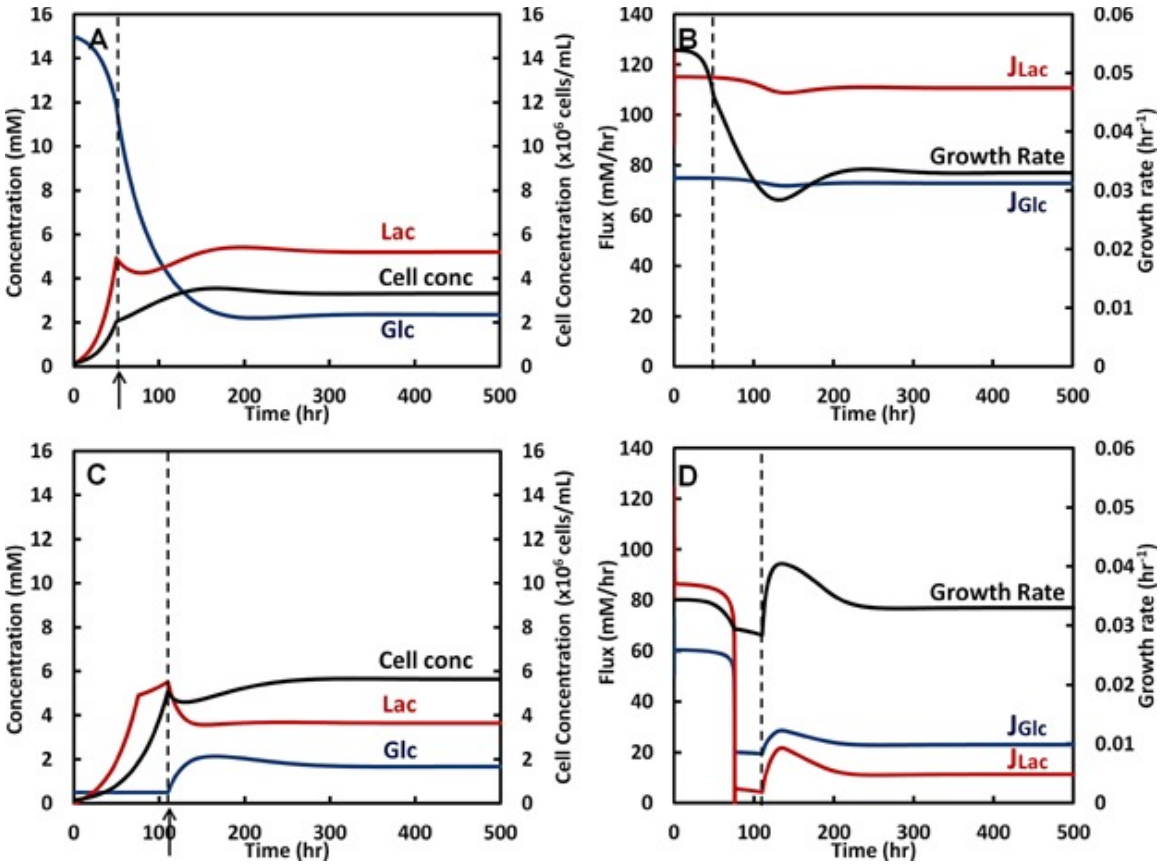

Figure 4. Transient simulations of continuous culture that reaches steady states with distinct cell concentrations.
(A-B) Culture started from batch mode exhibits high metabolic flux and remains at high flux state upon initiation of continuous culture. Such culture reaches steady state with high metabolic flux and lower cell concentration. (C-D) Culture started from fed-batch with glucose maintained at low level exhibits a metabolic shift to low flux state. Upon initiation of continuous mode, the culture remains at low flux state and reaches steady state with higher cell concentration. Arrow (↑) indicates the time at which continuous mode is initiated. In the continuous mode, dilution rate and feed glucose concentration were fixed at 0.033 h^{-1} and 7 mM, respectively.

For the fed-batch culture, glucose concentration is maintained at 0.5 mM. Over time, the culture undergoes a metabolic shift to a low flux state. After 110 h (Figure 4C&D) JL/JG was 0.22 mol/mol indicating low metabolic state. Cell concentration reaches 5.1×10^6 cells/mL. At this point, the culture is switched to continuous mode, where it continues at a low flux state as indicated by the low J_L/J_G. Glucose and lactate concentrations settled down

to 1.7 mM and 3.6 mM, respectively, and the cells continued to grow before reaching a final steady state concentration of 5.6×10^6 cells/mL.

2.5 DISCUSSION

In this study, we constructed a multi-scale model combining intracellular metabolic pathways with the macroscopic cell concentration in a continuous bioreactor. From a modeling perspective, biological systems are intrinsically multi-scale, involving time and length scales spanning over many orders of magnitude, from microsecond and nanometer at submolecular level, millisecond to submicrometer in biochemical reactions, to centimeter and minutes in tissue and even organism levels. In this multi-scale model, the time constants involved range from the order of seconds in enzyme reactions to multiple of hours in the reactor, and the material quantities range from the order of 10^{-5} moles per L for metabolites to 10^{10} per L for cells. Due to the ill-conditioned nature of the model, i.e. the span of over many orders of magnitude between distinct variables, appropriate scaling was necessary to solve the system.

The steady state multiplicity predicted by the mechanistic metabolism model is manifested in the continuous bioreactor. In the bistable region, for a given dilution rate, the culture can exist at either a high glycolysis flux steady state or a low glycolysis flux steady state. The two kinds of steady states have different metabolic efficiency. At a high flux state, the vast majority of glucose is converted to lactate, whereas at a low flux state more glucose consumed is converted to biomass. Thus different steady states are marked by distinct steady state cell concentrations. With the feed glucose concentration used in the simulation, multiple steady states are observed only in a range of dilution rates. Outside of the bistable region, in the high dilution rate region, only the high flux states are present. Whereas in the

low dilution rate region, only the low flux states exist. It is notable that the model predicts that in the range of lactate production rate to glucose consumption rate ratio (J_L/J_G) between 0.8–1.45 no stable steady state exists. The experimental data in the literature are in close agreement to this finding [4, 5].

In the bistable region, which steady state (high flux state or low flux state) a culture will reside in is dependent on the history of the culture. One can thus influence the steady state to be reached by controlling the cell's metabolic state before steady state is reached. Since the "default" state of cells in culture under typical culture conditions is a high flux state, at issue is thus "guiding" the cell to a low flux state before steady state is reached.

This was illustrated by two approaches: one by eliciting a metabolic shift to a low flux state in fed-batch culture via controlling glucose at low levels (Figure 4), and the other by operating at a low dilution rate region in which only the low flux steady state exists before gradually increasing the dilution rate to the bistable region (Appendix Figure 2). Indeed these two approaches were used to reach a low flux steady state in two experimental studies [17, 20].

The bistable behavior observed in continuous culture is reminiscent of that observed in fed-batch cultures. Cells in the later stage of fed-batch cultures can switch their metabolism from high rate of lactate production to lactate consumption. The metabolic shift to lactate consumption in fed-batch cultures has been shown to be correlated with a higher productivity [1, 2]. In continuous culture, a steady state with lactate consumption does not exist without lactate supplementation in the feed. Addition of lactate to the feed medium of a continuous culture may not be used in practice, but the result does show its feasibility as a steady state operation.

In culture, mammalian cells also consume glutamine and other amino acids. These amino acids are building blocks for cellular proteins, nucleotides, etc. Glutamine also contributes to the energy metabolism through anaplerotic pathway [31]. The rate of glutamine consumption at the high flux state is higher compared to that at low flux state. Overall glutamine consumption rate is almost one order of magnitude lower than glucose. For the purpose of demonstrating the mechanism of multiple steady states in continuous culture, glutamine effect is considered small and was not included in the model.

In our model, the specific growth rate is expressed as a Monod type kinetics with respect to the concentrations of glucose and lactate (Equation). Thus, we implicitly assume that all other nutrients, including glutamine and other amino acids, are in ample supply. While a few amino acids, including glutamine, are essential for the growth of cells in culture, none of them are depleted in the spent media; indicating no amino acid limitation in the cultures. Thus, the use of Equation 4 as a first approximation is appropriate in this case. In cases where some amino acids may be depleting, a modified form which includes those amino acids will be required.

There has been a resurgence of interest in using continuous culture for recombinant therapeutic protein production [14]. The prospect of producing biosimilars in different regions of the world has provided incentives for constructing regional manufacturing facilities. Many new facilities will aim to be smaller and more flexible in terms of the product it produces while sustaining a high throughput similar to the facility designed for fed-batch manufacturing. Continuous processes are well suited to such purposes.

Furthermore, continuous processes offer the possibility of steady state operation in which the metabolic state of cells is kept relatively constant as opposed to the constantly changing

nature in fed-batch cultures. Increasingly, biopharmaceutical production is focusing on controlling product quality in addition to the productivity. The glycosylation pattern of the product protein is a key product attribute that process engineers strive to control and is reported to be affected by many environmental factors that fluctuate in typical fed-batch cultures [32-35]. Steady state operation of continuous cultures may minimize such culture variations and provides greater control of product quality.

The multi-scale model presented demonstrates that multiple steady states exist under some culture conditions. Since those different steady states represent different metabolic states, they may also elicit different glycosylation patterns or other product quality attributes with some being the preferred. In view of such possibilities, controlling the culture condition to ensure it follows the trajectory to reach the desired steady state is thus critical. The model we established should provide mechanistic understanding to prescribe such trajectories to enhance process performance.

3 MECHANISTIC STUDY OF THE METABOLIC SHIFT TO LACTATE PRODUCTION IN MAMMALIAN CELL CULTURE

3.1 SUMMARY

Cultured mammalian cells invariably exhibit high glycolysis flux and high lactate production during their growth. As the growth rate tapers, cells may switch to a state of low glycolysis flux with low lactate production or even lactate consumption. The switch to lactate consumption has been shown in correlation with productivity. Cultures that underwent a switch to lactate consumption had higher tiers than those did not. In fed-batch cultures, cells sometimes switch back to a high glycolysis flux state and resume lactate

production. Such metabolic switch occurs at the late stage of cultures when the cultivation conditions represent a high-stress environment. The metabolic homeostasis of cells is tightly regulated through the AMPK signaling pathway, which is stimulated in response to energy, nutrient, and high-osmotic stresses. We have previously shown that the glycolysis flux of proliferating cells exhibits a hallmark of bistability in distinct high and low flux states. In this study, we use mathematical modeling to demonstrate the effect of AMPK on the bistability of glycolysis flux, and thus the topology of steady states. The transition from the low to the high flux state occurs in a certain region of the steady state topology. The metabolic outcome of the cells depends on the trajectory that they undertake in the steady state topology. Cells encountering the region that allows a switch in the metabolic state will adopt high glycolysis flux with elevated lactate production. Insights into this switch behavior provide a guideline principle in control of cell metabolism in fed-batch cultures.

3.2 INTRODUCTION

The extensive regulation of the glycolysis pathway in mammalian cells gives rise to very complex metabolic behavior. The metabolic behavior is affected by the isoform composition of several key enzymes in the glycolysis pathway. Glucose metabolism is further affected by cell's growth rate mediated through various signaling pathways. The complex regulation of glucose metabolism has a profound effect on the productivity of therapeutic proteins produced in cell culture. Cells invariably produce lactate from glucose when growing rapidly. However, under some conditions, for example in the stationary phase of fed-batch culture, they may consume lactate. It is not unusual that the same cell line may have different metabolic behavior, even under seemly identical culture conditions.

When analyzing data from a biomanufacturing plant, we found that the top productivity runs switched from lactate production to lactate consumption, while low productivity runs remained in the lactate production mode throughout the culture [1]. Such observations attest to the significant influence of glucose metabolism on productivity. Using a mechanistic kinetic model, we have previously attributed the "unpredictability" in glucose metabolism to the multiple steady state behavior of glycolysis flux in mammalian cells [21]. The topology of the glycolysis flux at different glucose and lactate concentration changes as the growth rate varies, due to changing levels of AKT activation of PFKFB enzyme [3]. In a fed-batch culture, the difference in the timing of glucose addition may cause cultures at the same initial conditions to diverge to different metabolic fates [3].

The multiple steady states behavior has also been observed in the continuous bioreactor. In the previous section (Section 2), a multiscale model that links the intracellular metabolism with the bioreactor cultivation conditions is described [36]. The model was used to demonstrate the occurrence of steady state multiplicity in a range of dilution rates in continuous culture. The low flux steady state is the desired state for increasing productivity because it provides a higher cell concentration as compared to the high flux state. In order to attain the metabolic shift to a low flux state in continuous culture, a low dilution rate is necessary. Intriguingly, model prediction shows that at a low flux state, lactate consumption occurs only under the presence of lactate in the feed.

In addition to AKT, another major player of signaling pathways that affect cell metabolism is AMPK. AMPK is activated by energy [37], nutrient [38-42], and hyperosmotic stresses [43]. During late stage of culture, many metabolites may accumulate to a high level, representing a high osmolality environment [1]. Under such conditions, AMPK might be

activated, leading to a stimulation of glycolysis flux through PFKFB activation. This chapter discusses the effect of AMPK activation on the topology of glycolysis flux at various levels of lactate and glucose. Glucose addition during high AMPK activity may shift the culture from a low flux state to a high flux state with a concurrent increase in lactate production. Through model simulations, we show that with the presence of lactate in the feed, one can prevent the occurrence of the metabolic switch-up and retain the culture at a low glycolysis flux state.

3.3 MATERIALS AND METHODS

A kinetic metabolic model of the central metabolism pathway in mammalian cells was previously constructed [3]. It includes glycolysis and pentose phosphate pathways, TCA cycle, malate-aspartate shuttle, and other inter-compartmental shuttles. The mass balance equations of 40 reaction intermediates involved in these pathways were incorporated into an ordinary differential equation (ODE) model. The rate expressions for all enzymatic reactions were derived based on the mechanistic understanding of enzyme kinetics [44]. The kinetic parameters were obtained from the previous literature.

Many reactions in the glycolysis pathway are catalyzed by multiple isozymes, which are subjected to diverse regulatory mechanisms [21]. The model used in this study considers the dominant isoforms expressed across different CHO cell lines as shown in our transcriptome data. Specifically, the HK1 isoform of hexokinase, the liver isoform of phosphofructokinase-1 (PFKL), the M2 isoform pyruvate kinase (PKM2), and the inducible isoform of 6-phosphofructo-2-kinase/fructose-2,6-bisphosphatase (PFKFB3) were considered. Both PFKM and PKM2 are highly sensitive to activation by fructose-1,6-biphosphate (F16BP). The PFKFB3 isoform displays the highest kinase/phosphatase (K/P)

ratio among other PFKFB isoforms. Figure 5 shows the allosteric regulations that these isoforms are subjected to [3].

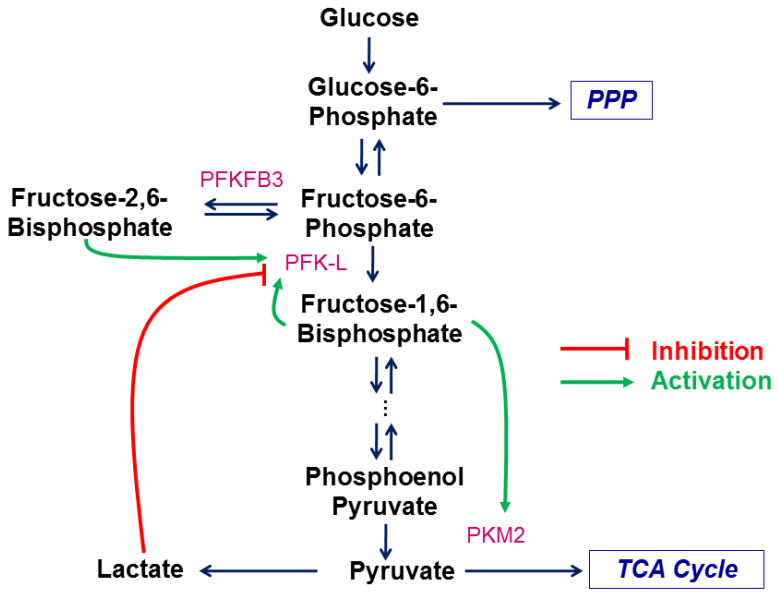

Figure 5. Allosteric regulations of glycolysis isoenzymes that are predominantly expressed in CHO cells.

The regulation of glycolysis flux by AMPK is modeled as an increase in the kinase activity (or K/P ratio) of the bifunctional enzyme PFKFB.

3.3.1 Steady state simulation

An algebraic model that consists of steady-state mass balance equations for all the reaction intermediates was derived from the ODE model [3]. The model was used to explore possible steady states. The inputs into the model are the K/P ratio and the concentrations of glucose and lactate. The extracellular concentrations of glutamine, the intracellular concentrations of energy nucleotides and a number of other metabolites were set to be constant [3]. The steady state solutions were obtained using the numerical solver *fsolve* in Matlab (Mathworks, Inc.). For each combination of K/P ratio, glucose and lactate

concentrations, positive and real-valued solutions were calculated using initial guesses, which are drawn from the standard uniform distribution using the pseudo-random number generator (*rand*) in Matlab.

3.3.2 Transient simulation

Transient simulations were performed using the ODE solver *ode15s* in Matlab. The initial extracellular lactate concentration is 25 mM. Cell concentration was assumed to be constant at $2x10^7$ cells/mL throughout the course of the simulation. The K/P ratio was held constant at 45 when simulating the effects of glucose on the metabolic switch, which restrains the simulation to the moment when the switch occurs. In another case, when the effects of K/P ratio on the switch are investigated, extracellular glucose was held constant at 5 mM.

3.4 RESULTS

3.4.1 Bistability in Glycolysis Flux and the Diversity of Lactate Behavior

The glycolysis flux behavior was simulated when lactate concentration and K/P ratio was held constant at 20 mM and 40, respectively (Figure 6A). In the glucose concentration range of around 3-21 mM, glycolysis flux exhibits the bistable behavior with three types of steady states: the two representing high (red) and low flux states (blue) are stable; the other is unstable (orange), which cannot be realized experimentally. Outside this range, glycolysis flux has only one steady state for one glucose concentration; below 3 mM, only the low flux state is observed, whereas above 21 mM, only high flux state exists. Glycolysis flux states play an important role in dictating the behavior of lactate. In the high flux states, lactate is rapidly produced at a high rate. In the low flux region, it is produced a slow rate

in the bistable region and consumed when the glucose concentration further decreases (i.e. the lactate consumption region is colored in green).

A transition from lactate consumption to lactate production and then a surge in the production rate is usually accompanied by increasing levels of glucose, and even a switch of flux state. Starting from a low glucose concentration (< 3 mM, thus the low flux state with lactate consumption), as the glucose concentration increases, the flux moves along the stable steady states line, and then enters the lactate production region. Further increase of glucose levels (> 21 mM) causes a switch from a low flux state to a high flux state, characterized by an abrupt increase in lactate production rate. The glucose concentration at which the switch happens hereinafter will be referred to as the "switch-up" concentration of glucose.

The concentration of lactate also affects its behavior. As an allosteric inhibitor of phosphofructokinase (PFK) (Figure 5), lactate exerts an inhibitory effect on glycolysis flux [45, 46]. In our previous work, we have demonstrated that an increase in the levels of lactate shifts the "switch-up" concentration to higher glucose levels [3]. At very high levels of lactate (> 40 mM), the "switch-up" concentration of glucose far exceeds those seen in culture, which becomes near lethal to cells due to high osmolality. In this study, we further examined the effects of lactate concentration on the lactate consumption region (Figure 6B). At low levels of lactate concentration, lactate is consumed only at a notably low level of glucose and outside the physiological range. With increasing levels of lactate, the lactate consumption region extends to a higher concentration of glucose. At 45 mM of lactate, lactate is consumed throughout the entire low flux region (in the glucose concentration range of ~0.5 – 40 mM).

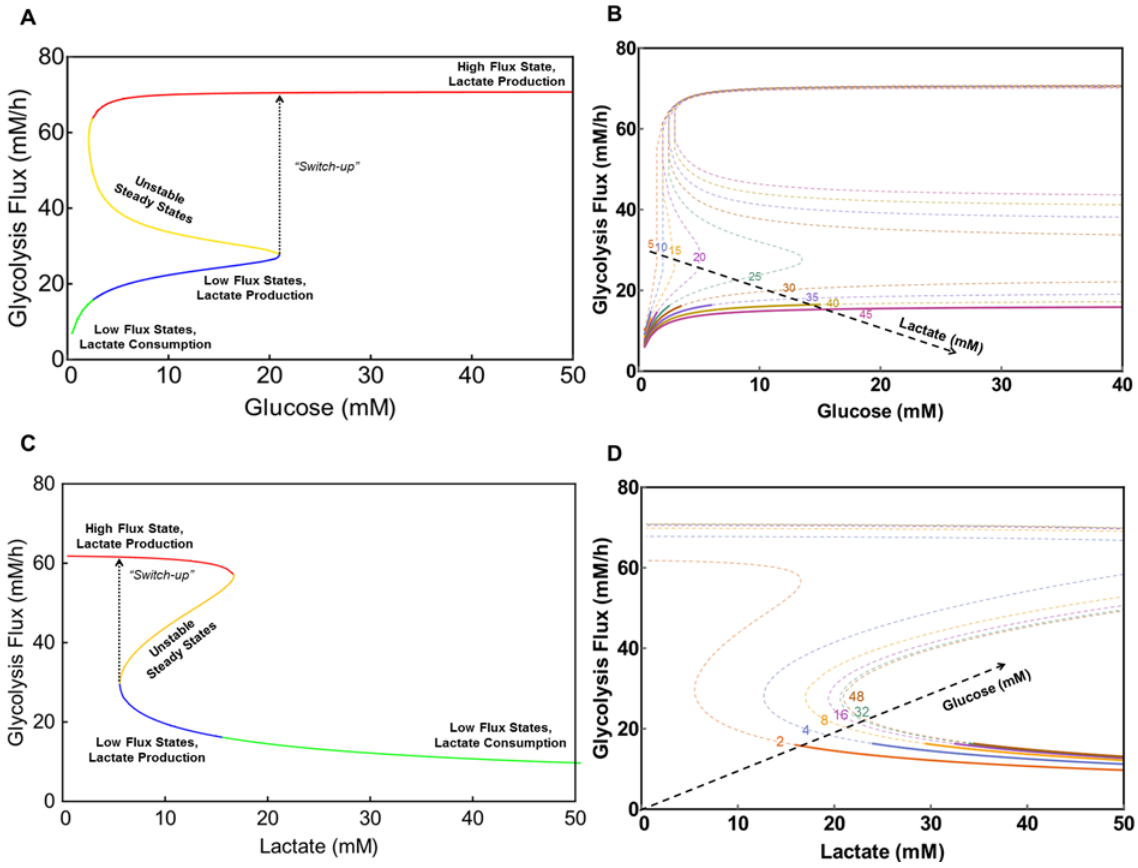

Figure 6. Bistability in glycolysis activity and diversity of lactate behavior.
(A) Glycolysis flux plotted against extracellular glucose concentration. High flux states are colored in red. Low flux states with lactate production and consumption are colored in blue and green, respectively. Unstable steady states are colored in orange. (B) Effects of lactate concentration on the "switch-up" concentration of glucose and the shape of the lactate consumption region (solid lines). (C) Glycolysis flux plotted against extracellular lactate concentration. High flux states are colored in red. Low flux states with lactate production and consumption are colored in blue and green, respectively. (D) Effects of glucose concentration on the "switch-up" concentration of lactate and the shape of the lactate consumption region (solid lines).

3.4.2 Effects of Glucose Concentration on Lactate Behavior

In the previous section, we examined the switch-up concentration of lactate at a given glucose level (Figure 6C). The simulation was performed when glucose concentration was held constant at 2 mM, at which condition, the lactate is consumed (as shown in the previous section). In the lactate concentration range of ~6-16 mM, glycolysis flux confers

the hallmark of bistability. In this bistable region, depending on the previous state of glycolysis flux, the system can be at a high or a low flux state [3]. When the lactate concentration changes, the system traverses along the stable steady states lines. Starting at a high concentration of lactate (thus the low flux state with lactate consumption), as the lactate level decreases, the flux gradually moves away from the lactate consumption region and enters the bistable region, where lactate starts to produce at a slow rate. In the bistable region, glycolysis flux remains at the low state. Further decrease in the lactate level to 6 mM ("switch-up" lactate concentration) causes an abrupt shift to a high flux state accompanied by high lactate production rate.

The behavior shown in Figure 6C was obtained at a constant concentration of extracellular glucose. Such behavior may vary at different glucose concentration. We thus investigated the effects of a wide range of glucose levels on the switch-up concentration of lactate (Figure 6D). At low levels of glucose, the switch-up concentration of lactate is also low. Increasing glucose levels shifts the "switch-up" to higher lactate concentrations. At high levels of glucose, the effects of glucose concentration on the switch-up become saturated; at 32 and 48 mM glucose, the switch-up concentrations of lactate are largely similar.

The extracellular concentration of glucose also affects the lactate consumption region. At a low glucose concentration, lactate is consumed at a wide range of lactate concentration (~ 16 to 50 mM and higher). As the glucose levels increase, the lactate consumption region, marked by the solid lines in Figure 6D, shifts to higher concentrations of lactate. At a very high glucose concentration of 48 mM, lactate is consumed only when its concentration exceeds 34.5 mM.

The synergistic effects of glucose and lactate concentrations on the "switch-up" are presented in a three-dimensional plot with the flux plotted against glucose and lactate concentrations (Figure 7). The plot shows the top (red) and bottom (blue or green) surfaces representing high and low flux states with lactate production or consumption, respectively. A slice of the plot at a fixed lactate concentration of 20 mM along the glucose axis yields the curve shown in Figure 6A. Similarly, the curve shown in Figure 6B is a slice of the plot at a fix glucose concentration of 2 mM along the lactate axis.

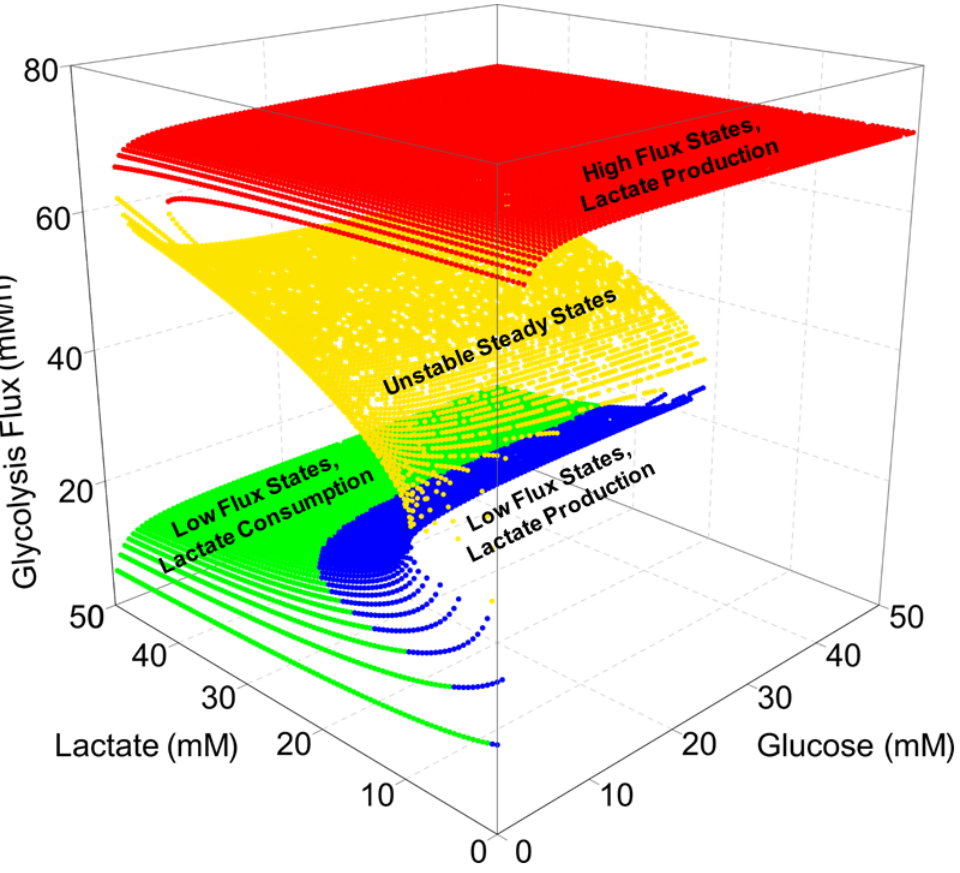

Figure 7. Synergistic effect of lactate and glucose concentrations on metabolic "switch-up" and the lactate consumption region.
The effect of lactate and glucose on the "switch-up" and on the shape of the lactate consumption region is examined by model simulation for a wide range of lactate and glucose concentrations (0-50 mM for both).

3.4.3 Effect of AMPK on Lactate Behavior

We have previously demonstrated the regulatory effects of growth on glycolysis, which influences the metabolic switch from high to low flux state during the late stage of the culture. In the current study, we investigated the effects of cellular stresses on glycolysis flux through AMPK. The AMPK signaling pathway regulates cellular energy homeostasis and promotes glycolysis activity [47]. Under cellular stresses, AMPK is activated and its active form (pAMPK) stimulates glycolysis through the activation of the kinase activity of PFKFB2, 3 [41, 48, 49] and induction of GLUT1, 4 and HK [50, 51] (Figure 8). The concurrent increase in the pAMPK level (and thus K/P ratio) causes a stimulation of glycolysis. Among three targets regulated by pAMPK, PFKFB is stimulated at the activity level, whereas the other two are regulated either at the transcriptional or translocational level. In order to examine the stability and steady state behavior, we only consider the system in which enzymes are uniformly distributed inside the cells with constant levels. Therefore, the effect of AMPK on glycolysis flux is thus described as its regulation on PFKFB.

Figure 9A demonstrates the effects of K/P on the glycolysis flux behavior at a constant lactate concentration of 20 mM. At low K/P ratios (10-30), a shift from the low flux state to the high flux state cannot occur for the entire range of glucose concentration examined. Higher K/P ratios bring the “switch-up” concentration of glucose to lower levels. At very high K/P ratios, the “switch-up” become very likely because glycolysis flux only has high flux states throughout most of the glucose concentration. An opposite trend for the “switch-up” concentration of lactate was observed when glucose concentration is held constant at 2 mM (Figure 9B). At low K/P ratios, the switch-up occurs only when lactate is not present.

Interestingly, at a very low level of K/P ratio, the switch-up is not possible even at zero lactate. With increasing K/P ratios, the "switch-up" moves to higher lactate concentrations.

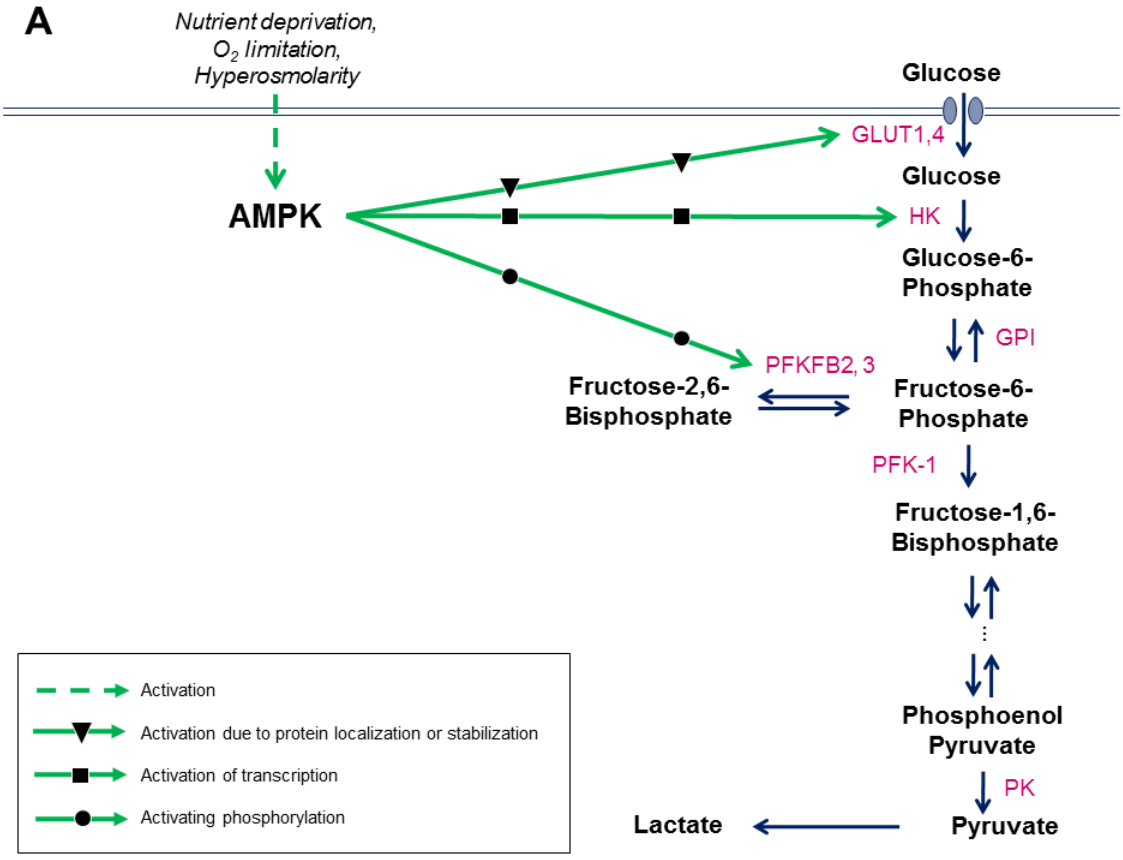

Figure 8. Regulation of AMPK on glycolysis.
The AMPK signaling pathway is involved in regulation of cellular energy homeostasis. In response to energy, nutrient, and hyperosmotic stresses, AMPK is activated, leading to the induction of GLUT1,4 and HK. In addition, AMPK can phosphorylate PFKFB2, 3 to promote the production of fructose-2,6-biphosphate levels, which in turns further activates PFK activity and thus increases glycolysis flux.

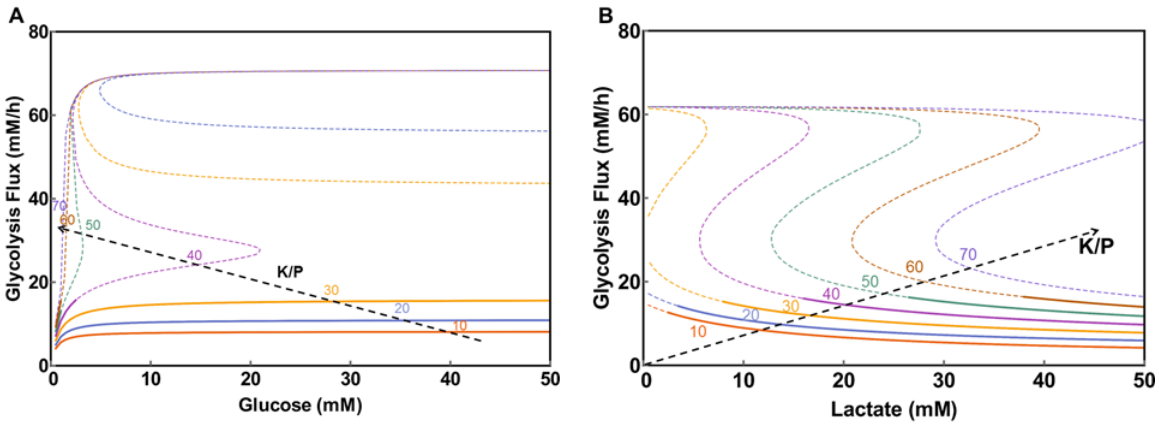

Figure 9. Effect of pAMPK level, represented as K/P ratio, on the metabolic "switch-up" and the shape of lactate consumption region (solid lines).
The glycolysis flux is plotted against glucose (A) and lactate (B) concentrations.

Figure 10 shows the three-dimensional curves of glycolysis flux plotted against glucose and lactate at four discrete values of K/P ratio. At a low K/P ratio, the top (high flux) plane is present only at very low levels of lactate. At higher lactate concentration, glycolysis flux can operate only at a low flux state with lactate consumption, shown in the green region that dominates the bottom (low flux) plane. The metabolic "switch-up" moves to a region where lactate is almost not present (shown in the slim blue region) and glucose are at extremely high levels, outside the examined range. Such condition is not relevant in culture, and thus not considered in this study. As the K/P ratio increases, the bottom plane recedes towards lower glucose and higher lactate concentrations such that a metabolic shift from the low flux plane to the high flux plane becomes possible. As the bottom plane regresses, the lactate consumption occurs only at high lactate concentration or very low levels of glucose, outside the physiological range. At a very high K/P ratio ($\geq$ 70), glycolysis flux is mostly in its high flux states throughout the examined range of glucose and lactate concentrations. The low flux states are only at very low levels of glucose (near

depletion). The “switch-up”, therefore, becomes feasible for almost all the glucose and lactate levels that have been seen in cell culture.

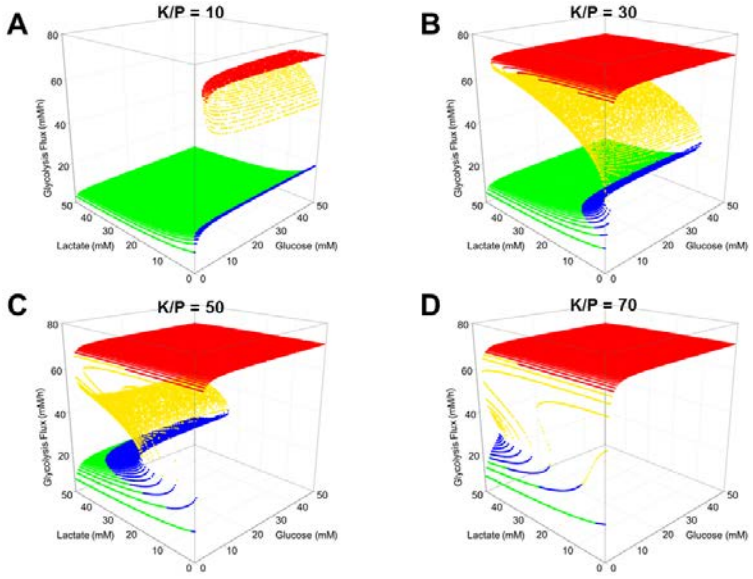

Figure 10. Effect of glucose and lactate on the metabolic “switch-up” and lactate consumption region at different K/P ratio.
The top (red) and bottom (blue or green) surfaces are stable steady states representing high and low glycolysis flux states. The bottom surface is divided into two regions: lactate production (blue) and lactate consumption (green). Orange surfaces are unstable steady states, which cannot be realized experimentally. (A) K/P = 10, (B) K/P = 30, (C) K/P = 50, (D) K/P = 70.

3.4.4 Trajectory of the Metabolic “Switch-up” Resulted from Glucose Addition

During the growth phase of cells in culture, lactate is produced at a high specific rate. As the growth rate diminishes, lactate production rate decreases with a concurrent switch from a high to a low glycolysis flux state. As time progresses, some cultures may start to consume lactate whereas others resume to the high lactate production rate, which is also marked by a high rate of glucose consumption [1]. The variation in lactate behavior during late stages of culture suggests two possible metabolic fates of cultures while cells progress on the low flux plane.

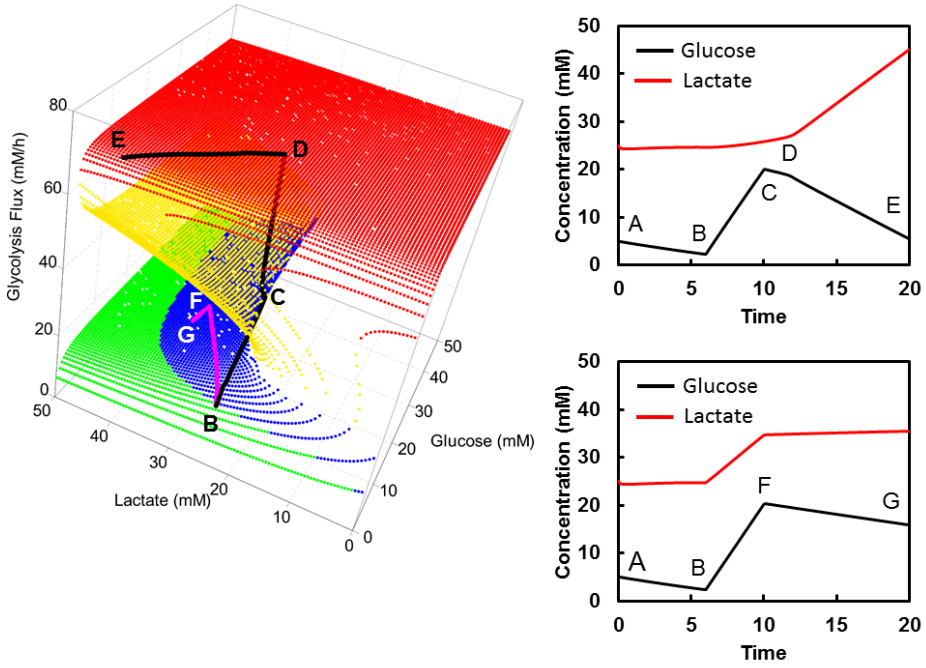

Figure 11. Transient simulations of cultures with and without a metabolic switch-up. At t = 0, cells are positioned on the bottom (low flux) plane in a low-stress condition (low pAMPK, and thus low K/P ratio), with low glucose and medium-high lactate concentrations (graph on the right-hand side of the figure). As the culture progresses with the appearance of cellular stresses, pAMPK activity increases (denoted by an increase of K/P ratio from 10 to 45), glucose is consumed and lactate is produced at low specific rates. The culture trajectory follows the line (A-B). Glucose is added slowly to the culture, leading to an increase in its concentration, as shown by the (B-C) line. After a certain time, it encounters a receded section of the bottom (low flux) plane, which leads to a shift from the low to the high flux state (C-D line) where cells start to consume glucose and lactate at high specific rates. No metabolic shift is observed when lactate is added to the culture (B-F line) along with glucose addition. The simulation shows that with lactate feed, a metabolic switch-up can be avoided.

A set of transient simulations was performed to demonstrate that different feeding strategies might diverge the metabolic fates of cultures (Figure 11). Cells are initially on the low flux plane of low K/P ratio of 10. As the culture progresses, cells consume glucose and produce lactate, as denoted by a path with decreasing glucose concentration and increasing lactate concentration. The path is depicted by the line AB in the two-dimensional plots of Figure 11. Line AB also represents a simultaneous increase in the K/P ratio from 10 to 45. The surface plot shown in Figure 11 corresponds to K/P ratio of 45

(pAMPK activation, as demonstrated in Figure 10). In the first scenario, glucose concentration is gradually increased due to glucose feeding to the culture starting at 6 h (line BC, Figure 11). During the feed, the path encounters the receded section of the low flux plane, leading to a switch up from the low flux plane to the high flux plane (line CD, Figure 11). In the other scenario, both glucose and lactate are added to the culture (line BF, Figure 11), leading to an increase in their concentrations. This feeding strategy diverges the path away from the receded plane by shifting the culture towards a higher lactate concentration. A metabolic switch-up thus cannot occur and the cells remain in the low flux plane. In the first scenario, upon switching to a high flux state, cells start to produce lactate and consume glucose at a high specific rate. Such culture only switches back to a low flux state at a notably low glucose concentration, which is not usually seen in culture [3]. In the second scenario, further addition of glucose to the culture (data not shown) will not cause the culture to switch to a high flux state unless the K/P ratio increases further. The difference in the feeding strategy, wherein lactate is either present or not in the feed, leads to variation in lactate behavior of cultures with very similar metabolic behavior.

3.4.5 Trajectory of the Metabolic "Switch-up" Caused by AMPK Activation

We performed another set of transient simulation to further demonstrate that lactate feeding helps prevent the metabolic "switch-up". In this study, cells are initially in the low flux plane of low K/P ratio and consume lactate. As the culture progresses, cells move along a path with decreasing lactate concentration (line AB, Figure 12). When cells are subject to certain energy or nutrient stresses, AMPK is activated, leading to an increase of K/P ratio (line BC, Figure 12). In the first case, while moving along AB line, as a result of the surge of K/P ratio (or pAMPK), cells encounter a receded section of the low flux plane and

undergo a metabolic switch from the low to the high flux plane (line CD, Figure 12). In this case, cells start to produce lactate at a high specific rate towards the end of the culture (line DE, Figure 12). In another case, lactate is added to the culture, which diverges the culture trajectory away from the receded region (line BF, Figure 12). Because the metabolic "switch-up" does not occur, cells remain at the low flux plane where lactate is produced at a low rate (line FG, Figure 12).

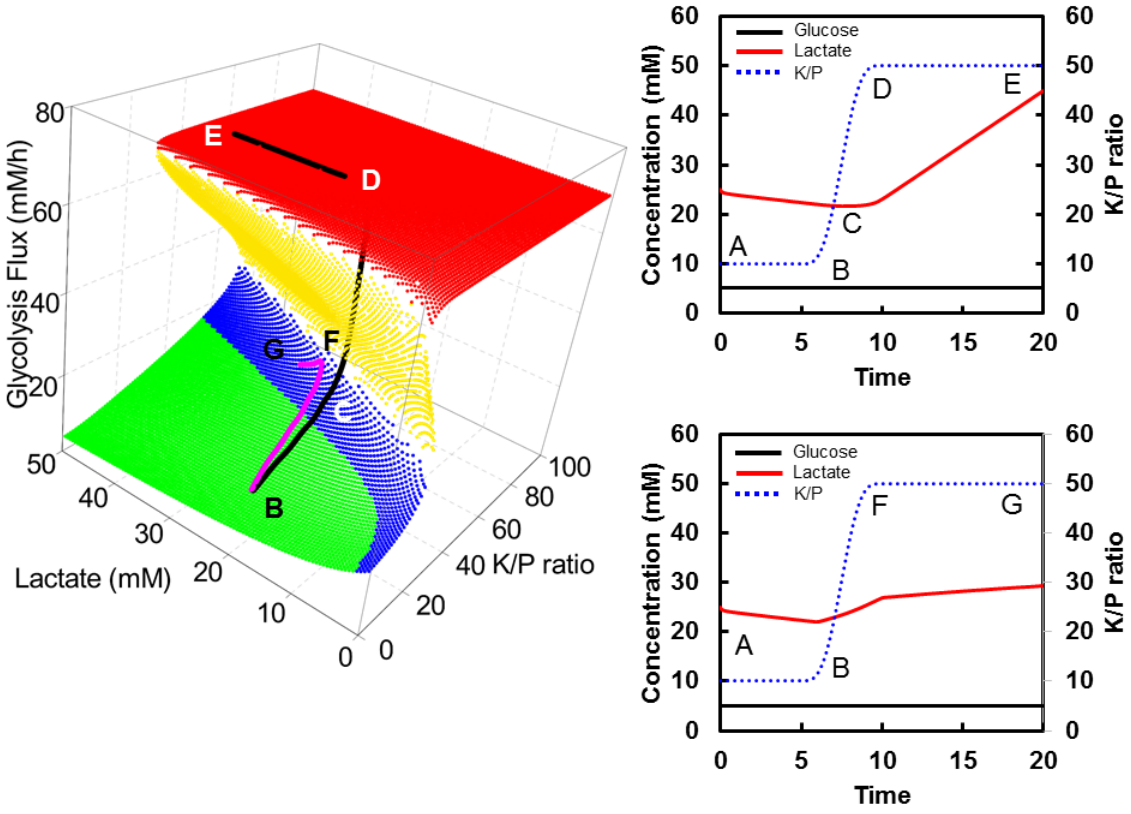

Figure 12. Transient simulations of cultures with and without a metabolic switch-up. At t = 0, cells are positioned on the bottom (low flux) plane in a low-stress condition (low pAMPK, and thus low K/P ratio), with low glucose and medium-high lactate concentrations (graph on the right-hand side of the figure). As the culture progresses, glucose is consumed and lactate is produced at low specific rates. The culture trajectory follows the line (A-B) with an increase in lactate concentration (glucose is assumed to be constant throughout the culture). With the appearance of cellular stresses, pAMPK activity increases (denoted by an increase of K/P ratio from 10 to 50, line B-C-D and B-F). After a certain time, it encounters a receded section of the bottom (low flux) plane, which leads to a shift from the low to the high flux state (C-D line) where cells start to consume glucose and lactate at high specific

rates. No metabolic shift is observed when lactate is added to the culture (B-F line). The simulation shows that with lactate feed, a metabolic switch-up can be avoided.

3.5 DISCUSSION

We have previously demonstrated that the multiplicity of steady states in glycolysis flux arises from the expression of glycolytic isozymes commonly seen in many rapidly growing cells, including cultured mammalian cells [21]. We also showed that the metabolic switch from a high glycolysis flux state to a low flux state in fed-batch culture is a reflection of the bistable behavior of glycolysis flux [3]. In this study, using the concept of bistability, we investigated the mechanism of the metabolic switch from a low flux to a high flux state ("switch-up"), with a concomitant increase in lactate production. The metabolic switch-up was attributed to the increase in the kinase activity of PFKFB enzyme because of AMPK activation. The switch-up was examined for different combinations of AMPK activity (or K/P ratio), glucose, and lactate concentrations.

The metabolic "switch-up" has been observed in cultured mammalian cells during the late stage of culture [1]. The culture conditions at its late stage usually represent a high-stress environment with the accumulation of several by-product metabolites, elevation of osmolarity and sometimes, limitation of certain types of nutrients. AMPK has been known for its important role in regulating cellular homeostasis in response to energy, nutrient, and hyperosmotic stress. Under a high-stress environment, AMPK is activated, leading to the simulation of glycolysis activity [41, 48, 50]. Using the mechanistic metabolism model, we demonstrated that as the levels of activated AMPK varies, the topology of the glycolysis flux at different glucose and lactate concentration changes due to changing PKKFB kinase activity. At a high level of activated AMPK (thus high kinase activity of PFKFB), the low flux plane recedes towards lower glucose and higher lactate concentrations. As a result, the

system can only have a high glycolysis flux steady state for a wide range of glucose and lactate concentration. When the system is operated near this receded region, even a small perturbation can diverge it to drastically different metabolic fates.

The model simulation also demonstrated the possibility of lactate addition to prevent the metabolic switch-up. As we described above, the levels of active AMPK govern the topology of glycolysis flux, and thus the switch-up behavior. The active form of AMPK enhances the kinase activity (K/P ratio) of PFKFB, resulting in an increase of F26BP production and thus the stimulation of PFK activity. Lactate counteracts the AMPK-mediated activation of PFK through its inhibitory effect on this enzyme. Increase in lactate concentration leads to an increase in the switch-up concentration of glucose. Interestingly, the result does show that lactate addition to the culture may help avoid the switch-up, although this might not be used in practice.

The mechanistic metabolic model presented here provides insights into the possible cause of metabolic switch to a high flux state with a surge in lactate production. This somewhat unpredictable behavior of metabolism has been observed in cell culture bioprocessing. The simulation result supports that the multiple steady state behavior of glycolysis flux may be at play. With a bettering understanding of the root cause of such metabolic switch, one can devise strategies to control the metabolism in a robust manner and avert the unfavorable switch.

4 MECHANISM FOR SHIFT OF GLUCOSE METABOLISM DURING STEM CELLS DIFFERENTIATION TOWARDS HEPATOCYTE-LIKE CELLS

Reproduced from: Chau D, Le T, Park Y, O'Brien C, and Hu W-S. *Energy Metabolism of Human Embryonic Stem Cells during Hepatocyte Differentiation*. (In preparation).

DC and TL analyzed microarray data. TL and CO constructed the ODE model. TL performed model simulation and analyzed the simulation results.

4.1 SUMMARY

The metabolic phenotype of human embryonic stem cells changes as they differentiate towards hepatocyte-like cells (HLC). At the very early stage, stem cells rely on glycolysis for energy generation, marked by the high specific rates of glucose consumption and lactate production. During HLC differentiation, glucose consumption rate decreases progressively with a concurrent decrease in lactate production, which suggests a switch of metabolic flux states. In this study, the mechanistic kinetic model of energy metabolism in mammalian cells [3] was extended to include the rate equations for isoforms of key glycolysis enzymes. The model was used to demonstrate the existence of multiple steady states of glycolysis flux at certain stages of differentiation. Model prediction showed that during the course of differentiation, a switch from a high to a low glycolytic flux state occurred due to changes in the isoform compositions of key glycolysis enzymes. The simulation results are in agreement with the metabolic profile of HLC during differentiation.

4.2 INTRODUCTION

Human embryonic stem cells are the pluripotent stem cells derived from the inner cell mass that possesses the ability to self-renew and differentiate into highly specialized cell types

found in the body. Using different growth factors and cytokines to mimic embryonic signaling cues, stem cells can be guided through different developmental stages to become hepatocytes in a manner similar to embryonic development [52-55].

A number of studies have shown the resemblance of stem cell-derived hepatocytes (SDHC) to primary hepatocytes at the global gene expression and proteome levels [56-58]. Despite these similarities, SDHCs still lack key markers and functionalities shown in fully matured hepatocytes. Certain metabolic functions of the liver such as cytochrome P450 (CYP) activity were either nonexistent or present at very low levels [52, 56]. Baxter et al. demonstrated that SCDHs are more representative of fetal hepatocytes than adult hepatocytes at the transcript, protein, and functional level [56]. Li et al. examined the time-course transcript dynamics of embryonic development from embryo to post-natal liver, and found that the transcript levels of genes involved in metabolic processes and cell cycle were significantly altered [59]. Although the role of metabolism for cellular growth and maintenance during development has been well studied, its impact on the differentiation of SCDHs remains elusive.

Stem cells have been shown to rely mainly on glycolysis for energy generation [60-62]. In more differentiated cell types, the energy demand is typically met with the upregulated oxidative phosphorylation (OxPhos) activity [63]. Primary hepatocytes have been shown to exist in a low glycolytic flux state [64, 65], and utilize mitochondrial respiration for bioenergetic demands [66-69]. The preference between glycolysis and oxidative phosphorylation have often been used as a marker of differentiation status.

In this study, we aimed to understand the metabolic properties of PSCs during the differentiation process to become SCDHs. In accordance with previous reports, our results

demonstrated that hESCs had high glycolytic activity as compared to their SCDHs counterpart. We also observed a switch of metabolic states during differentiation, which resembles the reported changes of metabolism during embryonic liver development. Using a mechanistic kinetic model of cellular energy metabolism, we predicted that such metabolic switch might result from the change in the transcript levels of key glycolysis isozymes.

4.3 MATERIALS AND METHODS

4.3.1 Human Embryonic Stem Cell Culture.

The human embryonic stem cell (hESC) H9 cell line was cultured in feeder-free condition using TeSR™-E8™ media (STEMCELL-Technologies). The cells were maintained on 2% hESC-qualified Matrigel® (Corning) at 37°C and 5% CO_2. Cells were routinely passaged using 0.5 mM EDTA (Corning) after reaching 50-70% confluency and replated onto 2% hESC-qualified Matrigel for continued expansion.

4.3.2 Hepatocyte Differentiation.

After reaching approximately 70% confluency, differentiation was initiated as described previously [70]. Briefly, H9 cells were harvested using 0.5 mM EDTA and replated onto 2% Growth Factor Reduced Matrigel® (Corning) in TeSR™-E8™ media for 24h or until 70% confluency was reached. Differentiation was started by switching to the hepatocyte differentiation medium which consists of a mixture of low glucose DMEM (Gibco) and MCDB-201 (Sigma) (60:40 v/v). The differentiation medium was further supplemented with 26 µg/mL ascorbic acid 3-phosphate (Sigma), linoleic acid and bovine serum albumin (LA-BSA; Sigma; 0.25 mg/mL BSA, and 2.35 µg/mL linoleic acid), insulin-transferrin-selenium (ITS (Sigma), 2.5 µg/mL insulin, 1.38 µg/mL transferrin, 1.25 ng/mL sodium

selenium), 0.4 µg/mL dexamethasone (Sigma), 4.3 µg/mL β-mercaptoethanol (Hyclone), 100 IU/mL penicillin, and 100 µg/mL streptomycin (Gibco).

The differentiation medium was supplemented with stage specific growth factors: Stage 1, Activin A (100 ng/mL) and Wnt3a (50 ng/mL); stage 2, FGF2 (10 ng/mL) and BMP4 (50 ng/mL); stage 3, FGF8b (25 ng/mL), FGF1 (50 ng/mL), and FGF4 (10 ng/mL); and stage 4, HGF (20 ng/mL) and Follistatin (100 ng/mL). The differentiations were carried out at 21% O_2 and 5% CO_2.

4.3.3 Metabolite Measurement.

Spent medium was collected every other day to assess the concentration of different metabolites. Glucose level was measured using Infinity Glucose Hexokinase (Thermo), following the manufacturer's instruction. Lactate measurement was carried out using a lactate assay kit (Sigma), following the manufacturer's instruction. Oxygen concentration was measured with the NeoFox Software viewer using the NeoFox-GT fluorimeter coupled with the FOSPOR-R Oxygen Sensor probe (NeoFox). The metabolic consumption or production rates for each metabolite was calculated for each stage by measuring the concentration of the metabolites on different days throughout the stages of differentiation. The viable and total cell concentration were measured by cell counting using 0.4% trypan blue exclusion assay.

The specific rates of glucose consumption and lactate production were determined by:

Equation 5. Specific rates of glucose consumption and lactate production

$$r = \frac{S_t V_t - S_{t_0} V_{t_0}}{X(t - t_o)}$$

where S is the concentration of glucose or lactate in the medium at time t (S_t) or t_0 (S_{t0}), V is the volume of spent medium at time t (V_t) or t_0 (V_{t0}), X is the average cell number between time t and t_0.

4.3.4 Model Simulation

In this study, the kinetic metabolic model described previously [3, 21] was extended to include the rate expressions of the isoforms of key glycolysis enzymes, including glucose transporter (GLUT1-4), hexokinase (HK1-3 and GCK), phosphofructokinase (PFKL, PFKM and PFKP), pyruvate kinase (PKM1, PKM2, PKL and PKR), and lactate dehydrogenase (LDHA and LDHB). The net rate for each enzyme reaction was a weighted summation of all individual rates by its isozymes. The weighting factors (see Section 8.3.1) were estimated from the transcript levels of the corresponding isozymes using gene expression microarray data. The isozyme-specific kinetic parameters are described in detail in Section 8.3.1 of the Appendix Materials. The steady state solutions were obtained from the algebraic model using the same method described in Section 2.3.2.

4.4 RESULTS

4.4.1 Changes in Energy Metabolism during Differentiation

During HLC differentiation, glucose consumption on a per cell basis (i.e. specific glucose consumption rate) decreased progressively, accompanied by the decrease in lactate production. The molar ratio of lactate production to glucose consumption ($\Delta L/\Delta G$) also decreased from 1.30 ± 0.35 to 0.50 ± 0.18, and 0.26 ± 0.06 (mol/mol) in the first, second, and last stages of differentiation, respectively (Figure 13A). The drastic change in $\Delta L/\Delta G$ between the first two stages suggests a metabolic switch from the high to the low glycolytic flux state. Interestingly, this switch occurred with a simultaneous upturn in oxygen

consumption. The oxygen consumption rate increased from 1.50×10^{-10} mmol O_2/cell/h in the first stage to 2.29×10^{-10} mmol O_2/cell/h when cells were at the end of the differentiation (Figure 13B). The molar ratio of oxygen and glucose consumption increased from 1.21 ± 0.20 to 3.46 ± 0.41 (mol/mol), indicating a change from a high glycolytic to an oxidative metabolism.

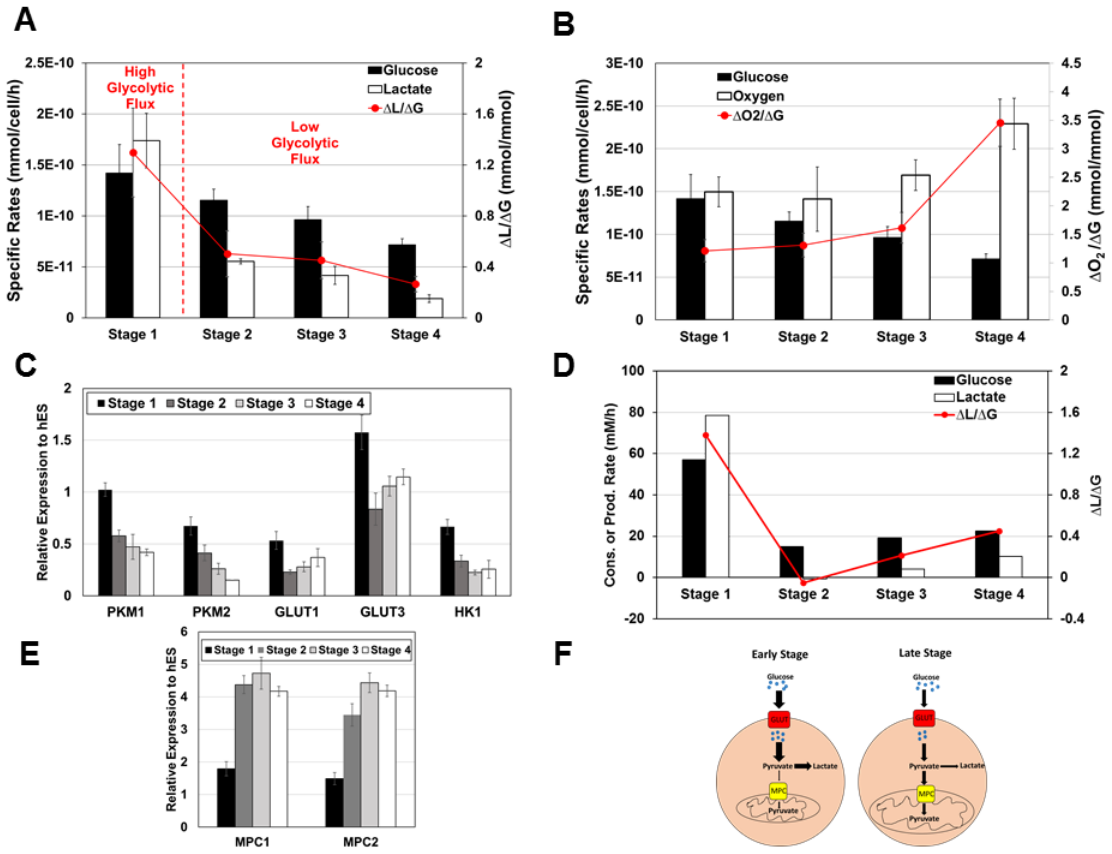

Figure 13. Metabolism Profiling of Cells during HLC Differentiation.
(A) Rates of glucose consumption (black bar) and lactate production (white bar) for cells during different stages of differentiation. The solid red line represents the molar ratio of lactate: glucose. (B) Rates of glucose consumption (black bar) and oxygen consumption (white bar) for cells during different stages of differentiation. The solid red line represents the molar ratio of oxygen: glucose. (C, E) Different metabolic isozyme levels were measured using qRT-PCR at different stages of differentiation. All error bars are represented as the standard deviation of three replicates. (D) Model predictions for rates of glucose consumption (black bar) and lactate production (white bar) during different stages of differentiation. The solid red line represents the molar ratio of lactate: glucose (F) Schematic of change in bioenergetic profiling for cells in early and late stages of differentiation. In the early stage, the rates of glucose consumption and lactate production were high. In the late stage, glucose consumption

decreased with a concomitant reduction of lactate production. At the same time, pyruvate transport into the mitochondria increased.

4.4.1 Effect of Isoform Composition on Flux State during Differentiation

Using the gene expression data of HLC differentiation, we examined the transcript dynamics of key glycolysis enzymes including their isoforms (Figure 14). A switch in isoform composition was not observed for most of the key glycolysis enzymes. Their predominant isoforms remained the same throughout the differentiation. The isozyme switch only occurred for phosphofructokinase and lactate dehydrogenase. In the first stage of differentiation, the muscle form of PFK (PFKM) was expressed at the highest level among three isoforms. However, as the differentiation progressed, the transcript level of this isoform decreased with an increasing level of the brain isoform PFKP. At the second stage, PFKP already became the predominant isoform and its expression increased monotonically towards the final stage of differentiation. The transcript dynamics of LDH isoforms were rather intriguing. In the first stage of differentiation, LDHB and LDHA were expressed at comparable levels. In the second and third stages, the expression level of LDHA decreased rapidly, making LDHB the predominant isoform. At the final stage of differentiation, LDHA transcript level increased markedly and became the dominant isoform of lactate dehydrogenase.

Incorporation of the transcript dynamics of key glycolysis isoenzymes into the kinetic model revealed multiple steady states behavior of glycolysis flux (Appendix Table 2). We first examined the effect of isoform levels of each enzyme on glycolysis flux. Despite the significant change in isoform level of GLUT3, the topology of glycolysis flux remained unchanged through different stages of differentiation. A decrease in the transcript levels of both HK1 and HK2 in the second stage led to the loss of bistability in glycolysis flux. For

a range of glucose concentration from 0.5 to 10 mM, the system could only operate at low flux states, marked by the low specific rates of glucose consumption and lactate production. In the third and fourth stages, both HK1 and HK2 were upregulated, the bistable region of glycolysis flux returned. The increase in PFKP and decrease in PFKM levels also caused a loss of bistability. Interestingly, because of the monotonic trends of these two isoforms, this metabolic behavior remained unchanged towards the final stage of differentiation. Changes in the PK isoform levels did not significantly alter the bistable region of glycolysis flux. However, the high flux state adopted a slightly lower glycolysis rate, which can be attributed to the changes in PKM1/2 levels (Figure 13C). Changes in LDH isoform levels did not affect the glycolysis flux behavior. When considering the changes in isoform levels of all of these enzymes, the behavior of glycolysis flux resembled the one obtained by only changing PFK isoform levels. The simulation result at the glucose concentration of 5 mM showed a switch from a high to a low glycolytic flux in the second stage (Figure 13D), similar to our experimental observations (Figure 13A).

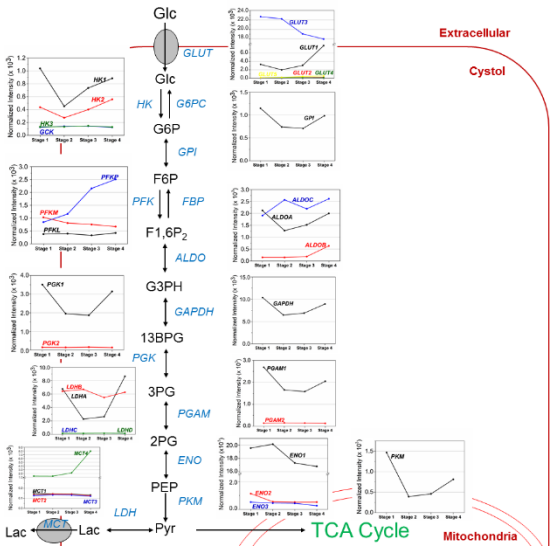

Figure 14. Transcript dynamics of glycolysis enzymes and their isoforms during HLC differentiation.

4.5 DISCUSSION

In this study, we showed that during hepatocyte differentiation of hESCs, the glycolytic activity decreases with a concurrent switch of metabolic states. The most drastic drop of glycolytic activity occurred during the transition between the first two stages of differentiation, wherein cells switched from a high to a low glycolytic flux state. Using the mechanistic metabolism model, we attributed this switch to the change in the isoform levels of key glycolysis enzymes, especially hexokinase and phosphofructokinase. Interestingly, in another study, a change in the expression of HK and PFK isozymes was shown to accompany the switch from a low flux state of somatic cells to a high flux state of induced pluripotent stem cells (iPSCs) [71].

The simulation result shows that a decrease in the expression levels of HK1 and HK2 caused the loss of high flux states in the examined range of glucose concentration (0.5-10 mM). Inside this range, glycolysis flux can thus only operate at a low flux state at any given glucose concentration. Attest to this result is the switch from a high to a low metabolic flux state observed in the second stage of differentiation.

A decrease in PFKM and an increase in PFKP levels also led to a loss of high flux states. Among three PFK isoforms, PFKM is the most sensitive to activation by fructose-1,6-biphosphate (F16BP, K_a = 0.35 mM) whereas PFKP is not activated by F16BP. In our previous study, we showed that feedback activation of PFK (M, L) by F16BP gives rise to the multiple steady state behavior [21]. Without this activation loop (i.e. in cells that do not express either PFKM or PFKL), glycolysis flux is less likely to confer multiple steady state behavior. In the current study, we further demonstrated that the multiple steady state

behavior remained unchanged even when cells have PFKM or PFKL given that the expression levels of these enzymes are low.

During the transition of hESCs towards the hepatic lineage, switch in isoform composition of key glycolysis enzymes is essential for certain metabolic functions of hepatocytes. The mechanistic metabolic model presented above provides insights into the role of isoform composition in regulating glycolytic activity and more importantly, metabolic switches during differentiation. At later stages of differentiation when hepatic cells begin to exhibit more active lipid metabolism, the glycolysis activity diminishes with a concurrent increase in TCA flux. The work conducted in this study can lay a foundation for the development of strategies to manipulate hESCs fate and lineage commitment to achieve more mature HLCs.

5 AN INTEGRATED PLATFORM FOR MUCIN-TYPE O-GLYCOSYLATION NETWORK GENERATION AND VISUALIZATION

5.1 SUMMARY

Mucin-type O-glycans have profound effects on the structure and stability of glycoproteins. O-glycans on the cell surface proteins also modulate the cell's interactions with the surrounding environments and other cells. The synthetic pathway of O-glycans involves a large number of enzymes with diverse substrate specificity. The expression pattern of these enzymes is cell and tissue-specific, thus making the pathway highly diverse. To facilitate the analysis of the pathway in a cell and tissue-specific fashion, we developed an integrated platform of RING (Rule Input Network Generator) and O-GlycoVis, a newly developed visualization program. RING uses an English-like reaction language to describe the substrate specificity of enzymes and additional constraints on the formation of the glycan products. Using this information, RING generates a list of possible glycans, which is used as input into O-Glycovis. O-GlycoVis displays the glycan distribution in the pathway and potential reaction paths leading to each glycan. With the input glycan data, O-Glycovis also traces all possible reaction paths leading to each glycan and outputs pathway maps with the relative abundance levels of glycans overlaid. O-glycan profiles from Chinese Hamster Ovary cells, Human Umbilical Vascular Endothelium cells, and two other breast cancer cell lines were used to illustrate the application of O-Glycovis.

5.2 INTRODUCTION

Mucin-type O-glycans (hereinafter referred to as O-glycans) are oligosaccharide moieties that are covalently attached to the serine or threonine residues of the protein. O-glycans are

abundantly present on cell surface proteins. They modulate the cell's interactions with the surrounding environment and other cells. O-glycans play an important role in cell-cell recognition in the immune system [72, 73]. Aberrant O-glycans on surface proteins of cancer cell lines change their adhesion characteristics and promote migration, invasion, and metastasis [74, 75]. O-glycans on secreted mucins contribute to the physical and chemical properties of mucins, enabling them to act as a general shield, protecting cells or tissues from direct contact with microorganisms [76].

O-glycans are also present in a number of glycoprotein therapeutics including recombinant erythropoietin [77], factor VIII [78], von Willebrand factor [79], and tumor necrosis factor receptor-Fc fusion protein [80]. They affect the stability, propensity to aggregation and pharmacokinetic properties of protein therapeutics (reviewed in [81]). In general, O-glycosylation of proteins is less characterized than N-glycosylation, largely because of the highly diversified nature of O-glycans and the technical challenges involved in the structural analysis of O-glycosylation.

O-glycosylation occurs mainly in the Golgi apparatus, albeit in tumor cells the initiation step might occur in the endoplasmic reticulum (ER) [82]. O-glycosylation is initiated by the transfer of an *N*-acetylgalactosamine (GalNAc) residue to the hydroxyl group of Ser or Thr in a peptide sequence, forming the Tn antigen structure (GalNAcαSer/Thr). The extension of the Tn antigen structure forms four major core structures (core 1-4). Core 1 is formed by the addition of a galactose to Tn antigen. The addition of an *N*-acetylglucosamine to the GalNAc of core 1 forms core 2. Core 3 results from the addition of a GlcNAc to Tn antigen. Core 4 is formed by branching of core 3 from its GalNAc with a β1-6GlcNAc. Core structures can be further extended to form complex O-glycans with

linear or branched chains. A typical O-glycan structure may contain ABO and Lewis blood group determinants, polysialic, i and I antigens. Repetition of LacNAc (type 1, type 2 and type 3) chains provides frameworks for further elaboration of O-glycan with additional monosaccharides or the described functional groups (see Table 1 for a list of common antigens).

Most O-glycosylation enzymes belong to one of the five groups: *N*-acetylgalactosaminyltransferases (GalNAcTs), *N*-acetylglucosaminlyltransferases (GlcNAcTs), galactosyltransferases (GalTs), sialyltransferases (SiaTs), and fucosyltransferases (FucTs). Each enzyme group can be further divided into several subgroups with distinct substrate specificities. For example, the polypeptide α-GalNAcT enzyme family catalyzes the addition of GalNAc to a Ser/Thr residue to initiate O-glycan synthesis on the protein backbone, while other GalNAcTs transfer GalNAc to GlcNAc or Gal to extend core structures. Similarly, some GlcNAcTs add GlcNAc to the GalNAc residue of Tn antigen to form core structures while others add GlcNAc to Gal, forming I or i antigen. GalTs add Gal to GalNAc or GlcNAc to form core 1 structure or type 1 and type 2 chains. SiaTs add *N*-Acetylneuraminic acid (Neu5Ac) to GalNAc and Gal to form α6- and α3-sialyl antigens. FucTs add fucose (Fuc) to Gal or GlcNAc to form various blood group antigens. The wide array of O-glycosylation enzymes and their manifold substrate specificities make O-glycosylation a highly diversified and complex biochemical network.

The expression pattern of O-glycosylation enzymes is cell and tissue-specific, making the O-glycosylation network also cell and tissue-specific. Computational tools prove useful to generate tissue- or cell-specific networks. A MATLAB-based framework was developed to construct the O-glycosylation network from five different glycosyltransferase activities

using a machine-readable definition for enzyme class with functional groups, linkages and substrate specificity [83, 84]. The resulting network was used to predict possible reaction paths leading to O-glycans on P-selectin glycoprotein ligand-1 (PSGL-1) of a human promyeloid cell line. A glycosyltransferase reaction library was constructed based on the substrate specificity reported previously in the literature [85]. Using this reaction library, a repertoire of possible glycan structures was predicted from the set of glycosyltransferases expressed in a human carcinoma cell line. More recently, [86] introduced a pattern-matching algorithm to generate the O-glycosylation networks based on 25 common glycosyl- and sulfotransferase activities. Through *in-silico* enzyme knockouts, the authors demonstrated the roles of each enzyme in the O-glycoform micro-heterogeneity.

Here, we report a framework for generation and analysis of O-glycosylation network using RING (Rule Input Network Generator) and O-GlycoVis, a newly developed visualization program. RING was previously used for studies of chemical systems [87, 88]. A unique feature of RING is its use of an English-like reaction language to describe substrate specificity and additional constraints on the formation of glycan products. Based on this user-input information, RING can predict all possible O-glycosylation reactions and glycan structures generated from thereof. O-GlycoVis then uses these inputs to display the network topology and overlay it with glycan structure information. O-GlycoVis can also predict possible glycan structures in the network from an input monosaccharide composition, identify the reaction paths leading to those glycans, and then map the relative abundance of glycans in an input profile to the reaction paths. O-GlycoVis is a Windows-based program, written in MATLAB® and freely available upon request.

Table 1. Classification of glycans in the O-glycosylation network of four cell lines based on the epitopes borne.

Epitope	SNFG representation	Percentage of glycan species bearing the epitope (%)			
		CHO	HUVEC	T47D	MCF7
Core 1 (and extended core 1) (a.k.a. Type 3 LacNAc chain)		5.1	1.2	96.6	2.8
Core 2 (and extended core 2)		94.1	98.3	0	96
Type 1 LacNAc chain		7.8	0	0	0
Type 2 LacNAc chain		47	92.6	0	76.7
i antigen	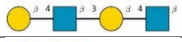	68.6	90	48.3	82.2
I antigen	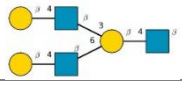	0	70.7	0	0
Blood group O/H		0	84.9	55.2	85.4
Blood group A		0	0	0	0
Blood group B		0	0	0	0
Sd^a/cad		49	0	13.8	0
Le^A		0	0	0	0
Le^B		0	0	0	0
Le^X		19.6	53.2	6.9	35.1
Le^Y		0	15	6.9	18.9
SLe^X	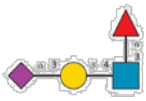	38.4	0	0	0
LacdiNAc		20.4	0	6.9	20

5.3 MATERIALS AND METHODS

The program consists of three main modules: reaction network generator (RING), glycan structure builder, and network visualizer as described below (Figure 15).

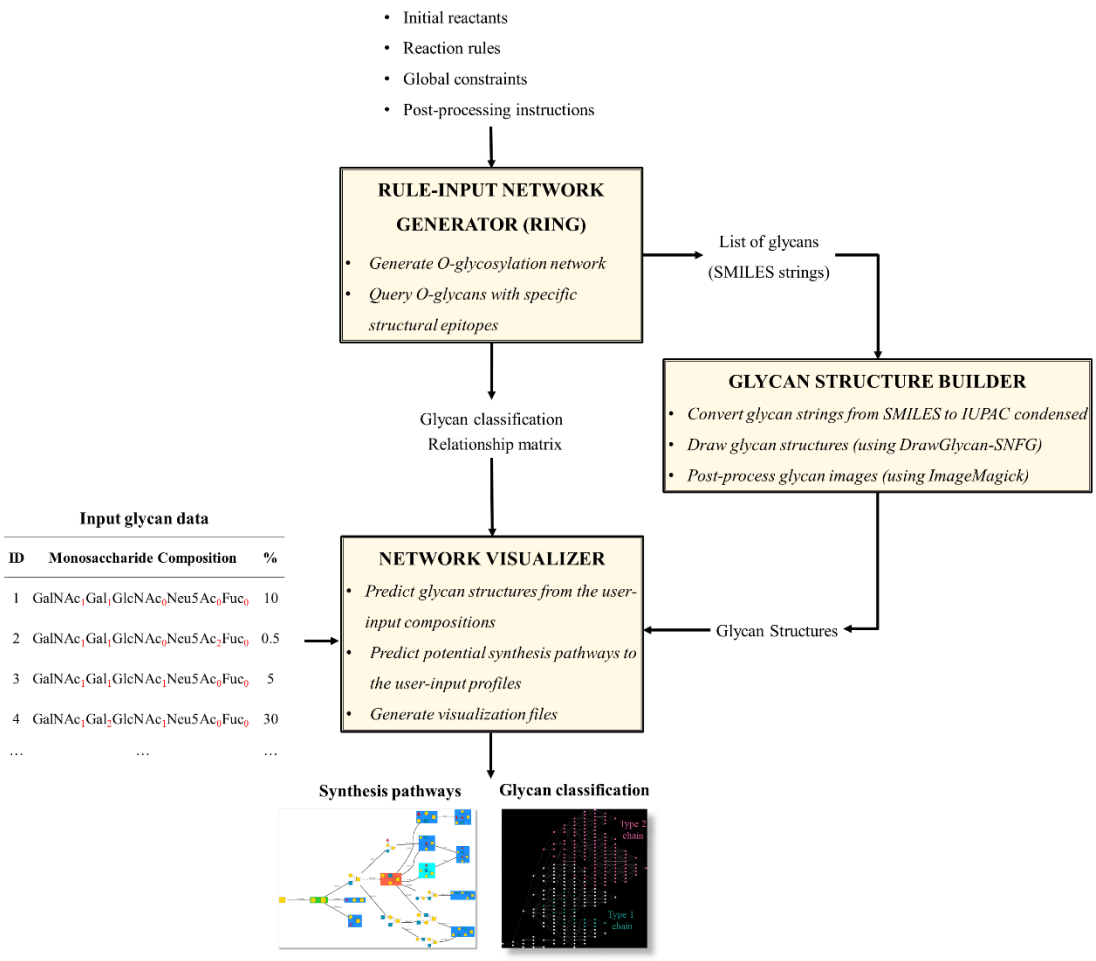

Figure 15. Input and output schematic for the platform used for mucin-type O-glycosylation network generation and visualization.

5.3.1 Rule Input Network Generator (RING)

For the generation of the O-glycosylation network, the inputs to the network generator are information on (1) initial reactants, (2) substrate specificity of all enzymes (reaction rules), (3) global constraints on glycans being formed, and (4) other post-processing instructions. These inputs are written in an English-like reaction language. Based on these inputs, the network generator then iteratively applies all the rules to the initial reactants and the products generated thereof. The output from the network generator is a list of all possible glycans and reactions consistent with the rules supplied by the user.

The initial reactants in the O-glycosylation model include a Ser/Thr residue on a polypeptide backbone and five nucleotide sugars (UDP-GalNAc, UDP-GlcNAc, UDP-Gal, CMP-Neu5Ac, and GDP-Fuc). The five nucleotide sugars provide the monosaccharides to be added to the extending O-glycans. An extending glycan on the protein may have more than one terminal monosaccharide that can receive a nucleotide sugar and form a glycosidic bond. The extending monosaccharide may have more than one carbon available for glycosidic bond formations. Furthermore, multiple nucleotide sugars may be capable of forming a glycosidic bond with the same hydroxyl carbon of the recipient monosaccharide. For example, UDP-Gal can be transferred to c3 or c4 of the GlcNAc residue on extending glycans to form β1-3 or β1-4 bond, respectively. The carbon c3 of GlcNAc can receive GDP-Fuc, UDP-GalNAc, UDP-Gal to form α1-3 or β1-3 bond. To deal with this complexity, each nucleotide sugar was represented as the sugar designator, plus designators for the type(s) of glycosidic bond that its carbonyl carbon can form as well as the carbons that are available for further glycan extension (Figure 16A).

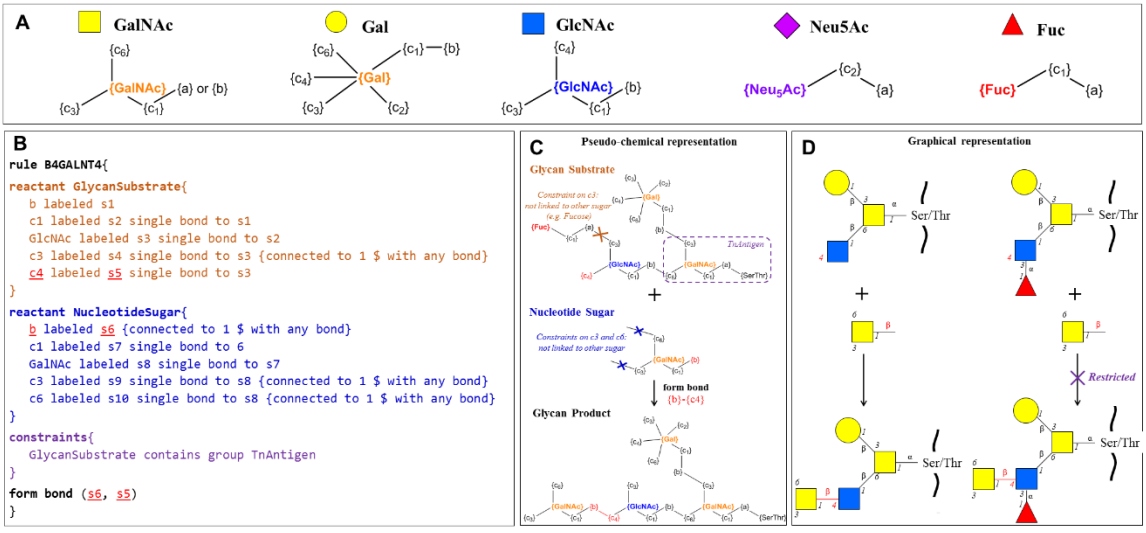

Figure 16. Illustration of an enzyme rule implemented in the O-glycosylation network

(A) Graphical and pseudo-chemical representations of nucleotide sugars. (B) An example of rule implementation in the O-glycosylation model. The rule describes structural requirements for the glycan to be extended (*GlycanSubstrate*) and the incoming nucleotide sugar (*NucleotideSugar*) in a reaction catalyzed by β1,4 N-acetylgalactosaminyltransferase 4 (B4GALNT4) enzyme. The *Glycan Substrate* must contain a terminal GlcNAc and the Tn antigen (GalNAcα-Ser/Thr) substructure. The *Nucleotide Sugar* must be UDP-GalNAc, shortened as GalNAc with an overhanging β-glycosidic "bond" connected to the carbonyl carbon c1 of GalNAc. The hydroxyl carbons c3 and c6 of GalNAc must not be linked with any other sugar. If all the requirements are satisfied, a β-glycosidic bond will be formed between s5 (hydroxyl carbon c4) of the *Glycan Substrate* and s6 (the overhanging β-glycosidic "bond") of the *Nucleotide Sugar* as stated in the "*form bond*" module. The product glycan will contain the *GalNAcβ1-4GlcNAc* substructure. (C) and (D) Pseudo-chemical and graphical representations of a reaction following the enzymatic rule defined in 2A. The pseudo-chemical representation was generated using the output from RING.

A reaction rule defines the structure requirements for two substrates, the receiving glycan to be extended and the incoming nucleotide sugar. The rule also specifies the carbon position of the glycosidic bond formed. The model consists of 32 reaction rules that describe the substrate specificity of common mammalian O-glycosyltransferases. Sulfotransferases were not considered in this work. The rules were derived from previous studies reported in the literature (see Appendix Table 3). Isozymes with similar substrate specificities were considered as one enzyme. For example, ST3GAL1 and ST3GAL2 were lumped because they both prefer the Gal residue of Galβ1-3GalNAc. Similarly, ST3GAL4 and ST3GAL6, both of which preferentially act on the Gal residue of type 2 chains, were also combined. All the isozymes that were combined are listed in Appendix Table 4. The effects of peptide sequence and charge on enzyme activity were neglected. Therefore, all the ppGalNAcTs were considered as having the same enzyme activity [89]. Figure 16B-D illustrates the implementation of one rule in the O-glycosylation model, whereby the structural requirements for two substrates are defined. One substrate is a glycan to be extended and the other is a nucleotide sugar.

Global constraints were implemented to restrict the formation of glycans to be within certain size or pattern. Most of these constraints prevent glycans with repetitive units to populate the network since they do not provide additional structural information. Five global constraints were imposed in the model (Appendix Table 5): (1) the maximal length of LacNAc chains on any glycan is two repeats; (2) a hybrid structure between type 1 and type 2 chains cannot be formed; (3) two consecutive I-antigens are not allowed in the system; (4) each monosaccharide can be linked to at most three other monosaccharides; (5) any carbon of a monosaccharide is connected with only one other monosaccharide.

Other post-processing instructions: Using the input, the program generates the reaction network and a list of all possible glycans. Each glycan is represented as a SMILES string [90], assigned a unique identification number (ID) and classified based on the borne epitopes (or structural patterns) defined in the post-processing instructions. All the glycan strings and their IDs are used as inputs of the glycan structure builder module. The relationship between glycans is stored in a matrix. Each row of the matrix corresponds to one reaction that occurred in the O-glycosylation network. Four columns of the matrix provide the IDs of the substrate and product glycans, the names and indices of rules involved in that reactions. The relationship matrix is an input of the network visualizer, aiding synthesis pathway identification.

5.3.2 Glycan Structure Builder

The SMILES format of output glycan strings from RING is not commonly used for glycan representation. We developed an algorithm to translate SMILES strings to the standard IUPAC-condensed nomenclature (Appendix Figure 3). The DrawGlycan-SNFG software [91] then converts all the output strings to graphical representations of glycans and store

them as image files. Each image file is automatically named according to the ID of the glycan it bears. ImageMagick then post-processes these image files for better visualization (e.g. crop and convert to background-transparent images).

5.3.3 Network Visualizer (O-GlycoVis)

O-GlycoVis is a Matlab based program developed for visualization of the O-glycosylation network. Using the glycan classification results as the input, O-GlycoVis interfaces with GraphViz to display the distribution of glycan epitopes in the O-glycosylation network. In the network display, each node represents a glycan and each edge depicts a reaction. Node colors (except for white) represent the epitopes that a glycan bears. If a glycan carries multiple epitopes, the node will be segmented into parts, each of which will be colored accordingly. Edges are colored by enzyme activities unless otherwise specified.

O-GlycoVis also predicts the synthesis pathway of input glycans. In this application, the module first retrieves the user-input information on the glycans and their abundances. Based on the monosaccharide composition of input glycans, the program identifies their IDs. A back-stepping algorithm is then used to identify all the immediate reactants leading to the input glycans (Figure 17). This process is repeated until the algorithm reaches the initial reactant glycan of the network. All the input glycans and their reactants are stored in a matrix whose two columns are the IDs of the substrate and product glycans. Each row of the matrix is one reaction step leading to the input glycan profiles. The matrix is used to create a pathway map, in which edges are labeled by the responsible reaction rules and nodes are colored by glycan abundances (percentages of the total glycan input).

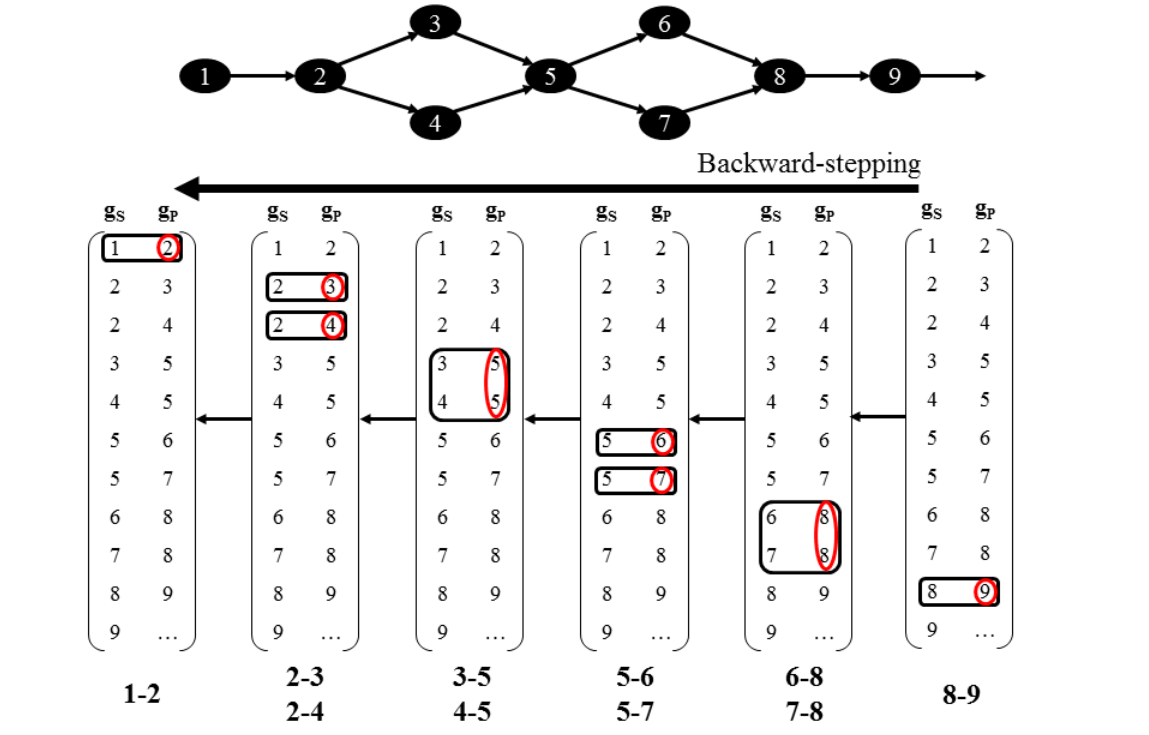

Figure 17. Backward-stepping Algorithm used in the program to identify all potential reaction pathways to synthesize an O-glycan (e.g. glycan #9).
g_s and g_p refer to substrate and product glycans of each glycosylation reaction.

5.4 RESULTS

5.4.1 O-Glycan Distribution in Chinese Hamster Ovary (CHO) Cells

The O-glycosyltransferase enzymes expressed in CHO cells were compiled using the RNA-Seq data of CHO-DG44 and CHO-K1 lines (Appendix Table 4). The enzymes that are expressed at the transcript level in both cell lines were used to construct the O-glycosylation network. The network generated consists of 255 glycan species and 557 reactions. The epitope(s) borne in each glycan was then identified using the program. Table 1 summarizes the results of glycan classification by epitopes. A total of nine common epitopes were found in glycans: (1) core 1 or extended core 1, (2) core 2 or extended core

2, (3) type 1 LacNAc, (4) type 2 LacNAc, (5) LacdiNAc structure or one of the following antigens: (6) Sd^a/Cad, (7) Lewis X (Le^X), (8) Sialyl-Lewis X (SLe^X) and (9) i antigen. Figure 18 displays the distribution of epitopes over the network. Glycans bearing more than one epitopes are represented as nodes with multiple colors (e.g. the terminal glycan g_T, as indicated by the circled nodes in Figure 18A-F. Its structure is shown in Appendix Figure 4). Core 3 and core 4 structures are not present in the network because CHO cells do not express β3-GnT6 enzyme. Similarly, I antigen was not formed because IGnT enzymes (GCNT2 and GCNT3) are not expressed. Lewis Y (Le^Y), blood groups ABO, Le^A, Le^B, and SLe^A were also absent because α2-FucTs (FUT1 and FUT2) and α4-FucT (FUT3) are not expressed.

Core 1 glycans constitute about 5% of the total number of species generated. The extension of core 1 glycan to core 2 vastly increases the glycan diversity (Figure 18A). Over 90% glycan species in the network have core 2 structure. Far more glycans have type 2 chain than type 1 chain (Figure 18B). The number of glycans that have type 1 chains is smaller because of the narrow substrate specificity of β3-GalT5, which only acts on the GlcNAc residues of core 2 (GlcNAcβ1-6GalNAc) and core 3 (GlcNAcβ1-3GalNAc) structures to form type 1 chains [92]. In comparison, β4-GalT, which catalyzes the formation of Galβ1-4GlcNAc of type 2 chains, has a broader substrate specificity. It accepts the GlcNAc residues of core 2/3 structures and β1,3GlcNAc residues of type 2 chains.

The representation of other epitopes in O-glycosylation network

The number of glycans with i antigen generated in the network far exceeds that with LacdiNAc structure (Figure 18C). The i antigen is formed by the addition of a β1,4Gal to GlcNAc residues of glycans through B4GALT enzymes catalyzed reactions. LacdiNAc

structure, however, is formed by the addition of a β1,4GalNAc to GlcNAc residues, catalyzed by B4GALNACT3,4. Interestingly, although B4GALNACT3,4 has a broader substrate specificity than B4GALT, the number of glycans bearing LacdiNAc is far less than those having i antigen. After GalNAc is added to the GlcNAc residue to form LacdiNAc, the chain growth is terminated. However, once the i antigen is formed, the newly added Gal residue can be further extended with another GlcNAc, Neu5Ac or GalNAc by B3GNT, ST3GAL, and B4GALNACT2, respectively. This increases the number of glycans having i antigen.

The program generated fewer glycans bearing Le^X antigen than that with SLe^X based on the O-glycosylation enzymes expressed in CHO cells, possibly due to the narrow substrate specificity of FUT4 (Figure 18D). FUT4 preferentially fucosylates the inner GlcNAc residue of type 2 chains to form Le^X [93, 94]. In other words, the enzyme prefers glycans having at least two consecutive LacNAc motifs (Galβ1-4GlcNAcβ1-). Less than 20% of glycans in the network satisfy this requirement because the global constraints restrict the length of LacNAc chains to only two repeats (see **Materials and Methods**). On the other hand, FUT7, which catalyzes SLe^X formation, accepts substrates with at least one LacNAc. The enzyme fucosylates the distal GlcNAc residues of sialylated glycans [citation]. Nearly 50% of glycans in the network comply with these structural requirements.

The number of glycans bearing Sd^a/Cad antigen is equivalent to that having type 2 chain and far exceeds that with type 1 chain (Figure 18E-F). Interestingly, about half of the Sd^a/Cad carrying glycans also have type 2 chain and vice versa, represented by nodes colored with both pink and yellow. On the other hand, less than 5% of glycans having Sd^a/Cad carry type 1 chain, indicated by dual-color nodes in Figure 18F. It should be noted

that all the glycans having both Sd^a/Cad and type 1 or type 2 chain are core 2 glycans with two arms (β1-6 and β1-3) on its structure. Sd^a/Cad is usually formed on one arm while type 1 or type 2 chain is on the other arm.

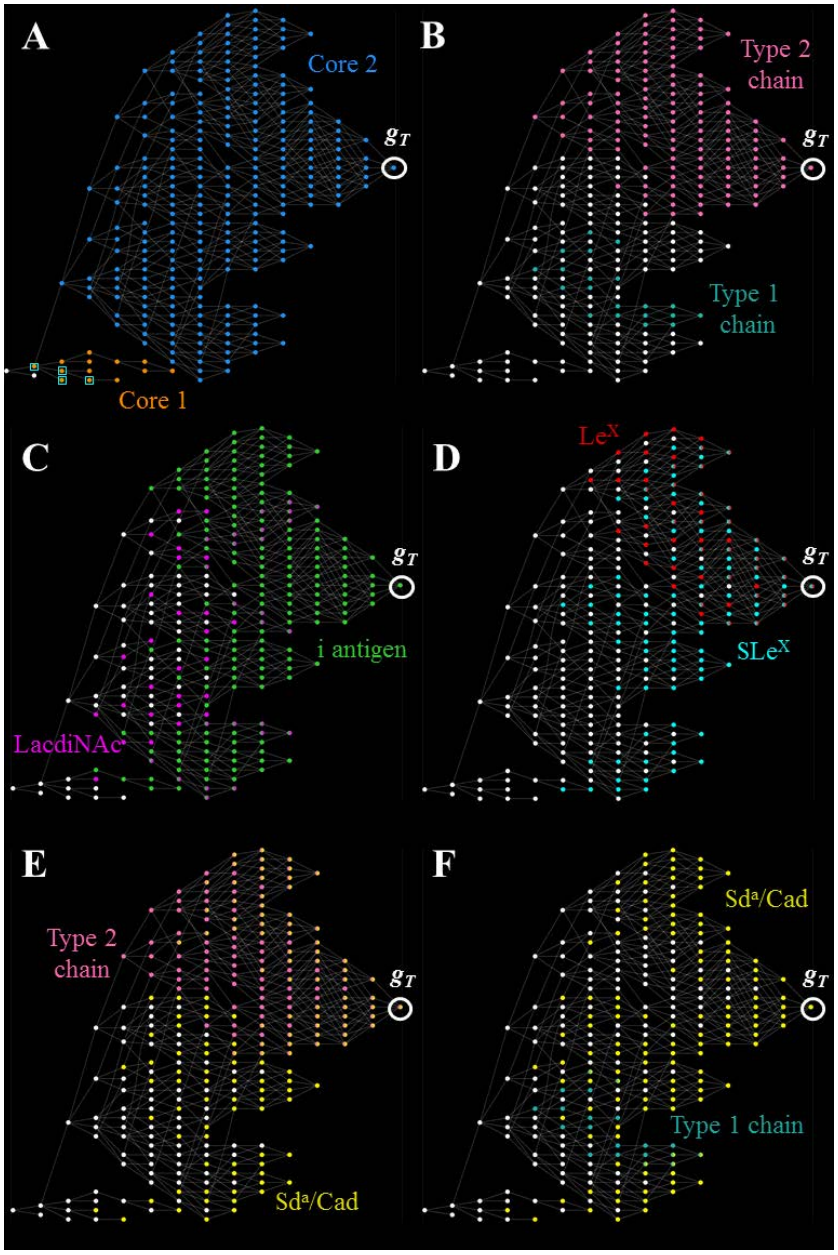

Figure 18. O-glycosylation network for CHO cells.
Highlighted nodes represent glycans bearing (A) core 1 (orange) and core 2 (blue) structures, (B) type 1 (teal) and type 2 (pink) chains, (C) LacdiNAc (purple) and i antigen (green), (D) Lewis X (red) and sialyl-Lewis X (aqua), (E) type 2 chain and Sd^a/Cad antigen (yellow), (F) type 1 chain and Sd^a/Cad antigen. Boxed nodes represent the reported O-glycans on the

recombinant MUC1(1.7TR)-IgG2a fusion protein produced in CHO cells. The circled node represents a terminal glycan g_T in the network. This node has multiple colors, indicating that the corresponding glycan carries more than one epitopes. The interactive network graph allows zooming in on the circled node to display its glycan structure (as shown in Appendix Figure 4).

Comparing the generated network with literature

We compared the O-glycosylation network generated for CHO cells to the reported O-glycans on the recombinant MUC1(1.7TR)-IgG2a fusion protein [95] produced in CHO cells. The detected glycans are noted by the boxed nodes in Figure 18A. Although a large number of glycans were predicted, only core 1, mono- and di-sialyl core 1 glycans were seen in the reported profile. Notably, core 2 glycans were not detected. However, importantly, all reported detected glycans were predicted in the network generated by the program. Although the glycosylation network generates a large number of intermediate glycans, not all accumulate to a detectable level and get excreted with the glycoprotein. Thus the number of predicted glycans is much larger than that detected. CHO cells express three core 2 enzymes. Two of them (C2GnT1 and 2) are expressed only at low levels. The other, C2GnT3, is expressed at a high level only in CHO-DG44. The absence of core 2 glycans could possibly be caused by several factors. The local protein structure may not be favorable for C2GnT3, or the enzyme may not be expressed at a high level in the CHO cell line used. It is also possible that the glycan was present at a low level but was not detected in glycan analysis.

5.4.2 O-Glycan Distribution in Human Umbilical Vein Endothelial Cells (HUVEC)

The O-glycosylation network for HUVEC was constructed based on the gene expression (RNAseq) data of glycosylation enzymes in the HUVEC TERT2 cells available from the

Human Protein Atlas version 18 [96]. The list of enzymes is shown in Appendix Table 4. The program generated a network of 515 glycans in 1210 reactions. Glycans in the network cover eight epitopes: (1) core 1 and (2) core 2 structures, (3) type 2 chain and other antigens including (4) Le^X, (5) Le^Y, (6) i, (7) I, and (8) blood group O/H. Similar to the O-glycosylation network of CHO cells, this network did not contain core 3 or 4 structure, blood group A or B, Le^A, and Le^B antigens because the responsible enzymes were not expressed. In addition, type 1 chain, blood group Sd^a/Cad, sLe^X, extended core 1 and LacdiNAc structures were not present because B3GALT5, B4GALNT2, FUT7, B3GNT3 and B4GALNT3,4 enzymes were not expressed. The abundance levels of predicted glycans harboring various epitopes are compared to networks predicted for other cells (Table 1). Similar to CHO cells, core 2 glycans are much more abundantly represented than core 1.

We compared the generated network with the reported O-glycan profile of HUVEC [97] (Appendix Table 6). Again, the program predicted far more glycans than detected. The program predicted 38 out of the 50 reported glycan structures (including isomers). We used O-Glycovis to identify the reaction paths from the starting glycan to the detected products along the generated a network (Figure 19A). Nodes along the reaction paths are colored yellow, and the edges are colored by the enzyme catalyzing the reaction step. The program generates an interactive graph that allows zooming in on a particular region of the network (Figure 19B), and visualizing the reactions that traverse a particular node with the structures of substrate and product glycans being displayed (Figure 19C).

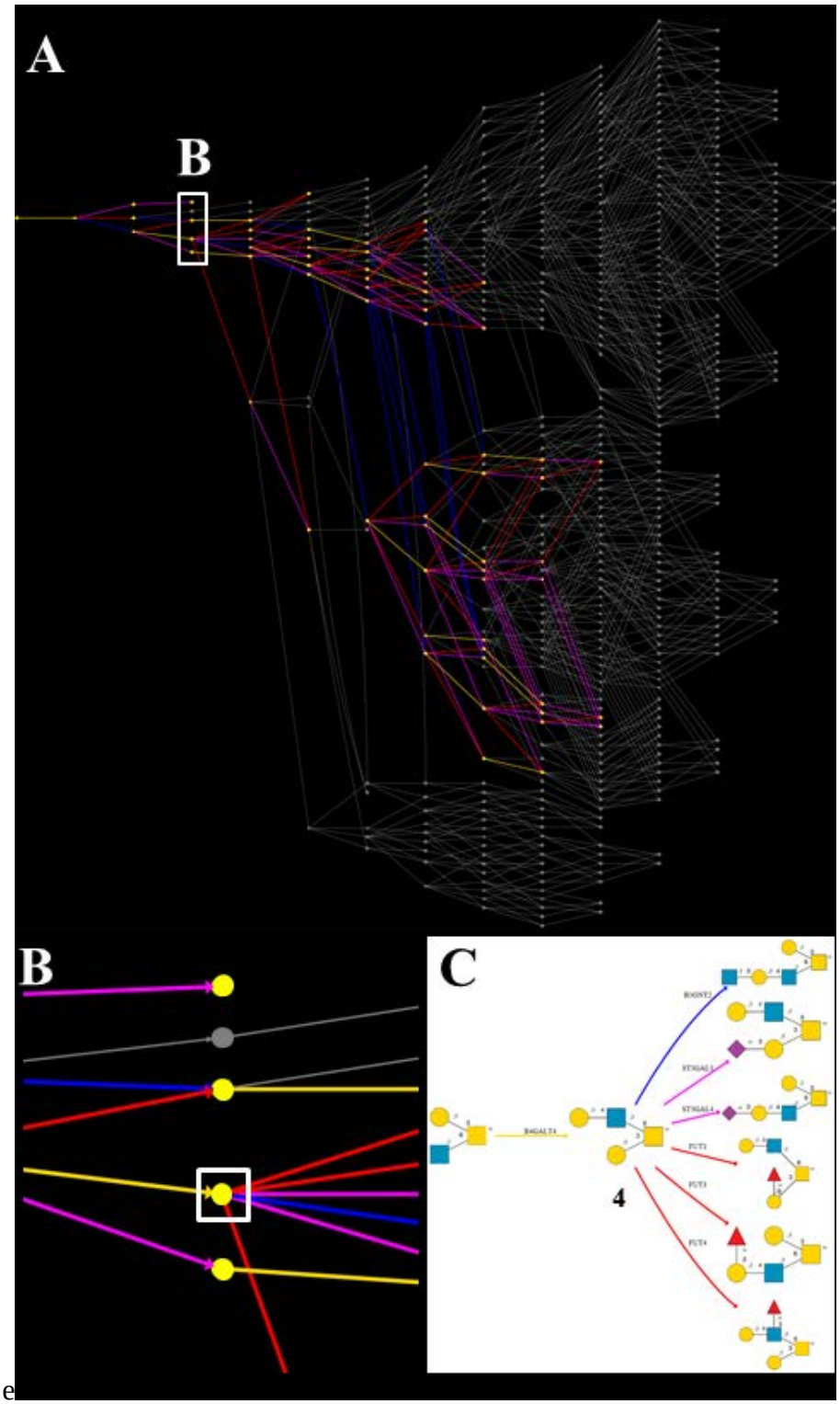

e

Figure 19. The program output using the HUVEC O-glycome profiling data.
(A) The O-glycosylation network predicted for HUVEC cells. Pathways proceed from left to right. The reaction paths leading to the reported glycans are highlighted. Nodes along the reaction paths are colored yellow, and the edges are colored by the enzyme catalyzing the

reaction step. (i.e. Gal-transferase: yellow; GlcNAc-transferase: blue; Fuc-transferase: red; Neu5Ac-transferase: purple). (B) Magnification view of the rectangular region B in A. (C) Magnification view of the rectangular region in B.

Among the twelve glycans that were not predicted by O-Glycovis, nine carries poly-LacNAc chains with three repeats of Galβ1-4GlcNAc, that exceeded the maximal length of two repeats imposed in the global constraints. Glycan #3 and #5 (Appendix Table 6, Appendix Figure 5) are formed by the transfer of Neu5Ac to GalNAc of asialylated core 1 structures, catalyzed by ST6GALNAC1,2 [98]. These two enzymes were not expressed in HUVEC TERT2 cells whose transcript profile was used to construct the network. All the reactions leading to glycan #30 were represented as the enzyme input into RING. The glycan is formed by sequential sialylation and fucosylation of the β1-6 arm of an extended core 2 structure (Appendix Figure 5). The glycan is absent in the predicted network because of the specification of reaction rules. Two synthesis routes lead to its formation with the reversed order of the two responsible enzymes: (1) FUT4-ST3GAL4, and (2) ST3GAL4-FUT4 (Appendix Figure 5). In our input rules, the route 1, sialylation of the terminal Gal residue by ST3GAL4, was blocked by prior fucosylation of the sub-terminal GlcNAc by FUT4 [96]. Another rule blocks route 2 because FUT4 activity toward the extending short sialyl-LacNAc chain was reported to be very weak [93]. By relaxing those rules glycan #30 can be generated.

5.4.3 O-Glycan Distribution in Breast Cancer Cells (T47D and MCF7)

Using the program, the O-glycosylation networks of two breast cancer cell lines T47D and MCF7 were predicted based on the glycosylation enzymes expression profile as revealed by the RNA-Seq data available from the Human Protein Atlas version 18 [96] (Appendix Table 4). The predicted network for T47D only consists of 29 glycans and 30 reactions. On the other hand, that for MCF7 has 858 glycans and 1906 reactions. The epitope

distribution of the O-glycans predicted in the two networks is shown in Table 1. The vast difference in the number of glycans generated between the two cell lines is also reflected in their epitope distribution.

The glycan profiles of secretory MUC1 reported for these two cell lines were also compared to the network prediction (Table 2). The program predicted all the reported glycan structures (4 and 11 for T47D and MCF7, respectively) and identified all possible pathways leading to such glycans. Figure 20A shows the enormous network predicted for MCF7, highlighting only the route leading to the reported glycans in T47D and MCF7 cells. Figure 20B and C show a simplified version of the output from O-Glycovis for T47D and MCF7 cells, respectively. The abundance level of the glycans is indicated by colors. The difference between the two networks is mainly due to the presence of core 2 enzymes, GCNT1, and GCNT3 in MCF7 cells line. Elimination of core 2 enzymes significantly reduced the size of the MCF7 network to somewhat similar to that of the T47D (i.e. 25 glycans and 26 reactions).

Table 2. Glycan profiles of secretory MUC1 reported for T47D and MCF7 cell lines.

Glycan ID Used in		Structure	% of the total profile	
[99]	Current work		T47D	MCF7
1	6		6.9	12.9
2	340	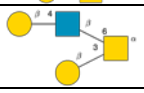	0	54.3
4	790		45.9	2.3
5	88		24.6	2.9
8	807	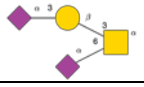	22.7	0
9	528	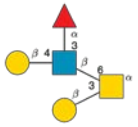	0	7.9
10	101	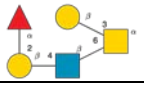	0	4.6

10’	342	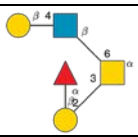	0	4.6
11	34	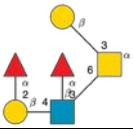	0	1.1
11’	534	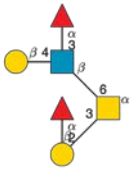	0	1.1
12	177	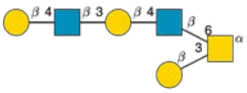	0	2.5
12’	339	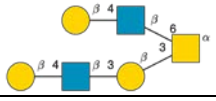	0	2.5

5.1 DISCUSSION

In this study, we employed RING to generate an O-glycosylation reaction network and integrate the output into O-GlycoVis for network visualization and analysis. The user inputs into RING are rules on the substrate specificity and the reaction of the glycosylation enzymes involved. We used the transcriptome data to decide on the enzymes to be included for each cell type evaluated. This is easily modified by users for any new cell line. RING predicts possible glycan structures generated in the O-glycosylation networks. Using the output from RING, O-GlycoVis generates network graphs that allow zooming into particular regions and nodes and displaying reactions that traverse one node with the structures of substrate and product glycans being shown. From an input monosaccharide composition, O-GlycoVis predicts the associated glycan structures and identifies the synthetic routes leading to each glycan. The abundance level of each glycan from an input profile can be overlaid onto the pathway map, assisting users to perform quantitative analysis of the glycan profile.

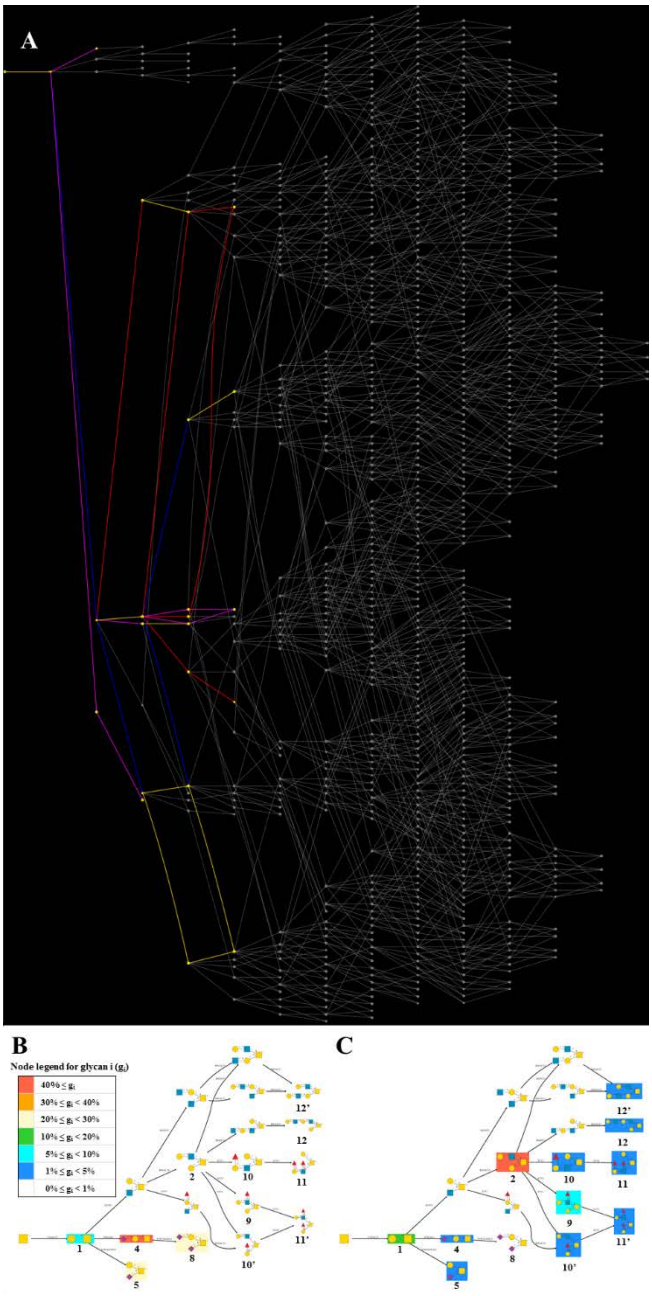

Figure 20. The program output using O-glycan profiling data from two breast cancer cell lines T47D and MCF7.
(A) The O-glycosylation network predicted for MCF7 cells. Pathways proceed from left to right. The reaction paths leading to the reported glycans in T47D and MCF7 cells are highlighted. Nodes along the reaction paths are colored yellow, and the edges are colored by the enzyme catalyzing the reaction step. (B) & (C) Pathway maps of cellular O-glycan biosynthesis in T47D and MCF7 cells, respectively. Glycan structures are highlighted according to their abundance levels in the glycan profile. The numbers below glycan structures are their corresponding IDs listed in the first column of Table 2.

The program bears some degree of similarity to GlycoVis, the visualization tool for N-glycosylation network [100]. However, there is a major difference between the two programs. N-glycosylation of recombinant therapeutic proteins follows a relatively fixed pathway of fix number of enzymes and reactions. Although some enzymes are represented by many isozymes with different substrate specificity, the basic network structure is not affected by those isoforms. In O-glycosylation, the number of enzymes is very large and the network generated in different cells or tissues can be vastly different as we have seen in the examples presented above. Hence, the O-GlycoVis is integrated with RING to facilitate O-glycosylation network generation and visualization in a tissue or cell-specific fashion.

A number of computational tools have been developed for the generation of glycosylation networks. A reaction pattern library was developed, which specifies the acceptor and donor monosaccharides and the linkage formed between them for a number of glycosyltransferases [85]. GNAT uses class-based inheritance to describe the enzyme substrate specificity [83]. Specifically, structural requirements on the substrate and product glycans of each glycosylation reaction are defined in different fields of an enzyme class or sub-class. O-Glycologue utilizes a set of pattern-matching rules to describe enzyme substrate specificity [86]. The program generates O-glycosylation networks by iterative application of such rules upon glycan strings. Glycan strings are represented using a one-letter code for monosaccharide and linkage. A similar approach was used to generate N-glycosylation networks, in which glycan structures are represented using modified LinearCode nomenclature [101]. RING can perform network generation with a similar capability to the aforementioned tools. Importantly, the English-like reaction language

used by RING allows simple description of glycan structures and substrate specificity of glycosylation enzymes. Like other network generating tools, the network generation step of RING may require a long computational time for a very large network that has a large number of global constraints imposed.

O-glycans are implicated in a variety of biological processes and human diseases. The structure of O-glycans affects the quality of therapeutic proteins. Better O-glycan characterization and a better control of O-glycosylation in protein and cell production will help generate high-quality products. The integrated platform reported here can help predict glycans generated in any particular cell line or tissue to facilitate the identification of glycans. Its versatility in projecting the network and tracing the reaction path will facilitate the development of strategies in glycoengineering.

6 CONCLUSION AND FUTURE DIRECTIONS

Energy metabolism has a profound impact on the outcome of cell culture processes. Elevated lactate production has a negative effect on cells' growth, viability, and productivity; reducing lactate production is thus of high importance to achieving desired process performance. This thesis presents mathematical modeling approaches to understand different behaviors energy metabolism. Insights from this study may provide new means for robust control of metabolism in mammalian cells culture.

In this study, we have demonstrated that the bistable behavior in glycolysis flux is implicated in several complex metabolic phenomena including the multiplicity of steady state in continuous culture, the metabolic switch to high lactate production in fed-batch culture and the switch to low flux state during hepatocyte differentiation. In fed-batch

cultures, the stimulation of PFKFB kinase activity due to AMPK activation under stress conditions affects the steady state topology of glycolysis flux. Lactate inhibition on glycolysis activity, to a certain extent, reverses the change in the steady state topology. Using the model, we investigated strategies to divert the culture from such undesired switch, which includes controlling glucose at low levels, adding lactate to the culture, inhibiting AMPK, and suppressing kinase activity of PFKFB. In continuous culture, bistability in glycolysis flux can be exploited to achieve a desired low flux state with high cell concentration. Two alternative approaches were proposed to guide a continuous culture towards this steady state. In hepatocyte differentiation, switch in isoform composition of key glycolysis enzymes alters the bistable behavior of steady state. Certain compositions, which are present in more differentiated counterparts of human embryonic stem cells (hESCs), cause a loss in the bistable behavior of glycolysis flux. Cells that possess such isoform compositions can only operate a low flux state for a wide range of glucose concentration. Model prediction was shown to be in agreement with experimental observations on changes of hESCs metabolism during differentiation.

Another challenge in cell culture process is to obtain proper and consistent glycosylation of the protein products. While N-glycans have been known to affect the biologics efficacy, (mucin-type) O-glycans have profound effects on the structure and stability of glycoproteins. The synthetic pathway of O-glycans in mammalian cells involves a large number of enzymes with cell-specific expression pattern. To facilitate the analysis of the pathway in a cell-specific fashion, we developed an integrated platform to generate the O-glycosylation networks of different cell lines. Using the generated networks, the synthetic

routes for input glycans were predicted. The platform holds potentials to facilitate the development of glycoengineering strategies.

The link between glucose metabolism and glycosylation patterns has been long known. Both N- and O-glycosylation (mucin-type) utilize nucleotide sugars that are synthesized from glucose-6-phosphate and fructose-6-phosphate, two metabolites of the glycolysis pathway. The concentration of these metabolites varies according to the glycolysis flux states. The kinetic model of energy metabolism presented in the current study can be linked with a model of nucleotide sugar pathways and eventually a glycosylation model to study the effects of glucose metabolism on the output glycan profile. Insights from this modeling effort can serve as a guideline for modulating metabolism to achieve desired glycosylation patterns.

7 REFERENCES

1. Le, H., et al., *Multivariate analysis of cell culture bioprocess data-Lactate consumption as process indicator.* Journal of Biotechnology, 2012. **162**(2-3): p. 210-223.
2. Charaniya, S., et al., *Mining manufacturing data for discovery of high productivity process characteristics.* Journal of Biotechnology, 2010. **147**(3-4): p. 186-197.
3. Mulukutla, B.C., et al., *Multiplicity of Steady States in Glycolysis and Shift of Metabolic State in Cultured Mammalian Cells.* Plos One, 2015. **10**(3).
4. Frame, K.K. and W.S. Hu, *Kinetic-Study of Hybridoma Cell-Growth in Continuous Culture .2. Behavior of Producers and Comparison to Nonproducers.* Biotechnology and Bioengineering, 1991. **38**(9): p. 1020-1028.
5. Frame, K.K. and W.S. Hu, *Kinetic-Study of Hybridoma Cell-Growth in Continuous Culture .1. A Model for Nonproducing Cells.* Biotechnology and Bioengineering, 1991. **37**(1): p. 55-64.
6. Hiller, G.W., et al., *A Kinetic-Analysis of Hybridoma Growth and Metabolism in Continuous Suspension-Culture on Serum-Free Medium.* Biotechnology and Bioengineering, 1991. **38**(7): p. 733-741.
7. Kurokawa, H., et al., *Kinetic-Study of Hybridoma Metabolism and Antibody-Production in Continuous-Culture Using Serum-Free Medium.* Journal of Fermentation and Bioengineering, 1993. **76**(2): p. 128-133.
8. Miller, W.M., H.W. Blanch, and C.R. Wilke, *A Kinetic-Analysis of Hybridoma Growth and Metabolism in Batch and Continuous Suspension-Culture - Effect of*

Nutrient Concentration, Dilution Rate, and Ph. Biotechnology and Bioengineering, 1988. **32**(8): p. 947-965.
9. Miller, W.M., C.R. Wilke, and H.W. Blanch, *Effects of Dissolved-Oxygen Concentration on Hybridoma Growth and Metabolism in Continuous Culture.* Journal of Cellular Physiology, 1987. **132**(3): p. 524-530.
10. Miller, W.M., C.R. Wilke, and H.W. Blanch, *The Transient Responses of Hybridoma Cells to Nutrient Additions in Continuous Culture .2. Glutamine Pulse and Step Changes.* Biotechnology and Bioengineering, 1989. **33**(4): p. 487-499.
11. Miller, W.M., C.R. Wilke, and H.W. Blanch, *Transient Responses of Hybridoma Cells to Nutrient Additions in Continuous Culture .1. Glucose Pulse and Step Changes.* Biotechnology and Bioengineering, 1989. **33**(4): p. 477-486.
12. Miller, W.M., C.R. Wilke, and H.W. Blanch, *Transient Responses of Hybridoma Cells to Lactate and Ammonia Pulse and Step Changes in Continuous Culture.* Bioprocess Engineering, 1988. **3**(3): p. 113-122.
13. Miller, W.M., C.R. Wilke, and H.W. Blanch, *Transient Responses of Hybridoma Metabolism to Changes in the Oxygen-Supply Rate in Continuous Culture.* Bioprocess Engineering, 1988. **3**(3): p. 103-111.
14. Warikoo, V., et al., *Integrated continuous production of recombinant therapeutic proteins.* Biotechnology and Bioengineering, 2012. **109**(12): p. 3018-3029.
15. Glacken, M.W., R.J. Fleischaker, and A.J. Sinskey, *Reduction of Waste Product Excretion Via Nutrient Control - Possible Strategies for Maximizing Product and Cell Yields on Serum in Cultures of Mammalian-Cells.* Biotechnology and Bioengineering, 1986. **28**(9): p. 1376-1389.
16. Zhou, W.C., J. Rehm, and W.S. Hu, *High Viable Cell Concentration Fed-Batch Cultures of Hybridoma Cells through Online Nutrient Feeding.* Biotechnology and Bioengineering, 1995. **46**(6): p. 579-587.
17. Europa, A.F., et al., *Multiple steady states with distinct cellular metabolism in continuous culture of mammalian cells.* Biotechnology and Bioengineering, 2000. **67**(1): p. 25-34.
18. Gambhir, A., et al., *Analysis of cellular metabolism of hybridoma cells at distinct physiological states.* Journal of Bioscience and Bioengineering, 2003. **95**(4): p. 317-327.
19. Altamirano, C., et al., *Analysis of CHO cells metabolic redistribution in a glutamate-based defined medium in continuous culture.* Biotechnology Progress, 2001. **17**(6): p. 1032-1041.
20. Follstad, B.D., et al., *Metabolic flux analysis of hybridoma continuous culture steady state multiplicity.* Biotechnology and Bioengineering, 1999. **63**(6): p. 675-683.
21. Mulukutla, B.C., et al., *Bistability in Glycolysis Pathway as a Physiological Switch in Energy Metabolism.* Plos One, 2014. **9**(6).
22. Mulquiney, P.J. and P.W. Kuchel, *Model of 2,3-bisphosphoglycerate metabolism in the human erythrocyte based on detailed enzyme kinetic equations: equations and parameter refinement.* Biochemical Journal, 1999. **342**: p. 581-596.
23. Wu, F., et al., *Computer modeling of mitochondrial tricarboxylic acid cycle, oxidative phosphorylation, metabolite transport, and electrophysiology.* Journal of Biological Chemistry, 2007. **282**(34): p. 24525-24537.

24. Monod, J., J. Wyman, and J.P. Changeux, *On Nature of Allosteric Transitions - a Plausible Model.* Journal of Molecular Biology, 1965. **12**(1): p. 88-&.
25. Korke, R., et al., *Large scale gene expression profiling of metabolic shift of mammalian cells in culture.* Journal of Biotechnology, 2004. **107**(1): p. 1-17.
26. Gambhir, A., et al., *Analysis of the use of fortified medium in continuous culture of mammalian cells.* Cytotechnology, 1999. **31**(3): p. 243-254.
27. Duran, J., et al., *Pfkfb3 is transcriptionally upregulated in diabetic mouse liver through proliferative signals.* Febs Journal, 2009. **276**(16): p. 4555-4568.
28. Manes, N.P. and M.R. El-Maghrabi, *The kinase activity of human brain 6-phosphofructo-2-kinase/fructose-2,6-bisphosphatase is regulated via inhibition by phosphoenolpyruvate.* Archives of Biochemistry and Biophysics, 2005. **438**(2): p. 125-136.
29. Novellasdemunt, L., et al., *Akt-dependent Activation of the Heart 6-Phosphofructo-2-kinase/Fructose-2,6-bisphosphatase (PFKFB2) Isoenzyme by Amino Acids.* Journal of Biological Chemistry, 2013. **288**(15): p. 10640-10651.
30. Mulukutla, B.C., M. Gramer, and W.S. Hu, *On metabolic shift to lactate consumption in fed-batch culture of mammalian cells.* Metab Eng, 2012. **14**(2): p. 138-49.
31. Young, J.D., *Metabolic flux rewiring in mammalian cell cultures.* Current Opinion in Biotechnology, 2013. **24**(6): p. 1108-1115.
32. Borys, M.C., D.I.H. Linzer, and E.T. Papoutsakis, *Ammonia Affects the Glycosylation Patterns of Recombinant Mouse Placental Lactogen-1 by Chinese-Hamster Ovary Cells in a Ph-Dependent Manner.* Biotechnology and Bioengineering, 1994. **43**(6): p. 505-514.
33. Butler, M., *Optimisation of the cellular metabolism of glycosylation for recombinant proteins produced by mammalian cell systems.* Cytotechnology, 2006. **50**(1-3): p. 57-76.
34. Hayter, P.M., et al., *The Effect of the Dilution Rate on Cho Cell Physiology and Recombinant Interferon-Gamma Production in Glucose-Limited Chemostat Culture.* Biotechnology and Bioengineering, 1993. **42**(9): p. 1077-1085.
35. Muthing, J., et al., *Effects of buffering conditions and culture pH on production rates and glycosylation of clinical phase I anti-melanoma mouse IgG3 monoclonal antibody R24.* Biotechnology and Bioengineering, 2003. **83**(3): p. 321-334.
36. Yongky, A., et al., *Mechanism for multiplicity of steady states with distinct cell concentration in continuous culture of mammalian cells.* Biotechnology and Bioengineering, 2015. **112**(7): p. 1437-1445.
37. Jeon, S.M., N.S. Chandel, and N. Hay, *AMPK regulates NADPH homeostasis to promote tumour cell survival during energy stress.* Nature, 2012. **485**(7400): p. 661-+.
38. Salt, I.P., et al., *AMP-activated protein kinase is activated by low glucose in cell lines derived from pancreatic beta cells, and may regulate insulin release.* Biochemical Journal, 1998. **335**: p. 533-539.
39. Gaglio, D., et al., *Glutamine Deprivation Induces Abortive S-Phase Rescued by Deoxyribonucleotides in K-Ras Transformed Fibroblasts.* Plos One, 2009. **4**(3).

40. Zhu, Y.H., et al., *L-Glutamine deprivation induces autophagy and alters the mTOR and MAPK signaling pathways in porcine intestinal epithelial cells.* Amino Acids, 2015. **47**(10): p. 2185-2197.
41. Marsin, A.S., et al., *Phosphorylation and activation of heart PFK-2 by AMPK has a role in the stimulation of glycolysis during ischaemia.* Current Biology, 2000. **10**(20): p. 1247-1255.
42. Ghislat, G., et al., *Withdrawal of Essential Amino Acids Increases Autophagy by a Pathway Involving Ca2+/Calmodulin-dependent Kinase Kinase-beta (CaMKK-beta).* Journal of Biological Chemistry, 2012. **287**(46): p. 38625-38636.
43. Fryer, L.G.D., A. Parbu-Patel, and D. Carling, *The anti-diabetic drugs rosiglitazone and metformin stimulate AMP-activated protein kinase through distinct signaling pathways.* Journal of Biological Chemistry, 2002. **277**(28): p. 25226-25232.
44. Segel, I.H., *Enzyme kinetics: behavior and analysis of rapid equilibrium and steady state enzyme systems*. 1975, New York: Wiley.
45. Leite, T.C., et al., *Lactate favours the dissociation of skeletal muscle 6-phosphofructo-1-kinase tetramers down-regulating the enzyme and muscle glycolysis.* Biochemical Journal, 2007. **408**: p. 123-130.
46. Leite, T.C., et al., *Lactate downregulates the glycolytic enzymes hexokinase and phosphofructokinase in diverse tissues from mice.* Febs Letters, 2011. **585**(1): p. 92-98.
47. Hardie, D.G., F.A. Ross, and S.A. Hawley, *AMPK: a nutrient and energy sensor that maintains energy homeostasis.* Nature Reviews Molecular Cell Biology, 2012. **13**(4): p. 251-262.
48. Marsin, A.S., et al., *The stimulation of glycolysis by hypoxia in activated monocytes is mediated by AMP-activated protein kinase and inducible 6-phosphofructo-2-kinase.* Journal of Biological Chemistry, 2002. **277**(34): p. 30778-30783.
49. Almeida, A., S. Moncada, and J.P. Bolanos, *Nitric oxide switches on glycolysis through the AMP protein kinase and 6-phosphofructo-2-kinase pathway.* Nature Cell Biology, 2004. **6**(1): p. 45-U9.
50. Barnes, K., et al., *Activation of GLUT1 by metabolic and osmotic stress: potential involvement of AMP-activated protein kinase (AMPK).* Journal of Cell Science, 2002. **115**(11): p. 2433-2442.
51. Kurth-Kraczek, E.J., et al., *5 ' AMP-activated protein kinase activation causes GLUT4 translocation in skeletal muscle.* Diabetes, 1999. **48**(8): p. 1667-1671.
52. Roelandt, P., et al., *Human embryonic and rat adult stem cells with primitive endoderm-like phenotype can be fated to definitive endoderm, and finally hepatocyte-like cells.* PLoS One, 2010. **5**(8): p. e12101.
53. Song, Z., et al., *Efficient generation of hepatocyte-like cells from human induced pluripotent stem cells.* Cell Res, 2009. **19**(11): p. 1233-42.
54. Si-Tayeb, K., et al., *Highly efficient generation of human hepatocyte-like cells from induced pluripotent stem cells.* Hepatology, 2010. **51**(1): p. 297-305.
55. Touboul, T., et al., *Generation of functional hepatocytes from human embryonic stem cells under chemically defined conditions that recapitulate liver development.* Hepatology, 2010. **51**(5): p. 1754-65.

56. Baxter, M., et al., *Phenotypic and functional analyses show stem cell-derived hepatocyte-like cells better mimic fetal rather than adult hepatocytes.* J Hepatol, 2015. **62**(3): p. 581-9.
57. Godoy, P., et al., *Gene networks and transcription factor motifs defining the differentiation of stem cells into hepatocyte-like cells.* J Hepatol, 2015. **63**(4): p. 934-42.
58. Jozefczuk, J., et al., *Comparative analysis of human embryonic stem cell and induced pluripotent stem cell-derived hepatocyte-like cells reveals current drawbacks and possible strategies for improved differentiation.* Stem Cells Dev, 2011. **20**(7): p. 1259-75.
59. Li, T., et al., *Multi-stage analysis of gene expression and transcription regulation in C57/B6 mouse liver development.* Genomics, 2009. **93**(3): p. 235-42.
60. Chung, S., et al., *Glycolytic network restructuring integral to the energetics of embryonic stem cell cardiac differentiation.* Journal of Molecular and Cellular Cardiology, 2010. **48**(4): p. 725-734.
61. Zhang, J., et al., *UCP2 regulates energy metabolism and differentiation potential of human pluripotent stem cells.* Embo Journal, 2011. **30**(24): p. 4860-4873.
62. Varum, S., et al., *Energy Metabolism in Human Pluripotent Stem Cells and Their Differentiated Counterparts.* Plos One, 2011. **6**(6).
63. Pan, C., et al., *Comparative proteomic phenotyping of cell lines and primary cells to assess preservation of cell type-specific functions.* Mol Cell Proteomics, 2009. **8**(3): p. 443-50.
64. Chan, C., et al., *Metabolic pre-conditioning of cultured cells in physiological levels of insulin: generating resistance to the lipid-accumulating effects of plasma in hepatocytes.* Biotechnol Bioeng, 2002. **78**(7): p. 753-60.
65. Chan, C., et al., *Metabolic flux analysis of cultured hepatocytes exposed to plasma.* Biotechnol Bioeng, 2003. **81**(1): p. 33-49.
66. Kantrow, S.P., et al., *Oxidative metabolism in rat hepatocytes and mitochondria during sepsis.* Arch Biochem Biophys, 1997. **345**(2): p. 278-88.
67. Jones, D.P. and H.S. Mason, *Gradients of O2 concentration in hepatocytes.* J Biol Chem, 1978. **253**(14): p. 4874-80.
68. Schumacker, P.T., N. Chandel, and A.G. Agusti, *Oxygen conformance of cellular respiration in hepatocytes.* Am J Physiol, 1993. **265**(4 Pt 1): p. L395-402.
69. Kekonen, E.M., V.P. Jauhonen, and I.E. Hassinen, *Oxygen and substrate dependence of hepatic cellular respiration: sinusoidal oxygen gradient and effects of ethanol in isolated perfused liver and hepatocytes.* J Cell Physiol, 1987. **133**(1): p. 119-26.
70. Raju, R., et al., *Cell Expansion During Directed Differentiation of Stem Cells Toward the Hepatic Lineage.* Stem Cells Dev, 2017. **26**(4): p. 274-284.
71. Folmes, C.D.L., et al., *Somatic Oxidative Bioenergetics Transitions into Pluripotency-Dependent Glycolysis to Facilitate Nuclear Reprogramming.* Cell Metabolism, 2011. **14**(2): p. 264-271.
72. Ellies, L.G., et al., *Core 2 oligosaccharide biosynthesis distinguishes between selectin ligands essential for leukocyte homing and inflammation.* Immunity, 1998. **9**(6): p. 881-890.

73. Mitoma, J., et al., *Critical functions of N-glycans in L-selectin-mediated lymphocyte homing and recruitment.* Nature Immunology, 2007. **8**(4): p. 409-418.
74. Julien, S., et al., *Stable expression of sialyl-Tn antigen in T47-D cells induces a decrease of cell adhesion and an increase of cell migration.* Breast Cancer Research and Treatment, 2005. **90**(1): p. 77-84.
75. Pinho, S., et al., *Biological significance of cancer-associated sialyl-Tn antigen: Modulation of malignant phenotype in gastric carcinoma cells.* Cancer Letters, 2007. **249**(2): p. 157-170.
76. Johansson, M.E.V., et al., *Composition and functional role of the mucus layers in the intestine.* Cellular and Molecular Life Sciences, 2011. **68**(22): p. 3635-3641.
77. Dube, S., J.W. Fisher, and J.S. Powell, *Glycosylation at Specific Sites of Erythropoietin Is Essential for Biosynthesis, Secretion, and Biological Function.* Journal of Biological Chemistry, 1988. **263**(33): p. 17516-17521.
78. Thim, L., et al., *Purification and characterization of a new recombinant factor VIII (N8).* Haemophilia, 2010. **16**(2): p. 349-359.
79. van Schooten, C.J.M., et al., *Variations in glycosylation of von Willebrand factor with O-linked sialylated T antigen are associated with its plasma levels.* Blood, 2007. **109**(6): p. 2430-2437.
80. Houel, S., et al., *N- and O-Glycosylation Analysis of Etanercept Using Liquid Chromatography and Quadrupole Time-of-Flight Mass Spectrometry Equipped with Electron-Transfer Dissociation Functionality.* Analytical Chemistry, 2014. **86**(1): p. 576-584.
81. Van den Steen, P., et al., *Concepts and principles of O-linked glycosylation.* Critical Reviews in Biochemistry and Molecular Biology, 1998. **33**(3): p. 151-208.
82. Gill, D.J., et al., *Initiation of GalNAc-type O-glycosylation in the endoplasmic reticulum promotes cancer cell invasiveness.* Proc Natl Acad Sci U S A, 2013. **110**(34): p. E3152-E3161.
83. Liu, G., A. Puri, and S. Neelamegham, *Glycosylation Network Analysis Toolbox: a MATLAB-based environment for systems glycobiology.* Bioinformatics, 2013. **29**(3): p. 404-406.
84. Liu, G. and S. Neelamegham, *A Computational Framework for the Automated Construction of Glycosylation Reaction Networks.* Plos One, 2014. **9**(6).
85. Kawano, S., et al., *Prediction of glycan structures from gene expression data based on glycosyltransferase reactions.* Bioinformatics, 2005. **21**(21): p. 3976-3982.
86. McDonald, A.G., K.F. Tipton, and G.P. Davey, *A Knowledge-Based System for Display and Prediction of O-Glycosylation Network Behaviour in Response to Enzyme Knockouts.* Plos Computational Biology, 2016. **12**(4).
87. Rangarajan, S., A. Bhan, and P. Daoutidis, *Language-oriented rule-based reaction network generation and analysis: Description of RING.* Computers & Chemical Engineering, 2012. **45**: p. 114-123.
88. Rangarajan, S., A. Bhan, and P. Daoutidis, *Language-oriented rule-based reaction network generation and analysis: Applications of RING.* Computers & Chemical Engineering, 2012. **46**: p. 141-152.
89. Zhang, L., E. Tian, and K.G. Ten Hagen *UDP-N-Acetyl-Alpha-D-Galactosamine: Polypeptide N-Acetylgalactosaminyltransferases (ppGalNAc-Ts),* in *Handbook of*

Glycosyltransferases and Related Genes, N. Taniguchi, et al., Editors. 2014, Springer Japan: Tokyo. p. 495-511.
90. Weininger, D., *Smiles, a Chemical Language and Information-System .1. Introduction to Methodology and Encoding Rules.* Journal of Chemical Information and Computer Sciences, 1988. **28**(1): p. 31-36.
91. Cheng, K., Y.S. Zhou, and S. Neelamegham, *DrawGlycan-SNFG: a robust tool to render glycans and glycopeptides with fragmentation information.* Glycobiology, 2017. **27**(3): p. 200-205.
92. Holgersson, J. and J. Lofling, *Glycosyltransferases involved in type 1 chain and Lewis antigen biosynthesis exhibit glycan and core chain specificity.* Glycobiology, 2006. **16**(7): p. 584-593.
93. Niemela, R., et al., *Complementary acceptor and site specificities of Fuc-TIV and Fuc-TVII allow effective biosynthesis of sialyl-TriLex and related polylactosamines present on glycoprotein counterreceptors of selectins.* Journal of Biological Chemistry, 1998. **273**(7): p. 4021-4026.
94. Nishihara, S., et al., *Alpha1,3-fucosyltransferase 9 (FUT9; Fuc-TIX) preferentially fucosylates the distal GlcNAc residue of polylactosamine chain while the other four alpha1,3FUT members preferentially fucosylate the inner GlcNAc residue.* Febs Letters, 1999. **462**(3): p. 289-94.
95. Olson, F.J., et al., *A MUC1 tandem repeat reporter protein produced in CHO-K1 cells has sialylated core 1 O-glycans and becomes more densely glycosylated if coexpressed with polypeptide-GalNAc-T4 transferase.* Glycobiology, 2005. **15**(2): p. 177-91.
96. Uhlen, M., et al., *A pathology atlas of the human cancer transcriptome.* Science, 2017. **357**(6352): p. 660-+.
97. Kudelka, M.R., et al., *Cellular O-Glycome Reporter/Amplification to explore O-glycans of living cells.* Nature Methods, 2016. **13**(1): p. 81-+.
98. Ikehara, Y., et al., *Cloning and expression of a human gene encoding an N-acetylgalactosamine-alpha2,6-sialyltransferase (ST6GalNAc I): a candidate for synthesis of cancer-associated sialyl-Tn antigens.* Glycobiology, 1999. **9**(11): p. 1213-24.
99. Muller, S. and F.G. Hanisch, *Recombinant MUC1 probe authentically reflects cell-specific O-glycosylation profiles of endogenous breast cancer mucin - High density and prevalent core 2-based glycosylation.* Journal of Biological Chemistry, 2002. **277**(29): p. 26103-26112.
100. Hossler, P., L.T. Goh, and M.M.a.H.W.S. Lee, *GlycoVis: visualizing glycan distribution in the protein N-glycosylation pathway in mammalian cells.* Biotechnology and Bioengineering, 2006. **95**: p. 946-960.
101. Krambeck, F.J., et al., *A mathematical model to derive N-glycan structures and cellular enzyme activities from mass spectrometric data.* Glycobiology, 2009. **19**(11): p. 1163-75.
102. Brockhausen, I., *Biosynthesis of Complex Mucin-Type O-Glycans.* Comprehensive Natural Products II: Chemistry and Biology, Vol 6: Carbohydrates, Nucleosides & Nucleic Acids, 2010: p. 315-350.
103. Montiel, M.D., et al., *Molecular cloning, gene organization and expression of the human UDP-GalNAc:Neu5Acalpha2-3Galbeta-R beta1,4-N-*

acetylgalactosaminyltransferase responsible for the biosynthesis of the blood group Sda/Cad antigen: evidence for an unusual extended cytoplasmic domain. Biochemical Journal, 2003. **373**(Pt 2): p. 369-79.
104. Zerfaoui, M., et al., *alpha(1,2)-Fucosylation prevents sialyl Lewis x expression and E-selectin-mediated adhesion of fucosyltransferase VII-transfected cells.* Eur J Biochem, 2000. **267**(1): p. 53-60.
105. Gotoh, M., et al., *Molecular cloning and characterization of beta1,4-N-acetylgalactosaminyltransferases IV synthesizing N,N'-diacetyllactosediamine.* Febs Letters, 2004. **562**(1-3): p. 134-40.
106. Hakomori, S.-i. and M. Palcic, *Histo-Blood Group A and B Transferases, Their Gene Structures, and Common O Group Gene Structures*, in *Handbook of Glycosyltransferases and Related Genes*, N. Taniguchi, et al., Editors. 2014, Springer Japan: Tokyo. p. 463-477.
107. Brockhausen, I., et al., *Control of O-glycan synthesis: specificity and inhibition of O-glycan core 1 UDP-galactose:N-acetylgalactosamine-alpha-R beta 3-galactosyltransferase from rat liver.* Biochem Cell Biol, 1992. **70**(2): p. 99-108.
108. Brockhausen, I., et al., *UDP-Gal: GlcNAc-R beta1,4-galactosyltransferase--a target enzyme for drug design. Acceptor specificity and inhibition of the enzyme.* Glycoconj J, 2006. **23**(7-8): p. 525-41.
109. Ujita, M., et al., *Poly-N-acetyllactosamine extension in N-glycans and core 2- and core 4-branched O-glycans is differentially controlled by i-extension enzyme and different members of the beta 1,4-galactosyltransferase gene family.* J Biol Chem, 2000. **275**(21): p. 15868-75.
110. Ujita, M., et al., *Regulation of I-branched poly-N-acetyllactosamine synthesis. Concerted actions by I-extension enzyme, I-branching enzyme, and beta1,4-galactosyltransferase I.* J Biol Chem, 1999. **274**(14): p. 9296-304.
111. Kuhns, W., et al., *Processing O-glycan core 1, Gal beta 1-3GalNAc alpha-R. Specificities of core 2, UDP-GlcNAc: Gal beta 1-3 GalNAc-R(GlcNAc to GalNAc) beta 6-N-acetylglucosaminyltransferase and CMP-sialic acid: Gal beta 1-3GalNAc-R alpha 3-sialyltransferase.* Glycoconj J, 1993. **10**(5): p. 381-94.
112. Kuhns, W., et al., *Characterization of a novel mucin sulphotransferase activity synthesizing sulphated O-glycan core 1,3-sulphate-Gal beta 1-3GalNAc alpha-R.* Glycobiology, 1995. **5**(7): p. 689-97.
113. Chen, G.Y., N. Kurosawa, and T. Muramatsu, *A novel variant form of murine beta-1, 6-N-acetylglucosaminyltransferase forming branches in poly-N-acetyllactosamines.* Glycobiology, 2000. **10**(10): p. 1001-11.
114. Yeh, J.C., E. Ong, and M. Fukuda, *Molecular cloning and expression of a novel beta-1,6-N-acetylglucosaminyltransferase that forms core 2, core 4, and I branches.* Journal of Biological Chemistry, 1999. **274**(5): p. 3215-3221.
115. Schwientek, T., et al., *Control of O-glycan branch formation. Molecular cloning of human cDNA encoding a novel beta1,6-N-acetylglucosaminyltransferase forming core 2 and core 4.* J Biol Chem, 1999. **274**(8): p. 4504-12.
116. Brockhausen, I., et al., *Pathways of mucin O-glycosylation in normal and malignant rat colonic epithelial cells reveal a mechanism for cancer-associated Sialyl-Tn antigen expression.* Biol Chem, 2001. **382**(2): p. 219-32.

117. Sasaki, K., et al., *Expression cloning of cDNA encoding a human beta-1,3-N-acetylglucosaminyltransferase that is essential for poly-N-acetyllactosamine synthesis.* Proc Natl Acad Sci U S A, 1997. **94**(26): p. 14294-9.
118. Shiraishi, N., et al., *Identification and characterization of three novel beta 1,3-N-acetylglucosaminyltransferases structurally related to the beta 1,3-galactosyltransferase family.* J Biol Chem, 2001. **276**(5): p. 3498-507.
119. Brockhausen, I., et al., *Mucin synthesis. III. UDP-GlcNAc:Gal beta 1-3(GlcNAc beta 1-6)GalNAc-R (GlcNAc to Gal) beta 3-N-acetylglucosaminyltransferase, an enzyme in porcine gastric mucosa involved in the elongation of mucin-type oligosaccharides.* Can J Biochem Cell Biol, 1983. **61**(12): p. 1322-33.
120. Kono, M., et al., *Mouse beta-galactoside alpha 2,3-sialyltransferases: comparison of in vitro substrate specificities and tissue specific expression.* Glycobiology, 1997. **7**(4): p. 469-79.
121. Kitagawa, H. and J.C. Paulson, *Cloning of a Novel Alpha-2,3-Sialyltransferase That Sialylates Glycoprotein and Glycolipid Carbohydrate Groups.* Journal of Biological Chemistry, 1994. **269**(2): p. 1394-1401.
122. Okajima, T., et al., *Molecular cloning of a novel alpha2,3-sialyltransferase (ST3Gal VI) that sialylates type II lactosamine structures on glycoproteins and glycolipids.* J Biol Chem, 1999. **274**(17): p. 11479-86.
123. Weinstein, J., U. de Souza-e-Silva, and J.C. Paulson, *Sialylation of glycoprotein oligosaccharides N-linked to asparagine. Enzymatic characterization of a Gal beta 1 to 3(4)GlcNAc alpha 2 to 3 sialyltransferase and a Gal beta 1 to 4GlcNAc alpha 2 to 6 sialyltransferase from rat liver.* J Biol Chem, 1982. **257**(22): p. 13845-53.
124. Kurosawa, N., et al., *Cloning and expression of Gal beta 1,3GalNAc-specific GalNAc alpha 2,6-sialyltransferase.* J Biol Chem, 1994. **269**(29): p. 19048-53.
125. Samyn-Petit, B., et al., *Molecular cloning and functional expression of human ST6GalNAc II. Molecular expression in various human cultured cells.* Biochimica Et Biophysica Acta-General Subjects, 2000. **1474**(2): p. 201-211.
126. Sjoberg, E.R., et al., *Molecular cloning of a developmentally regulated N-acetylgalactosamine alpha2,6-sialyltransferase specific for sialylated glycoconjugates.* J Biol Chem, 1996. **271**(13): p. 7450-9.
127. Tsuchida, A., et al., *Molecular cloning and expression of human ST6GalNAc III: restricted tissue distribution and substrate specificity.* J Biochem, 2005. **138**(3): p. 237-43.
128. Larsen, R.D., et al., *Molecular cloning, sequence, and expression of a human GDP-L-fucose:beta-D-galactoside 2-alpha-L-fucosyltransferase cDNA that can form the H blood group antigen.* Proceedings of the National Academy of Sciences, 1990. **87**(17): p. 6674-6678.
129. Barreaud, J.-P., et al., *Three bovine α2-fucosyltransferase genes encode enzymes that preferentially transfer fucose on Galβ1–3GalNAc acceptor substrates.* Glycobiology, 2000. **10**(6): p. 611-621.
130. Devries, T., et al., *Acceptor Specificity of Different Length Constructs of Human Recombinant Alpha-1,3/4-Fucosyl-Transferases - Replacement of the Stem Region and the Transmembrane Domain of Fucosyl-Transferase-V by Protein-a Results in an Enzyme with Gdp-Fucose Hydrolyzing Activity.* Journal of Biological Chemistry, 1995. **270**(15): p. 8712-8722.

131. Niemela, R., et al., *Complementary acceptor and site specificities of Fuc-TIV and Fuc-TVII allow effective biosynthesis of sialyl-TriLex and related polylactosamines present on glycoprotein counterreceptors of selectins.* J Biol Chem, 1998. **273**(7): p. 4021-6.
132. Turunen, J.P., et al., *De novo expression of endothelial sialyl Lewis(a) and sialyl Lewis(x) during cardiac transplant rejection: superior capacity of a tetravalent sialyl Lewis(x) oligosaccharide in inhibiting L-selectin-dependent lymphocyte adhesion.* J Exp Med, 1995. **182**(4): p. 1133-41.
133. Mulquiney, P.J. and P.W. Kuchel, *Model of 2,3-bisphosphoglycerate metabolism in the human erythrocyte based on detailed enzyme kinetic equations: equations and parameter refinement.* Biochem J, 1999. **342 Pt 3**: p. 581-96.
134. Fornaini, G., et al., *Regulatory properties of human erythrocyte hexokinase during cell ageing.* Arch Biochem Biophys, 1985. **239**(2): p. 352-8.
135. Gerber, G., et al., *Hexokinase of human erythrocytes. Purification, kinetic model and its application to the conditions in the cell.* Eur J Biochem, 1974. **45**(1): p. 39-52.
136. Magnani, M., et al., *Action of oxidized and reduced glutathione on rabbit red blood cell hexokinase.* Biochim Biophys Acta, 1980. **615**(1): p. 113-20.
137. Rijksen, G., et al., *Separation and characterization of hexokinase I subtypes from human erythrocytes.* Biochim Biophys Acta, 1981. **659**(2): p. 292-301.
138. Rijksen, G. and G.E. Staal, *Regulation of human erythrocyte hexokinase. The influence of glycolytic intermediates and inorganic phosphate.* Biochim Biophys Acta, 1977. **485**(1): p. 75-86.
139. Grossbard, L. and R.T. Schimke, *Multiple Hexokinases of Rat Tissues - Purification and Comparison of Soluble Forms.* Journal of Biological Chemistry, 1966. **241**(15): p. 3546-3560.
140. Gracy, R.W. and B.E. Tilley, *Phosphoglucose isomerase of human erythrocytes and cardiac tissue.* Methods Enzymol, 1975. **41**: p. 392-400.
141. Kahana, S.E., et al., *The kinetics of phosphoglucoisomerase.* J Biol Chem, 1960. **235**: p. 2178-84.
142. Tilley, B.E., R.W. Gracy, and S.G. Welch, *A point mutation increasing the stability of human phosphoglucose isomerase.* J Biol Chem, 1974. **249**(14): p. 4751-9.
143. Dunaway, G.A., et al., *Analysis of the phosphofructokinase subunits and isoenzymes in human tissues.* Biochem J, 1988. **251**(3): p. 677-83.
144. Hanson, R.L., F.B. Rudolph, and H.A. Lardy, *Rabbit muscle phosphofructokinase. The kinetic mechanism of action and the equilibrium constant.* J Biol Chem, 1973. **248**(22): p. 7852-9.
145. Merry, S. and H.G. Britton, *The mechanism of rabbit muscle phosphofructokinase at pH8.* Biochem J, 1985. **226**(1): p. 13-28.
146. Otto, M., et al., *A mathematical model for the influence of anionic effectors on the phosphofructokinase from rat erythrocytes.* Eur J Biochem, 1977. **74**(2): p. 413-20.
147. Otto, M., et al., *A mathematical model for the influence of fructose 6-phosphate, ATP, potassium, ammonium and magnesium on the phosphofructokinase from rat erythrocytes.* Eur J Biochem, 1974. **49**(1): p. 169-78.

148. Vora, S., R. Oskam, and G.E. Staal, *Isoenzymes of phosphofructokinase in the rat. Demonstration of the three non-identical subunits by biochemical, immunochemical and kinetic studies.* Biochem J, 1985. **229**(2): p. 333-41.
149. Foe, L.G. and R.G. Kemp, *Isolation and characterization of phosphofructokinase C from rabbit brain.* J Biol Chem, 1985. **260**(2): p. 726-30.
150. Kitajima, S., R. Sakakibara, and K. Uyeda, *Kinetic studies of fructose 6-phosphate,2-kinase and fructose 2,6-bisphosphatase.* J Biol Chem, 1984. **259**(11): p. 6896-903.
151. Kretschmer, M., W. Schellenberger, and E. Hofmann, *Quasi-stationary concentrations of fructose-2,6-bisphosphate in the phosphofructokinase-2/fructose-2,6-bisphosphatase cycle.* Biochem Biophys Res Commun, 1985. **131**(2): p. 899-904.
152. Okar, D.A., et al., *PFK-2/FBPase-2: maker and breaker of the essential biofactor fructose-2,6-bisphosphate.* Trends Biochem Sci, 2001. **26**(1): p. 30-5.
153. Beutler, E., *2,3-diphosphoglycerate affects enzymes of glucose metabolism in red blood cells.* Nat New Biol, 1971. **232**(27): p. 20-1.
154. Beutler, E., *Red Cell Metabolism: A Manual of Biochemical Methods*. 3rd ed. 1984, New York: Grune and Stratton.
155. Mehler, A.H., *Kinetic properties of native and carboxy-peptidase-altered rabbit muscle aldolase.* J Biol Chem, 1963. **238**: p. 100-4.
156. Mehler, A.H. and B. Bloom, *Interaction between rabbit muscle aldolase and dihydroxyacetone phosphate.* J Biol Chem, 1963. **238**: p. 105-7.
157. Penhoet, E.E., M. Kochman, and W.J. Rutter, *Ioslation of fructose diphosphate aldolases A, B, and C.* Biochemistry, 1969. **8**(11): p. 4391-5.
158. Penhoet, E.E., M. Kochman, and W.J. Rutter, *Molecular and catalytic properties of aldolase C.* Biochemistry, 1969. **8**(11): p. 4396-402.
159. Rose, I.A., E.L. O'Connell, and A.H. Mehler, *Mechanism of the Aldolase Reaction.* J Biol Chem, 1965. **240**: p. 1758-65.
160. Srivastava, S.K. and E. Beutler, *The effect of normal red cell constituents on the activities of red cell enzymes.* Arch Biochem Biophys, 1972. **148**(1): p. 249-55.
161. Strapazon, E. and T.L. Steck, *Interaction of the aldolase and the membrane of human erythrocytes.* Biochemistry, 1977. **16**(13): p. 2966-71.
162. Yeltman, D.R. and B.G. Harris, *Purification and characterization of aldolase from human erythrocytes.* Biochim Biophys Acta, 1977. **484**(1): p. 188-98.
163. Gracy, R.W., *Triosephosphate isomerase from human erythrocytes.* Methods Enzymol, 1975. **41**: p. 442-7.
164. Sawyer, T.H., B.E. Tilley, and R.W. Gracy, *Studies on human triosephosphate isomerase. II. Nature of the electrophoretic multiplicity in erythrocytes.* J Biol Chem, 1972. **247**(20): p. 6499-505.
165. Schneider, A.S., et al., *Hereditary Hemolytic Anemia with Triosephosphate Isomerase Deficiency.* N Engl J Med, 1965. **272**: p. 229-35.
166. Cori, C.F., S.F. Velick, and G.T. Cori, *The combination of diphosphopyridine nucleotide with glyceraldehyde phosphate dehydrogenase.* Biochim Biophys Acta, 1950. **4**(1-3): p. 160-9.

167. Furfine, C.S. and S.F. Velick, *The Acyl-Enzyme Intermediate and the Kinetic Mechanism of the Glyceraldehyde 3-Phosphate Dehydrogenase Reaction.* J Biol Chem, 1965. **240**: p. 844-55.
168. Heinz, F. and B. Freimuller, *Glyceraldehyde-3-phosphate dehydrogenase from human tissues.* Methods Enzymol, 1982. **89 Pt D**: p. 301-5.
169. Wang, C.S. and P. Alaupovic, *Glyceraldehyde-3-phosphate dehydrogenase from human erythrocyte membranes. Kinetic mechanism and competitive substrate inhibition by glyceraldehyde 3-phosphate.* Arch Biochem Biophys, 1980. **205**(1): p. 136-45.
170. Ali, M. and Y.S. Brownstone, *A study of phosphoglycerate kinase in human erythrocytes. II. Kinetic properties.* Biochim Biophys Acta, 1976. **445**(1): p. 89-103.
171. Krietsch, W.K. and T. Bucher, *3-phosphoglycerate kinase from rabbit sceletal muscle and yeast.* Eur J Biochem, 1970. **17**(3): p. 568-80.
172. Lee, C.S. and W.J. O'Sullivan, *Properties and mechanism of human erythrocyte phosphoglycerate kinase.* J Biol Chem, 1975. **250**(4): p. 1275-81.
173. Yoshida, A. and S. Watanabe, *Human phosphoglycerate kinase. I. Crystallization and characterization of normal enzyme.* J Biol Chem, 1972. **247**(2): p. 440-5.
174. Mulquiney, P.J., W.A. Bubb, and P.W. Kuchel, *Model of 2,3-bisphosphoglycerate metabolism in the human erythrocyte based on detailed enzyme kinetic equations: in vivo kinetic characterization of 2,3-bisphosphoglycerate synthase/phosphatase using 13C and 31P NMR.* Biochem J, 1999. **342 Pt 3**: p. 567-80.
175. Mulquiney, P.J. and P.W. Kuchel, *Model of 2,3-bisphosphoglycerate metabolism in the human erythrocyte based on detailed enzyme kinetic equations: computer simulation and metabolic control analysis.* Biochem J, 1999. **342 Pt 3**: p. 597-604.
176. Garfinkel, L. and D. Garfinkel, *Magnesium regulation of the glycolytic pathway and the enzymes involved.* Magnesium, 1985. **4**(2-3): p. 60-72.
177. Rider, C.C. and C.B. Taylor, *Enolase isoenzymes in rat tissues. Electrophoretic, chromatographic, immunological and kinetic properties.* Biochim Biophys Acta, 1974. **365**(1): p. 285-300.
178. Wold, F. and C.E. Ballou, *Studies on the enzyme enolase. I. Equilibrium studies.* J Biol Chem, 1957. **227**(1): p. 301-12.
179. Albe, K.R., M.H. Butler, and B.E. Wright, *Cellular concentrations of enzymes and their substrates.* J Theor Biol, 1990. **143**(2): p. 163-95.
180. Holzhutter, H.G., G. Jacobasch, and A. Bisdorff, *Mathematical modelling of metabolic pathways affected by an enzyme deficiency. A mathematical model of glycolysis in normal and pyruvate-kinase-deficient red blood cells.* Eur J Biochem, 1985. **149**(1): p. 101-11.
181. Kahn, A. and J. Marie, *Pyruvate kinases from human erythrocytes and liver.* Methods Enzymol, 1982. **90 Pt E**: p. 131-40.
182. Koster, J.F., et al., *The influence of glucose I,6-diphosphate on the enzymatic activity of pyruvate kinase.* Biochim Biophys Acta, 1972. **258**(3): p. 763-8.
183. Mc, Q.J. and M.F. Utter, *Equilibrium and kinetic studies of the pyruvic kinase reaction.* J Biol Chem, 1959. **234**(8): p. 2151-7.

184. Rozengurt, E., L. Jimenez de Asua, and H. Carminatti, *Some kinetic properties of liver pyruvate kinase (type L). II. Effect of pH on its allosteric behavior.* J Biol Chem, 1969. **244**(12): p. 3142-7.
185. Yamada, K. and T. Noguchi, *Nutrient and hormonal regulation of pyruvate kinase gene expression.* Biochemical Journal, 1999. **337**: p. 1-11.
186. Borgmann, U., T.W. Moon, and K.J. Laidler, *Molecular kinetics of beef heart lactate dehydrogenase.* Biochemistry, 1974. **13**(25): p. 5152-8.
187. Wang, C.S., *Inhibition of human erythrocyte lactate dehydrogenase by high concentrations of pyruvate. Evidence for the competitive substrate inhibition.* Eur J Biochem, 1977. **78**(2): p. 569-74.
188. Zewe, V. and H.J. Fromm, *Kinetic Studies of Rabbit Muscle Lactate Dehydrogenase. Ii. Mechanism of the Reaction.* Biochemistry, 1965. **4**: p. 782-92.
189. Zewe, V. and H.J. Fromm, *Kinetic Studies of Rabbit Muscle Lactate Dehydrogenase .2. Mechanism of Reaction.* Biochemistry, 1965. **4**(4): p. 782-&.
190. Stambaugh, R. and D. Post, *Substrate and Product Inhibition of Rabbit Muscle Lactic Dehydrogenase Heart (H4) and Muscle (M4) Isozymes.* Journal of Biological Chemistry, 1966. **241**(7): p. 1462-+.
191. Borgmann, U., T.W. Moon, and K.J. Laidler, *Molecular Kinetics of Beef Heart Lactate-Dehydrogenase.* Biochemistry, 1974. **13**(25): p. 5152-5158.
192. Kanji, M.I., M.L. Toews, and W.R. Carper, *A kinetic study of glucose-6-phosphate dehydrogenase.* J Biol Chem, 1976. **251**(8): p. 2258-62.
193. Thorburn, D.R. and P.W. Kuchel, *Regulation of the human-erythrocyte hexose-monophosphate shunt under conditions of oxidative stress. A study using NMR spectroscopy, a kinetic isotope effect, a reconstituted system and computer simulation.* Eur J Biochem, 1985. **150**(2): p. 371-86.
194. Kirkman, H.N., W.G. Wilson, and E.H. Clemons, *Regulation of glucose-6-phosphate dehydrogenase. I. Intact red cells.* J Lab Clin Med, 1980. **95**(6): p. 877-87.
195. Glaser, L. and D.H. Brown, *Purification and properties of d-glucose-6-phosphate dehydrogenase.* J Biol Chem, 1955. **216**(1): p. 67-79.
196. Villet, R.H. and K. Dalziel, *Studies of 6-phosphogluconate dehydrogenase from sheep liver. 2. Kinetics of the oxidative-decarboxylation reaction, coenzyme binding and analyses for metals.* Eur J Biochem, 1972. **27**(2): p. 251-8.
197. Pearse, B.M. and M.A. Rosemeyer, *Human 6-phosphogluconate dehydrogenase. Purification of the erythrocyte enzyme and the influence of ions and NADPH on its activity.* Eur J Biochem, 1974. **42**(1): p. 213-23.
198. Villet, R.H. and K. Dalziel, *The nature of the carbon dioxide substrate and equilibrium constant of the 6-phosphogluconate dehydrogenase reaction.* Biochem J, 1969. **115**(4): p. 633-8.
199. McIntyre, L.M., et al., *Comparison of computer simulations of the F-type and L-type non-oxidative hexose monophosphate shunts with 31P-NMR experimental data from human erythrocytes.* Eur J Biochem, 1989. **180**(2): p. 399-420.
200. Casazza, J.P. and R.L. Veech, *The interdependence of glycolytic and pentose cycle intermediates in ad libitum fed rats.* J Biol Chem, 1986. **261**(2): p. 690-8.
201. Wood, T., *Purification and properties of D-ribulose-5-phosphate 3-epimerase from calf liver.* Biochim Biophys Acta, 1979. **570**(2): p. 352-62.

202. Horecker, B.L. and J. Hurwitz, *The purification of phosphoketopentoepimerase from Lactobacillus pentosus and the preparation of xylulose 5-phosphate.* J Biol Chem, 1956. **223**(2): p. 993-1008.
203. Urivetzky, M. and K.K. Tsuboi, *Enzymes of the Human Erythrocyte. V. Pentose Phosphate Isomerase, Purification and Properties.* Arch Biochem Biophys, 1963. **103**: p. 1-8.
204. Kiely, M.E., A.L. Stuart, and T. Wood, *Partial purification and kinetic properties of ribose-5-phosphate ketol-isomerase and ribulose-5-phosphate 3-epimerase from various sources.* Biochim Biophys Acta, 1973. **293**(2): p. 534-41.
205. Joshi, A. and B.O. Palsson, *Metabolic dynamics in the human red cell. Part III--Metabolic reaction rates.* J Theor Biol, 1990. **142**(1): p. 41-68.
206. Warnock, L.G. and C.R. Prudhomme, *The isolation and preliminary characterization of apotransketolase from human erythrocytes.* Biochem Biophys Res Commun, 1982. **106**(3): p. 719-23.
207. Venkataraman, R. and E. Racker, *Mechanism of action of transaldolase. II. The substrate-enzyme intermediate.* J Biol Chem, 1961. **236**: p. 1883-6.
208. Horecker, B.L. and P.Z. Smyrniotis, *Purification and properties of yeast transaldolase.* J Biol Chem, 1955. **212**(2): p. 811-25.
209. Kuhn, E. and K. Brand, *Purification and properties of transaldolase from bovine mammary gland.* Biochemistry, 1972. **11**(10): p. 1767-72.
210. Datta, A.G. and E. Racker, *Mechanism of action of transketolase. I. Properties of the crystalline yeast enzyme.* J Biol Chem, 1961. **236**: p. 617-23.
211. Mannervik, B., *A branching reaction mechanism of glutathione reductase.* Biochem Biophys Res Commun, 1973. **53**(4): p. 1151-8.
212. Worthington, D.J. and M.A. Rosemeyer, *Glutathione reductase from human erythrocytes. Catalytic properties and aggregation.* Eur J Biochem, 1976. **67**(1): p. 231-8.
213. Scott, E.M., I.W. Duncan, and V. Ekstrand, *Purification and Properties of Glutathione Reductase of Human Erythrocytes.* J Biol Chem, 1963. **238**: p. 3928-33.
214. Wu, F., et al., *Computer modeling of mitochondrial tricarboxylic acid cycle, oxidative phosphorylation, metabolite transport, and electrophysiology.* J Biol Chem, 2007. **282**(34): p. 24525-37.
215. Kohn, M.C., M.J. Achs, and D. Garfinkel, *Computer simulation of metabolism in pyruvate-perfused rat heart. III. Pyruvate dehydrogenase.* Am J Physiol, 1979. **237**(3): p. R167-73.
216. Tsai, C.S., M.W. Burgett, and L.J. Reed, *Alpha-keto acid dehydrogenase complexes. XX. A kinetic study of the pyruvate dehydrogenase complex from bovine kidney.* J Biol Chem, 1973. **248**(24): p. 8348-52.
217. Kohn, M.C., M.J. Achs, and D. Garfinkel, *Computer simulation of metabolism in pyruvate-perfused rat heart. II. Krebs cycle.* Am J Physiol, 1979. **237**(3): p. R159-66.
218. Kohn, M.C. and D. Garfinkel, *Computer simulation of metabolism in palmitate-perfused rat heart. II. Behavior of complete model.* Ann Biomed Eng, 1983. **11**(6): p. 511-31.

219. Shepherd, D. and P.B. Garland, *The kinetic properties of citrate synthase from rat liver mitochondria.* Biochem J, 1969. **114**(3): p. 597-610.
220. Smith, C.M. and J.R. Williamson, *Inhibition of citrate synthase by succinyl-CoA and other metabolites.* FEBS Lett, 1971. **18**(1): p. 35-38.
221. Thomson, J.F., et al., *Isotope and solvent effects of deuterium on aconitase.* Arch Biochem Biophys, 1966. **117**(1): p. 65-74.
222. Denton, R.M., D.A. Richards, and J.G. Chin, *Calcium ions and the regulation of NAD+-linked isocitrate dehydrogenase from the mitochondria of rat heart and other tissues.* Biochem J, 1978. **176**(3): p. 899-906.
223. Plaut, G.W., et al., *Cosubstrate and allosteric modifier activities of structural analogues of NAD and ADP for NAD-specific isocitrate dehydrogenase from bovine heart.* Biochemistry, 1979. **18**(15): p. 3430-8.
224. Williamson, J.R., et al., *Mitochondrial-cytosolic interactions in cardiac tissue: role of the malate-aspartate cycle in the removal of glycolytic NADH from the cytosol.* Symp Soc Exp Biol, 1973. **27**: p. 241-81.
225. Smith, C.M., J. Bryla, and J.R. Williamson, *Regulation of mitochondrial alpha-ketoglutarate metabolism by product inhibition at alpha-ketoglutarate dehydrogenase.* J Biol Chem, 1974. **249**(5): p. 1497-505.
226. Cha, S. and R.E. Parks, Jr., *Succinic Thiokinase. Ii. Kinetic Studies: Initial Velocity, Product Inhibition, and Effect of Arsenate.* J Biol Chem, 1964. **239**: p. 1968-77.
227. Barman, T.E., *Enzyme Handbook.* 1969, New York: Springer-Verlag.
228. Gutman, M., *Regulation of mitochondrial succinate dehydrogenase by substrate type activators.* Biochemistry, 1977. **16**(14): p. 3067-72.
229. Hatefi, Y. and D.L. Stiggall, *Metal-containing flavoprotein dehydrogenases*, in *The Enzymes*, P.D. Boyer, Editor. 1976, Academic Press: New York. p. 175-297.
230. Brant, D.A., L.B. Barnett, and R.A. Alberty, *The temperature dependence of the steady state kinetic parameters of the fumarase reaction.* J. Am. Chem. Soc., 1963. **85**: p. 2204-2209.
231. Penner, P.E. and L.H. Cohen, *Effects of adenosine triphosphate and magnesium ions on the fumarase reaction.* J Biol Chem, 1969. **244**(3): p. 1070-5.
232. Kimball, D.F., et al., *Malate dehydrogenase. Kinetic studies with meso-tartrate and 2-keto-3-hydroxysuccinate, comparison of the mitochondrial and supernatant pig heart enzymes.* Arch Biochem Biophys, 1979. **195**(1): p. 66-73.
233. Oza, N.B. and J.D. Shore, *The effects of adenine nucleotides on NADH binding to mitochondrial malate dehydrogenase.* Arch Biochem Biophys, 1973. **154**(1): p. 360-5.
234. Henson, C.P. and W.W. Cleland, *Kinetic Studies of Glutamic Oxaloacetic Transaminase Isozymes.* Biochemistry, 1964. **3**: p. 338-45.
235. Crow, K.E., et al., *Rat liver cytosolic malate dehydrogenase: purification, kinetic properties, role in control of free cytosolic NADH concentration. Analysis of control of ethanol metabolism using computer simulation.* J Biol Chem, 1982. **257**(23): p. 14217-25.
236. Indiveri, C., et al., *Reaction mechanism of the reconstituted oxoglutarate carrier from bovine heart mitochondria.* Eur J Biochem, 1991. **198**(2): p. 339-47.

237. Dierks, T., E. Riemer, and R. Kramer, *Reaction mechanism of the reconstituted aspartate/glutamate carrier from bovine heart mitochondria.* Biochim Biophys Acta, 1988. **943**(2): p. 231-44.
238. Uldry, M. and B. Thorens, *The SLC2 family of facilitated hexose and polyol transporters.* Pflugers Arch, 2004. **447**(5): p. 480-9.
239. Uldry, M., et al., *GLUT2 is a high affinity glucosamine transporter.* Febs Letters, 2002. **524**(1-3): p. 199-203.
240. Williams, T.F., et al., *Stereospecific transport of glucose in the perfused rat liver.* Am J Physiol, 1968. **215**(5): p. 1200-9.
241. Colville, C.A., et al., *Kinetic analysis of the liver-type (GLUT2) and brain-type (GLUT3) glucose transporters in Xenopus oocytes: substrate specificities and effects of transport inhibitors.* Biochem J, 1993. **290 (Pt 3)**: p. 701-6.
242. Haser, W.G., R.A. Shapiro, and N.P. Curthoys, *Comparison of the phosphate-dependent glutaminase obtained from rat brain and kidney.* Biochem J, 1985. **229**(2): p. 399-408.
243. Rife, J.E. and W.W. Cleland, *Kinetic mechanism of glutamate dehydrogenase.* Biochemistry, 1980. **19**(11): p. 2321-8.
244. Frieden, C., *Glutamic dehydrogenase. III. The order of substrate addition in the enzymatic reaction.* J Biol Chem, 1959. **234**: p. 2891-6.
245. Houston, B. and H.G. Nimmo, *Effects of phosphorylation on the kinetic properties of rat liver ATP-citrate lyase.* Biochim Biophys Acta, 1985. **844**(2): p. 233-9.
246. Plowman, D.M. and W.W. Cleland, *Purification and kinetic studies of the citrate cleavage enzyme.* J Biol Chem, 1967. **242**(18): p. 4239-47.
247. Ranganathan, N.S., P.A. Srere, and T.C. Linn, *Comparison of phospho- and dephospho-ATP citrate lyase.* Arch Biochem Biophys, 1980. **204**(1): p. 52-8.
248. Houston, B. and H.G. Nimmo, *Purification and some kinetic properties of rat liver ATP citrate lyase.* Biochem J, 1984. **224**: p. 437-443.
249. Teller, J.K., L.A. Fahien, and J.W. Davis, *Kinetics and regulation of hepatoma mitochondrial NAD(P) malic enzyme.* J Biol Chem, 1992. **267**(15): p. 10423-32.
250. Hsu, R.Y., H.A. Lardy, and W.W. Cleland, *Pigeon liver malic enzyme. V. Kinetic studies.* J Biol Chem, 1967. **242**(22): p. 5315-22.
251. Bulos, B. and P. Handler, *Kinetics of Beef Heart Glutamic-Alanine Transaminase.* J Biol Chem, 1965. **240**: p. 3283-94.
252. Jitrapakdee, S., M.E. Walker, and J.C. Wallace, *Functional expression, purification, and characterization of recombinant human pyruvate carboxylase.* Biochem Biophys Res Commun, 1999. **266**(2): p. 512-7.
253. Halestrap, A.P. and D. Meredith, *The SLC16 gene family-from monocarboxylate transporters (MCTs) to aromatic amino acid transporters and beyond.* Pflugers Arch, 2004. **447**(5): p. 619-28.
254. Juel, C. and A.P. Halestrap, *Lactate transport in skeletal muscle - role and regulation of the monocarboxylate transporter.* J Physiol, 1999. **517 (Pt 3)**: p. 633-42.

8 APPENDIX

8.1 APPENDIX TABLES

Appendix Table 1. Fixed parameter values in the metabolic model

Reproduced from: Mulukutla, B.C., et al., *Multiplicity of Steady States in Glycolysis and Shift of Metabolic State in Cultured Mammalian Cells.* Plos One, 2015. **10**(3).

Parameter Symbol	Parameter Description	Value	Units
Ccadp	Cytosolic ADP concentration	0.54	mM
Cmadp	Mitochondrial ADP concentration	0.1	mM
Ccatp	Cytosolic ATP concentration	0.31	mM
Cmatp	Mitochondrial ATP concentration	0.1	mM
Ccamp	Cytosolic AMP concentration	0.03	mM
Cmamp	Mitochondrial AMP concentration	0.1	mM
Cmgtp	Mitochondrial GTP concentration	0.1	mM
Cmgdp	Mitochondrial GDP concentration	0.1	mM
pHm	Mitochondrial pH	8	
pHi	Intracellular pH	7.3	
Mg	Cytosolic magnesium concentration	0.7	mM
MgADP	Cytosolic MgADP concentration	0.46	mM
MgATP	Cytosolic MgATP concentration	2.69	mM
Ncd	Total cytosolic NAD concentration	0.32	mM
Ndp	Total cytosolic NADP concentration	0.065	mM
Ccpi	Cytosolic phosphate concentration	2.5	mM
Cmpi	Mitochondrial phosphate concentration	2.5	mM
Cc23p2g	Cytosolic 2,3-bisphosphoglycerate concentration	3.1	mM
Ccg16p	Cytosolic glucose 1,6-bisphosphate concentration	0.1	mM
Ccala	Cytosolic alanine concentration	1	mM
Cmcoq	Mitochondrial oxidized ubiquinol concentration	1.08	mM
Cmqh2	Mitochondrial reduced ubiquinol concentration	0.27	mM
Ccco2	Cytosolic CO_2 concentration	1.2	mM
Cmco2	Mitochondrial CO_2 concentration	21.4	mM
Cccoash	Cytosolic Coenzyme A concentration	0.02	mM

Ccaccoa	Cytosolic Acetyl-Coenzyme A concentration	0.001	mM
Cmcoash	Mitochondrial Coenzyme A concentration	0.04	mM
Cmnad	Mitochondrial NAD concentration	2.87	mM
Cmnadh	Mitochondrial NADH concentration	0.1	mM

Appendix Table 2. Changes in the steady state behavior of glycolysis flux at different stages of HLC differentiation

Each row represents one set of steady state simulations that consider the changes in the transcript levels of isoforms of a single glycolysis enzyme. The last row shows the resulting steady state behavior of glycolysis flux under changes in the isoform levels of GLUT, HK, PFK, PK, and LDH, altogether.

	Day 6 (Stage 1)	**Day 10 (Stage 2)**	**Day 14 (Stage 3)**	**Day 20 (Stage 4)**
GLUT	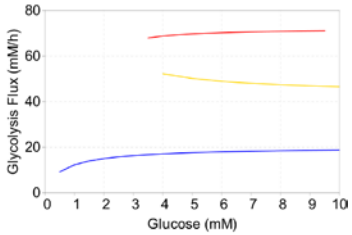	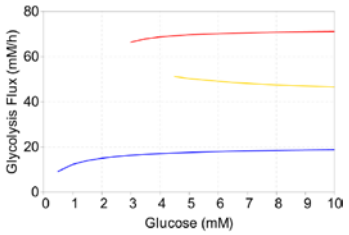	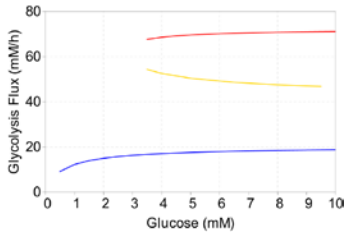	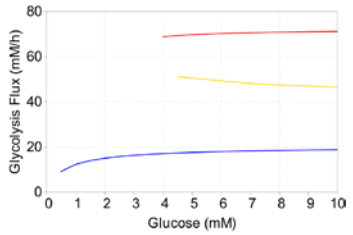
HK	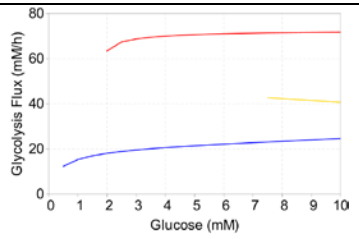	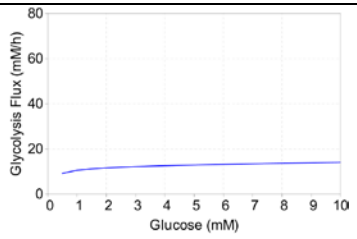	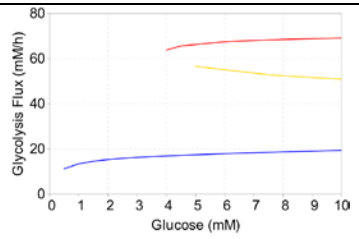	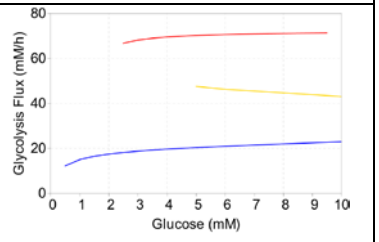

PFK	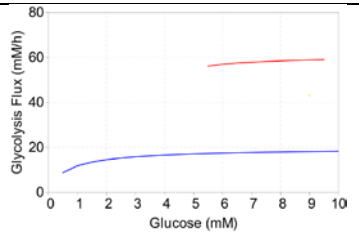	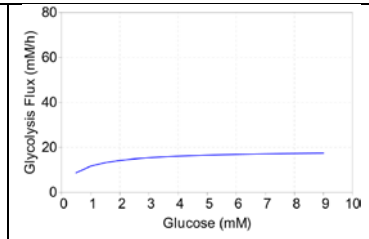	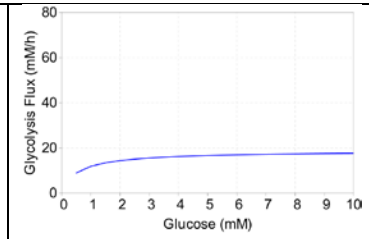	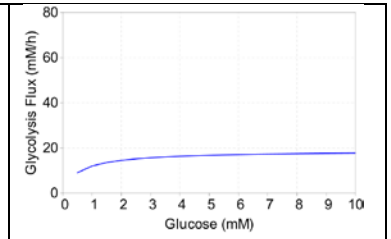
PK	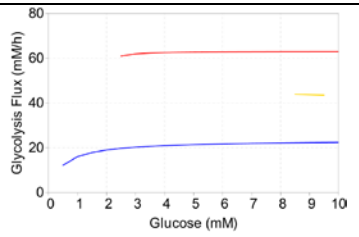	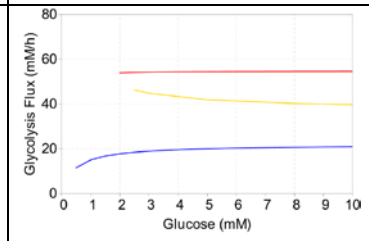	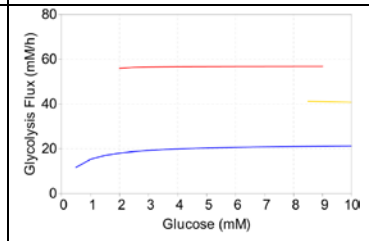	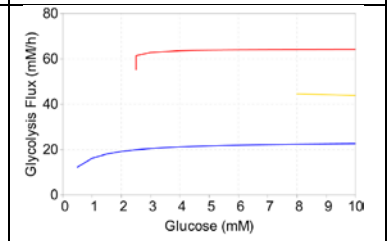
LDH	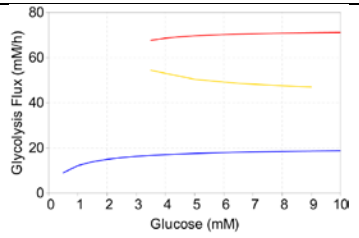	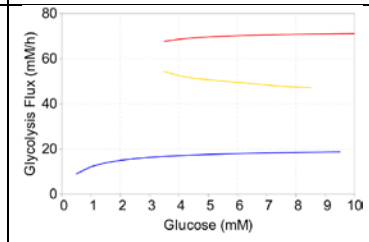	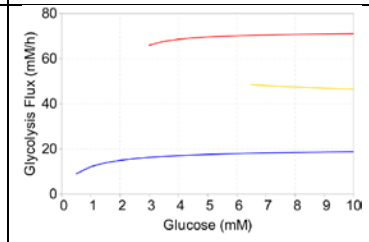	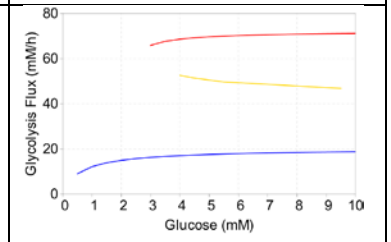
Combined	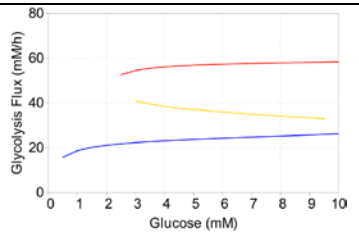	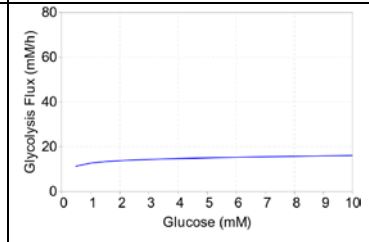	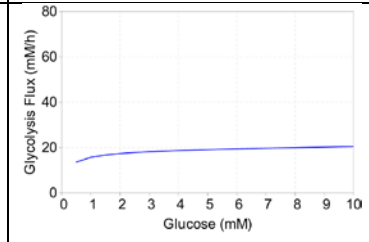	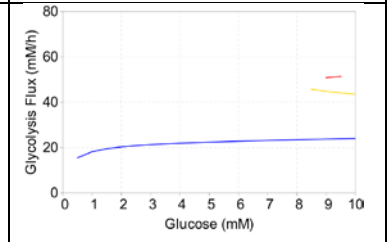

Appendix Table 3. Structural requirements for glycan substrates of all enzymes implemented in O-glycosylation network.

Enzyme (*Short Name*)	Gene symbol	Substrate → Product	Requirement/restriction implemented in the model
polypeptide *N*-acetylgalactosaminyltransferase (*ppGalNAcT*)	GALNTs	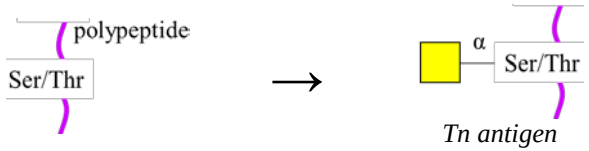	Requirement: No specific sequon is required although the presence of Pro near Ser/Thr seems to favor the initiation of mucin-type ***O***-glycosylation, [102]
N-acetyl-*β*-glucosaminyl-glycoprotein 4-*β*-N-acetylgalactosaminyltransferase 2 (*Cad β4-GalNAcT2*)	B4GALNT2	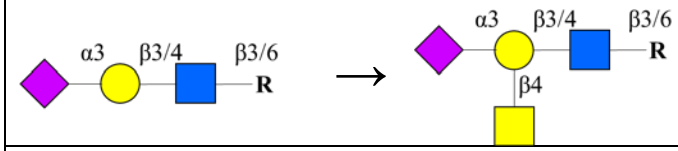 	Requirement: Gal residues of Neu5Acα2-3Gal (of type 1, type 2 and type 3 chains). Type 3 chains are less preferred than type 1 and 2 chains. [103] Restriction: Prior fucosylation of the Gal residue was reported to preclude this reaction.[104]
N-acetyl-*β*-glucosaminyl-glycoprotein 4-*β*-N-acetylgalactosaminyltransferase 3 and 4 (*β4-GalNAcT3,4*)	B4GALNT3, 4	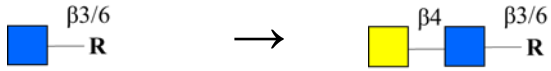	Requirement: Non-reducing terminal GlcNAcβ residue [105]
α-1,3-N-acetylgalactosaminytransferase	A3GALNT	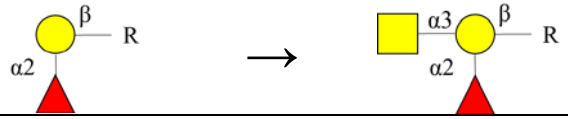	Requirement: prior α2-fucosylation of the target Gal residue [106].

Enzyme (*Short Name*)	**Gene symbol**	**Substrate → Product**	**Requirement/restriction implemented in the model**
N-acetylgalactosaminide *β*-1,3-galactosyltransferase (*C1β3-GalT-I*)	C1GALT1	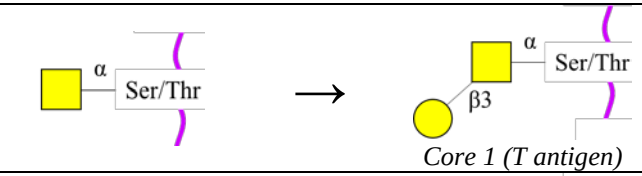 *Core 1 (T antigen)*	Requirement: Free 3- and 4-hydroxyls of GalNAc [107].
		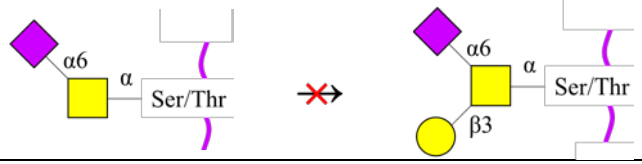	Restriction: Sialyl Tn antigen is not a substrate [102]
β-N-acetylglucosaminyl-glycopeptide *β*-1,4-galactosyltransferase (*β4-GalT*)	B4GALT1, 2, 3, 4	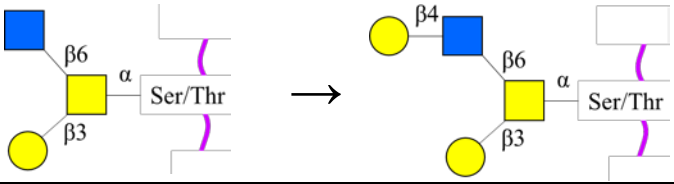	Requirement: Free 4-hydroxyl of GlcNAc [108].
		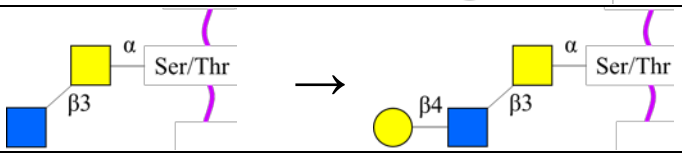	Note: β4GalT4 is the most efficient enzyme for galactosylation of core 2. β4GalT1 is the most efficient enzyme for galactosylation of core 3. Both β4GalT1 and β4GalT4 are efficient in forming type 2 poly-*N*-acetyllactosamine structures (Gal*β*1-4GlcNAc-)$_n$ of core 2 and 3 [109]. β4GalT1 is the most efficient enzyme for galactosylation of GlcNAcβ1-6 of I antigen [110]
		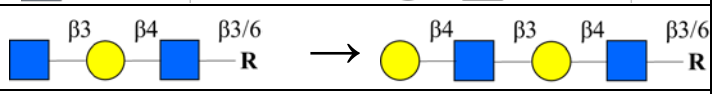	
		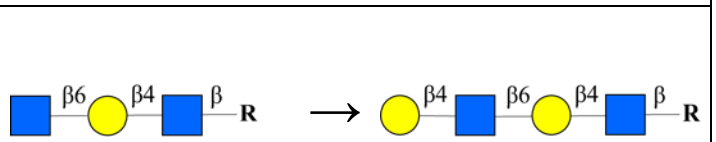	

Enzyme (*Short Name*)	Gene symbol	Substrate → Product	Requirement/restriction implemented in the model
			Restriction: Prior addition of Gal or GalNAc to the GlcNAc residue via β1,3-linkage precludes this reaction.[1]
β-N-acetylglucosaminyl-glycopeptide *β*-1,3-galactosyltransferase (*β3-GalT*)	B3GALT5	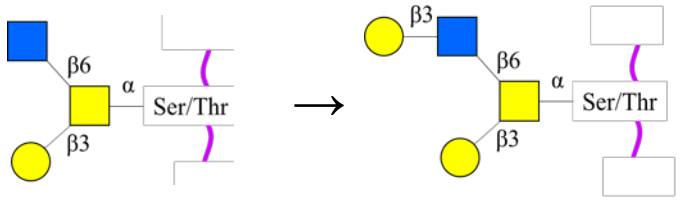	Requirement: Free 3-hydroxyl of GlcNAc; Substrates include core 2 and 3 O-glycans [92]. Note: Because core 3 structures are not formed in the network, the model only considers core 2 glycans as substrates of B3GALT5.
			Restriction: Prior addition of Gal or GalNAc to the GlcNAc residue via β1,4-linkage precludes this reaction.[2][3]
α-1,3-galactosyltransferase	A3GALT	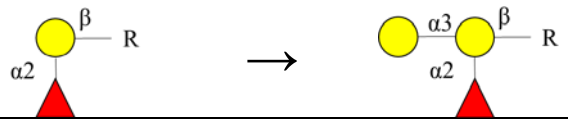	Requirement: prior α2-fucosylation of the target Gal residue [106].

[1] Assumed to simplify the model.
[2] Assumed to simplify the model.
[3] Assumed to simplify the model.

Enzyme (*Short Name*)	Gene symbol	Substrate → Product	Requirement/restriction implemented in the model
β-1,3-galactosyl-***O***-glycosyl-glycoprotein *β*-1,6-*N* – acetylglucosaminyltransferase (*C2β6-GnT*)	GCNT1, 3, 4	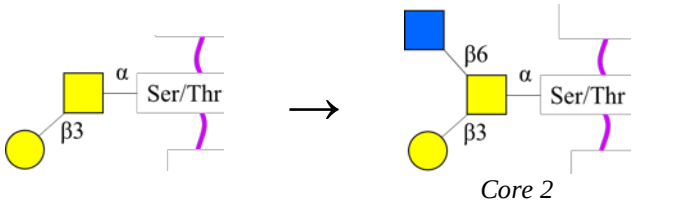 *Core 2*	Requirement: Free 4- and 6-hydroxyls of Gal and GalNAc [111]; free 2-acetamido group of GalNAc [102]. The latter requirement is not necessary for the current model.
		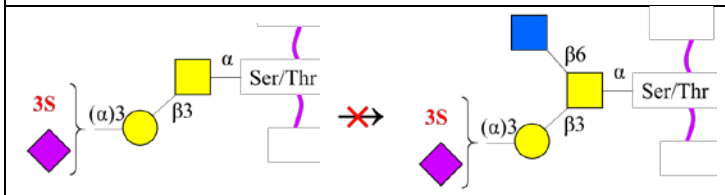	Restriction: Gal of core 1 must not be ***O***-3-sulfated [112] or connected with Neu5Ac via α2-3 linkage [102]
N-acetyllactosaminide *β*-1,6-N-acetylglucosaminyl-transferase	GCNT2	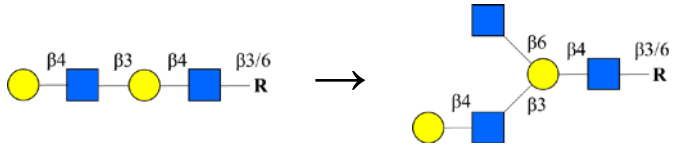	Requirement: Non-terminal Galβ1-4 residue on poly-LacNAc chain (mainly type 2). Sub-terminal Galβ1-4 residue is most preferred substrate [113].
β-1,3-galactosyl-*O*-glycosyl-glycoprotein *β*-1,6-N-acetylglucosaminyltransferase 3	GCNT3	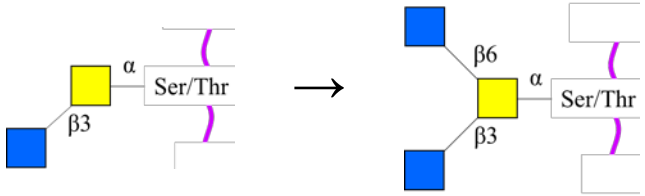	Requirement: Free 4- and 6-hydroxyls of GalNAc and the 6-hydroxyl of Gal [102]. Core 1, core 3, and GlcNAcb1-3Gal- are substrates for the synthesis of

Enzyme (*Short Name*)	Gene symbol	Substrate → Product	Requirement/restriction implemented in the model
		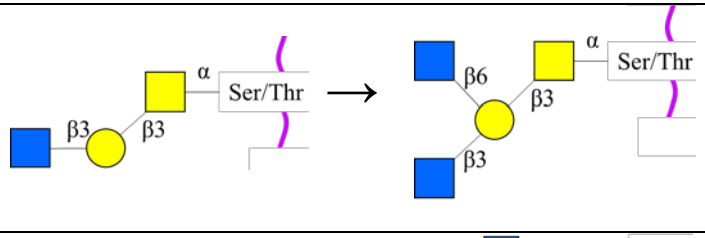 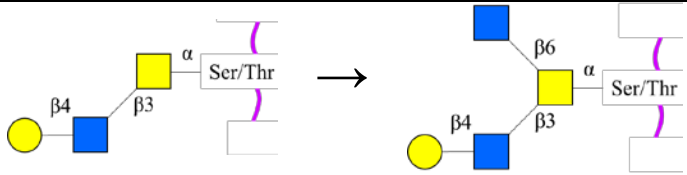	core 2, core 4, and I antigen, respectively [114, 115] Restriction: Extended core 3 structures (Galβ1-3/4GlcNacβ1-3GalNAcαSer/Thr) are not substrate for core 4 synthesis [116]. In order to simplify the network, it was assumed that only unmodified core 3 structure is the substrate.
N-acetyllactosaminide *β*-1,3-N-acetylglucosaminyltransferase (*β3-GnT*)	B3GNT1, 2, 3, 4	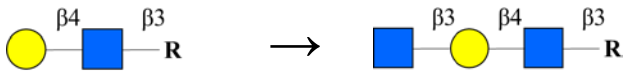	Requirement: Free 3-hydroxyl of Gal on (poly)-*N*-acetyllactosamine chains [117, 118]
		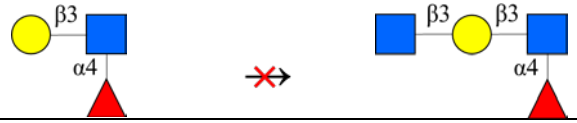	Restriction: type 1 and type 2 chains with the inner GlcNAc being α1,4- and α1,3-fucosylated are not substrates [118].
		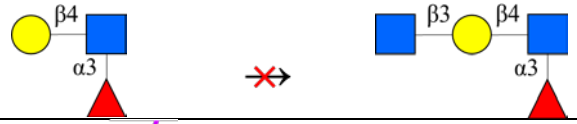	
N-acetyllactosaminide *β*-1,3-N-acetylglucosaminyltran	B3GNT3	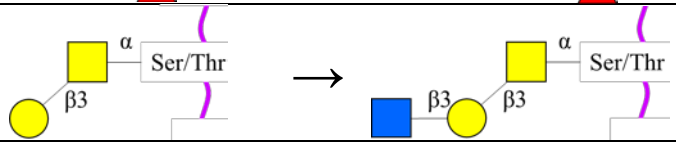	Requirement: Free 3-hydroxyl of Gal; Substrates include core 1 and core 2 O-glycans [119]

Enzyme (*Short Name*)	Gene symbol	Substrate → Product	Requirement/restriction implemented in the model
sferase 3 (*core 1 extension*)		*Extended core 1* 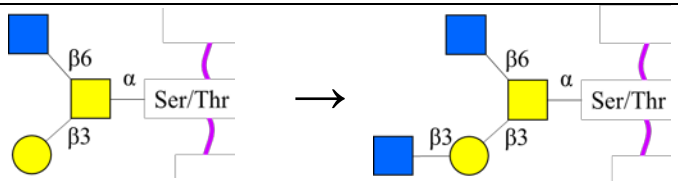	
		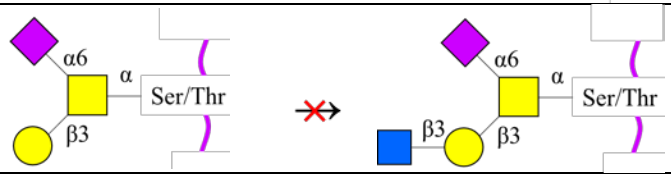	Restriction: α6-sialyl core 1 is not a substrate.
N-acetyllactosaminide *β*-1,3-N-acetylglucosaminyltransferase 6 (*core 3 synthase*)	B3GNT6	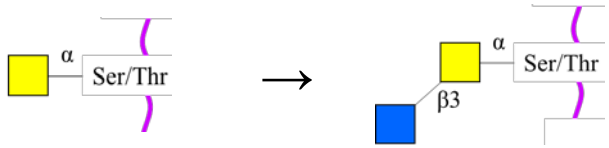	
N-acetyl-*β*-glucosaminyl-glycoprotein 4-*β*-N-acetylgalactosaminyltransferase 3 and 4 (*β4-GalNAcT3,4*)	B4GALNT3, 4	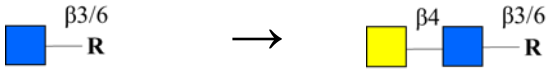	Requirement: Non-reducing terminal GlcNAcβ residue [105]
β-galactoside *α*-2,3-sialyltransferase (*ST3O*)	ST3GAL1, 2	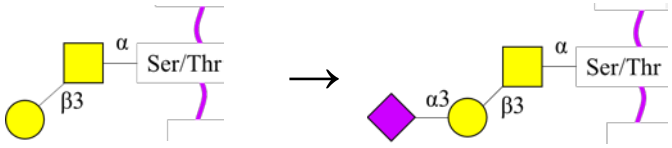	Requirement: Free 3-hydroxyl of Gal; Gal*β*1-3 residue of core 1 and 2 (Gal*β*1-3GalNAc) [120, 121].

Enzyme (*Short Name*)	Gene symbol	Substrate → Product	Requirement/restriction implemented in the model
		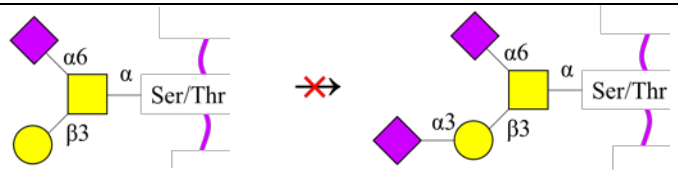	Restriction: Sialyl T and Tn antigens are not substrates. Prior sialylation of the Gal residue by ST6Gal precludes this reaction[4].
β-galactoside *α*-2,3-sialyltransferase 4 and 6 (*STZ* and *ST3GalVI*)	ST3GAL4, 6	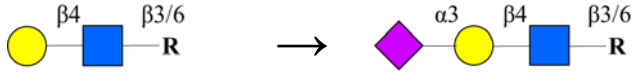	Requirement: Free 3-hydroxyl of Gal Restriction: Type 2 *N*-acetyllactosamine extensions (Gal*β*1-4GlcNAc-)$_n$ [120, 122]. I-branched chains were assumed to be substrates although they are not formed in the network.
			Restriction: type 2 chains with the inner GlcNAc being α1,3-fucosylated are not substrates [121].
β-galactoside *α*-2,3-sialyltransferase 3 (*ST3N*)	ST3GAL3	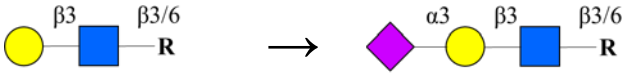	Requirement: Free 3-hydroxyl of Gal Restriction: Type 1 *N*-acetyllactosamine extensions (Gal*β*1-3GlcNAc-)$_n$ are substrates [123]. I-branched chains were assumed to be

[4] Assumed to simplify the model.

Enzyme (*Short Name*)	Gene symbol	Substrate → Product	Requirement/restriction implemented in the model
			substrates although they are not formed in the network.
			Restriction: type 1 chains with the inner GlcNAc being α1,4-fucosylated are not substrates [121].
α-N-acetylgalactosaminide *α*-2,6-sialyltransferase (*ST6GalNAc)*	ST6GALNAC1	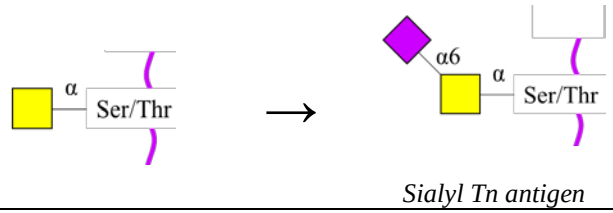 *Sialyl Tn antigen*	Requirement: Free 6-hydroxyl of GalNAc; Tn antigen, core 1, and α3-sialyl-T antigen are substrates [102]. Note: Because ST6GALNAC1 is primarily responsible for Sialyl-Tn antigen synthesis, the model only consider this activity of the enzyme [102].
		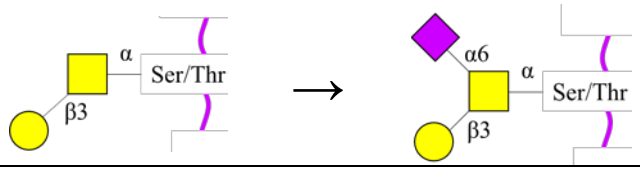	
		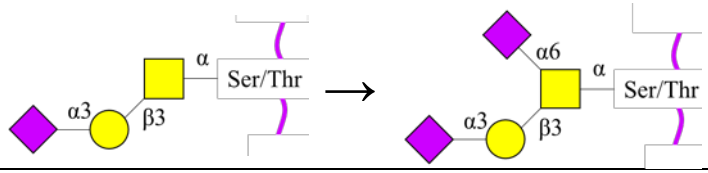	
	ST6GALNAC2, 1	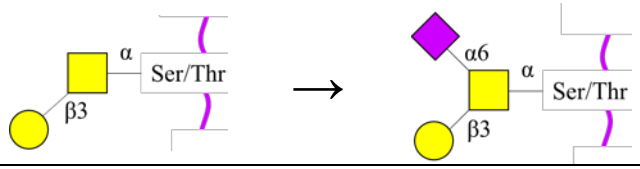	Requirement: Free 6-hydroxyl of GalNAc. Core 1 is the preferred substrate [124, 125].

Enzyme (*Short Name*)	Gene symbol	Substrate → Product	Requirement/restriction implemented in the model
		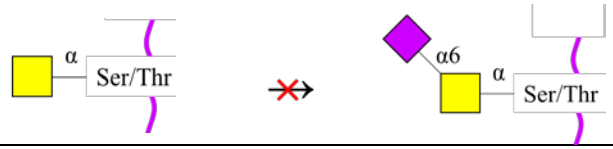	Restriction: Tn antigen is not a substrate. Low activity toward α3-sialyl-T antigen [124, 125]. Note: Because ST6GALNAC2 is not expressed in CHO-DG44 cells, this rule was disabled in the model.
		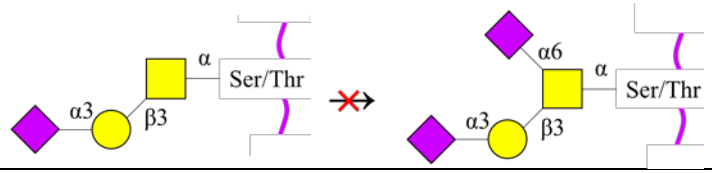	
	ST6GALNAC3,4 and 1,2	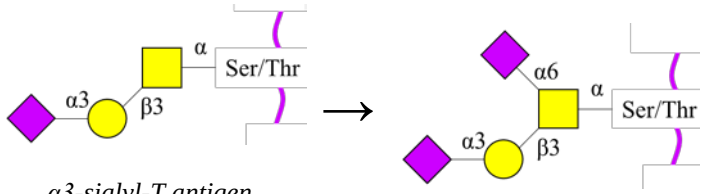 *α3-sialyl-T antigen*	Requirement: Free 6-hydroxyl of GalNAc Restriction: α3-sialyl-T antigen is a preferred substrate [126, 127]
		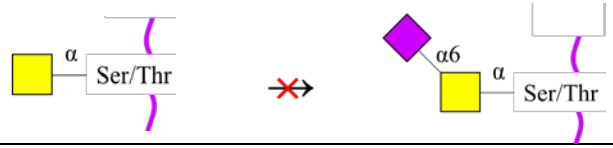	Restriction: very low or no activity toward Tn antigen [126, 127]
		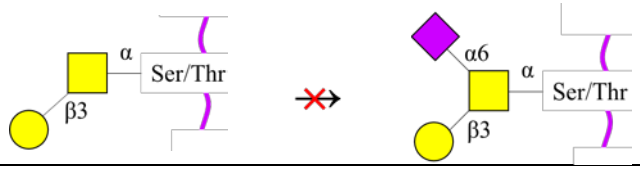	Restriction: very low or no activity toward core 1 [126, 127]

Enzyme (*Short Name*)	Gene symbol	Substrate → Product	Requirement/restriction implemented in the model
α-(1,2)-fucosyltransferase (*α2-FucT*)	FUT1, 2	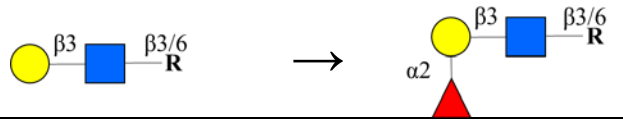	Requirement: type 1, 2 and 3 LacNAc chain. [128, 129]. Note: For type 3 LacNAc substrate, the activity was restricted to unmodified core 1 structure to simplify the model.
		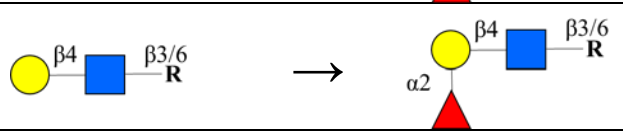	
		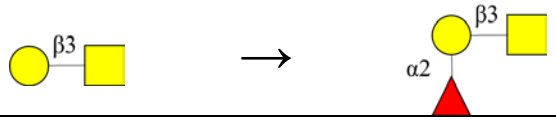	
		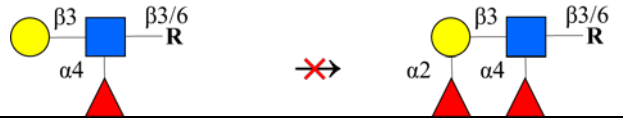	Restriction: α2-FUTs act before α3/4-FUTs [102].
		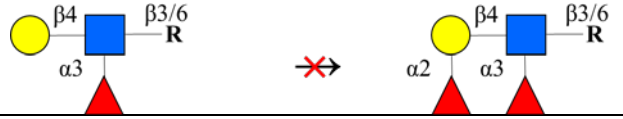	
α-(1,3/4)-fucosyltransferase (*α3/4-FucT*)	FUT3	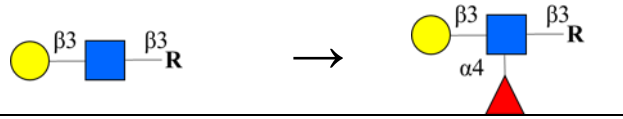	Requirement: type 1 and 2 chain. Restriction: Prior α2,3/6-sialylation of the outer Gal residue precludes the *α3-FucT* activity and prior α1,2-fucosylation of this Gal suppresses it [130].
		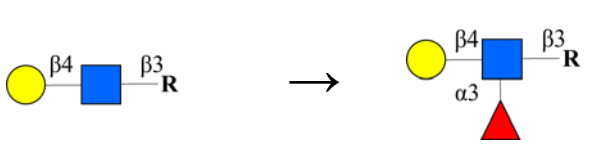	

Enzyme (*Short Name*)	Gene symbol	Substrate → Product	Requirement/restriction implemented in the model
			Note: Gal residues connected to the I-branched GlcNAc are not substrates.[5]
α-(1,3)-fucosyltransferase (*α3-FucT)*	FUT4	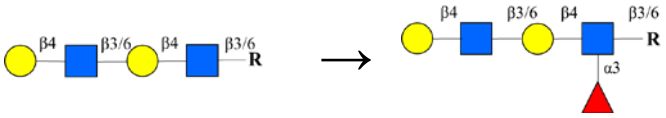	Requirement: The inner and distal GlcNAcβ residues of poly-*N*-acetyllactosamine (type 2 chains) [94, 131]. I-branched chains were assumed to be substrates. Restriction: The inner GlcNAcβ residue of neutral chains are preferred substrates [131].
	FUT7,4	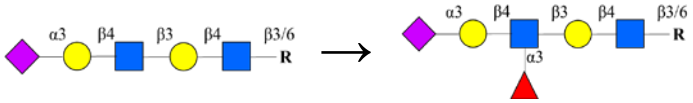	Requirement: The distal GlcNAcβ residue of sialylated poly-*N*-acetyllactosamine (type 2 chains) [94, 131, 132]. I-branched chains were assumed to be substrates.
			Restriction: Type 2 chains terminated with Neu5Acα2-3 (i.e. Neu5Acα2-3Galβ1-4GlcNAcβ1-) are substrates. Neutral chains are NOT substrates [94].

[5] Assumed to simplify the model.

Appendix Table 4. List of O-glycosyltransferases expressed in four different cell lines and the enzymatic activities considered in the O-glycosylation network.

ENZYMATIC ACTIVITY	GENE	Expressed (Y) or Not Expressed (N)			
		CHO	HUVEC	T47D	MCF7
β3-GalT	**B3GALT5**	Y	N	N	N
β3-GlcNAcT	**B4GAT1 (B3GNT1)**	Y	Y	Y	Y
	B3GNT2	Y	Y	Y	Y
	B3GNT3 *(Core 1 extension)*	Y	N	Y	Y
	B3GNT4	Y	N	Y	Y
	B3GNT6 *(Core 3 GnT)*	N	N	N	Y (very low)
	B3GNT7	Y	Y (very low)	Y (very low)	Y (very low)
	B3GNT8	Y	Y	N	Y (very low)
Cad β4-GalNAcT	**B4GALNT2**	Y	N	Y	Y
β4-GalNAcT	**B4GALNT3**	Y	N	Y	Y (very low)
	B4GALNT4	Y	Y (very low)	Y	Y
β4-GalT	**B4GALT1**	Y	Y	Y	Y
	B4GALT2	Y	Y	Y	Y
	B4GALT3	Y	Y	Y	Y
	B4GALT4	Y	Y	Y	Y
Core 1 β3-GalT	**C1GALT1**	Y	Y	Y	Y
α2-FucT	**FUT1**	N/A	Y	Y	Y
	FUT2	N/A	N	Y (very low)	Y
α4-FucT	**FUT3**	N/A	N	N	N
α3-FucT	**FUT4**	Y	Y	Y	Y
	FUT5	N/A	N	N	Y (very low)
	FUT6	N/A	N	N	N

	FUT7	Y	N	Y (very low)	Y (very low)
	FUT9	N/A	N	Y (very low)	Y
Polypeptide GalNAc-T	**GALNT1-18**	Y	Y	Y	Y
Core 2 β6-GlcNAcT	**GCNT1**	Y	Y	N	Y
	GCNT3	N	N	N	Y (very low)
	GCNT4	Y	N	N	N
IGnT	**GCNT2**	N	Y	Y (very low)	N
α3-SiaT	**ST3GAL1**	Y	Y	Y	Y
	ST3GAL2	Y	Y	Y	Y
	ST3GAL3	Y	Y	Y	Y
	ST3GAL4	Y	Y	Y	Y
	ST3GAL6	Y	Y	Y	N
α6-SiaT	**ST6GALNAC1**	Y	N	N	N
	ST6GALNAC2	N	N	Y	Y
	ST6GALNAC3	N	Y	N	N
	ST6GALNAC4	Y	Y	Y	Y
A-transferase B-transferase	**ABO**	Y	N	N	N

Appendix Table 5. Some examples of glycan structures that violate global constraints.

Constraint #	SNFG representation	Causes of violation
1	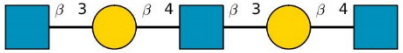 GlcNAc(β1-3)Gal(β1-4)GlcNAc(β1-3)Gal(β1-4)GlcNAc	Extends beyond two repeats of Type 2 chain.
	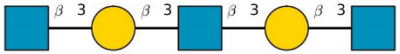 GlcNAc(β1-3)Gal(β1-3)GlcNAc(β1-3)Gal(β1-3)GlcNAc	Extends beyond two repeats of Type 1 chain.
	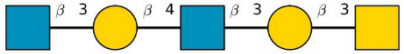 GlcNAc(β1-3)Gal(β1-4)GlcNAc(β1-3)Gal(β1-3)GalNAc	Extends beyond Type 2 + Type 3 chain.
	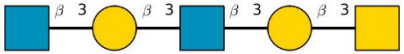 GlcNAc(β1-3)Gal(β1-3)GlcNAc(β1-3)Gal(β1-3)GalNAc	Extends beyond Type 1 + Type 3 chain.
	 GlcNAc(β1-3)Gal(β1-4)GlcNAc(β1-6)Gal(β1-4)GlcNAc	Extends beyond two repeats of Type 2 chain with I antigen.
2	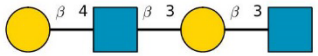 Galβ1-4GlcNAcβ1-3Galβ1-3GlcNAc	A hybrid structure between Type 2 and Type 1.
	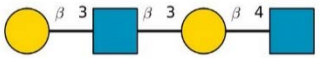 Galβ1-3GlcNAcβ1-3Galβ1-4GlcNAc	A hybrid structure between Type 1 – Type 2.
	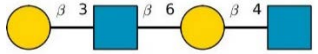 Galβ1-4GlcNAcβ1-6Galβ1-3GlcNAc	A hybrid structure between Type 2 and Type 1, linked via I-antigen.

3	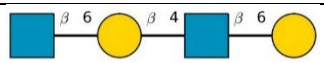 GlcNAcβ1-6Galβ1-4GlcNAcβ1-6Gal	Two consecutive I-antigens linked via type 2 chain.
	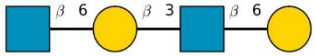 GlcNAcβ1-6Galβ1-3GlcNAcβ1-6Gal	Two consecutive I-antigens linked via type 1 chain.
4	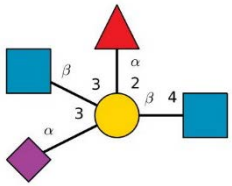 GlcNAc(β1-3)[Fuc(α1-2)][Neu5Ac(α2-3)]Gal(β1-4)GlcNAc	A galactose is linked to four other monosaccharides including Neu5Ac, Fuc, and two GlcNAc
5	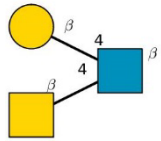 Gal(β1-4)[GalNAc(β1-4)]GlcNAc	C4 of the GlcNAc is linked to two other monosaccharides (Gal and GalNAc)

Appendix Table 6. List of O-glycans secreted from Human Umbilical Vein Cells (HUVEC).

Composition	Glycan ID		Structure[6]
	[91][7]	Current work	
$GalNAc_1GlcNAc_0Gal_1Neu5Ac_0Fuc_1$	**1**	299	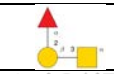
$GalNAc_1GlcNAc_0Gal_1Neu5Ac_1Fuc_0$	**2**	474	
$GalNAc_1GlcNAc_0Gal_1Neu5Ac_1Fuc_0$	**3**	n/a[8]	
$GalNAc_1GlcNAc_1Gal_2Neu5Ac_0Fuc_0$	**4**	166	
$GalNAc_1GlcNAc_0Gal_1Neu5Ac_1Fuc_1$	**5**	n/a	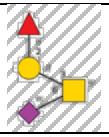
$GalNAc_1GlcNAc_1Gal_2Neu5Ac_0Fuc_1$	**7**	265	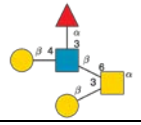
$GalNAc_1GlcNAc_1Gal_2Neu5Ac_0Fuc_1$	**8**	168	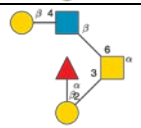
$GalNAc_1GlcNAc_0Gal_1Neu5Ac_2Fuc_0$	**10**	502	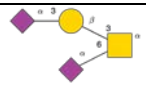

[6] Shaded structures were not predicted by the program.
[7] The ID sequence is not continuous because only IDs of glycans detected in HUVEC cells were shown. The IDs of glycans only detected in other cells were omitted.
[8] Not predicted by the program

$GalNAc_1GlcNAc_1Gal_2Neu5Ac_0Fuc_2$	**11**	267	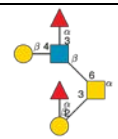
$GalNAc_1GlcNAc_1Gal_2Neu5Ac_1Fuc_0$	**13**	172	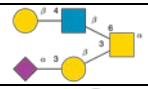
$GalNAc_1GlcNAc_1Gal_2Neu5Ac_1Fuc_0$	**14**	82	
$GalNAc_1GlcNAc_2Gal_3Neu5Ac_0Fuc_0$	**16**	103	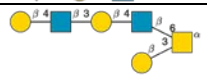
$GalNAc_1GlcNAc_1Gal_2Neu5Ac_1Fuc_1$	**18**	173	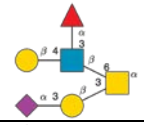
$GalNAc_1GlcNAc_1Gal_2Neu5Ac_1Fuc_1$	**19**	171	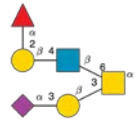
$GalNAc_1GlcNAc_2Gal_3Neu5Ac_0Fuc_1$	**22**	94	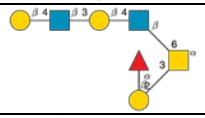
$GalNAc_1GlcNAc_2Gal_3Neu5Ac_0Fuc_1$	**23**	214	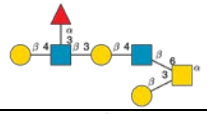
$GalNAc_1GlcNAc_1Gal_2Neu5Ac_2Fuc_0$	**24**	491	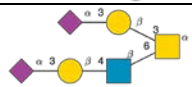
$GalNAc_1GlcNAc_2Gal_3Neu5Ac_0Fuc_2$	**26**	217	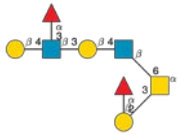
$GalNAc_1GlcNAc_2Gal_3Neu5Ac_1Fuc_0$	**28**	100	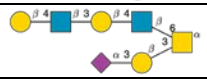

$GalNAc_1GlcNAc_2Gal_3Neu5Ac_1Fuc_0$	**29**	89	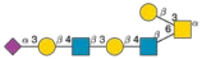
$GalNAc_1GlcNAc_1Gal_2Neu5Ac_2Fuc_1$	**30**	n/a	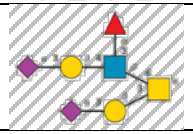
$GalNAc_1GlcNAc_2Gal_3Neu5Ac_1Fuc_1$	**33**	211	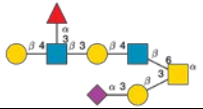
$GalNAc_1GlcNAc_2Gal_3Neu5Ac_1Fuc_1$	**34**	163	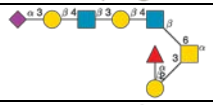
$GalNAc_1GlcNAc_2Gal_3Neu5Ac_2Fuc_0$	**38**	495	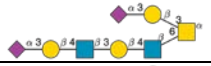
$GalNAc_1GlcNAc_3Gal_4Neu5Ac_1Fuc_0$	**41**	71 75	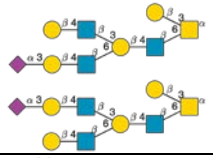
$GalNAc_1GlcNAc_3Gal_4Neu5Ac_1Fuc_0$	**42**	160 n/a	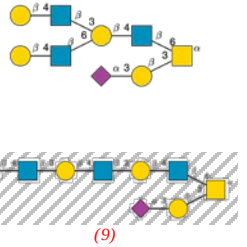 *(9)*
$GalNAc_1GlcNAc_3Gal_4Neu5Ac_1Fuc_0$	**43**	n/a	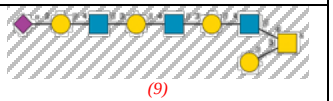 *(9)*
$GalNAc_1GlcNAc_2Gal_3Neu5Ac_2Fuc_1$	**44**	481	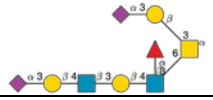

(9) The length of LacNAc chain in this structure exceeds the maximal length imposed in the global constraints.

$GalNAc_1GlcNAc_3Gal_4Neu5Ac_1Fuc_1$	**47**	67 279	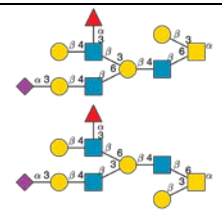
$GalNAc_1GlcNAc_3Gal_4Neu5Ac_1Fuc_1$	**48**	157 179 n/a	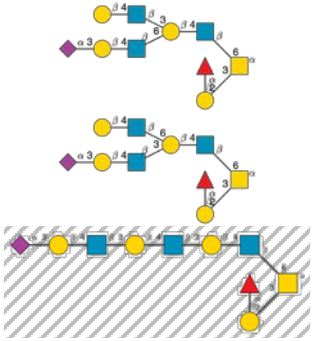 *(9)*
$GalNAc_1GlcNAc_3Gal_4Neu5Ac_1Fuc_1$	**49**	156 181	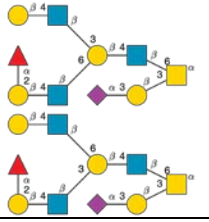
$GalNAc_1GlcNAc_3Gal_4Neu5Ac_1Fuc_2$	**56**	400	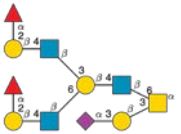
$GalNAc_1GlcNAc_3Gal_4Neu5Ac_1Fuc_2$	**57**	210	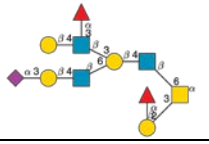

$GalNAc_1GlcNAc_3Gal_4Neu5Ac_2Fuc_0$	**58**	182 158	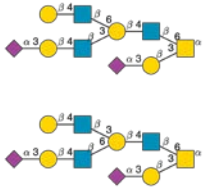
$GalNAc_1GlcNAc_3Gal_4Neu5Ac_2Fuc_0$	**59**	70	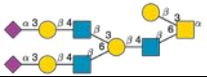
$GalNAc_1GlcNAc_4Gal_5Neu5Ac_1Fuc_0$	**62**	n/a	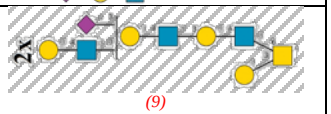 *(9)*
$GalNAc_1GlcNAc_3Gal_4Neu5Ac_2Fuc_1$	**63**	213	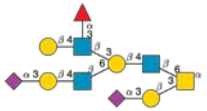
$GalNAc_1GlcNAc_4Gal_5Neu5Ac_1Fuc_1$	**65**	n/a	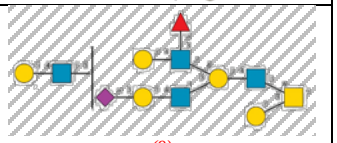 *(9)*
$GalNAc_1GlcNAc_4Gal_5Neu5Ac_1Fuc_1$	**66**	n/a	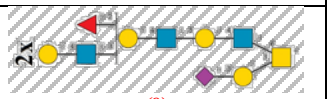 *(9)*
$GalNAc_1GlcNAc_3Gal_4Neu5Ac_3Fuc_0$	**70**	501	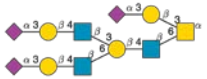
$GalNAc_1GlcNAc_4Gal_5Neu5Ac_2Fuc_0$	**73**	n/a	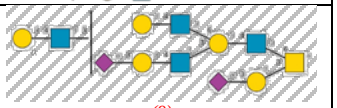 *(9)*
$GalNAc_1GlcNAc_4Gal_5Neu5Ac_2Fuc_1$	**74**	n/a	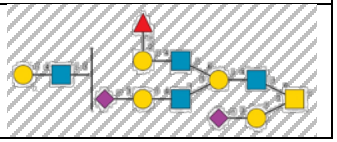

			(9)
$GalNAc_1GlcNAc_4Gal_5Neu5Ac_3Fuc_0$	**76**	n/a	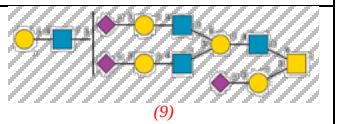 *(9)*

8.2 APPENDIX FIGURES

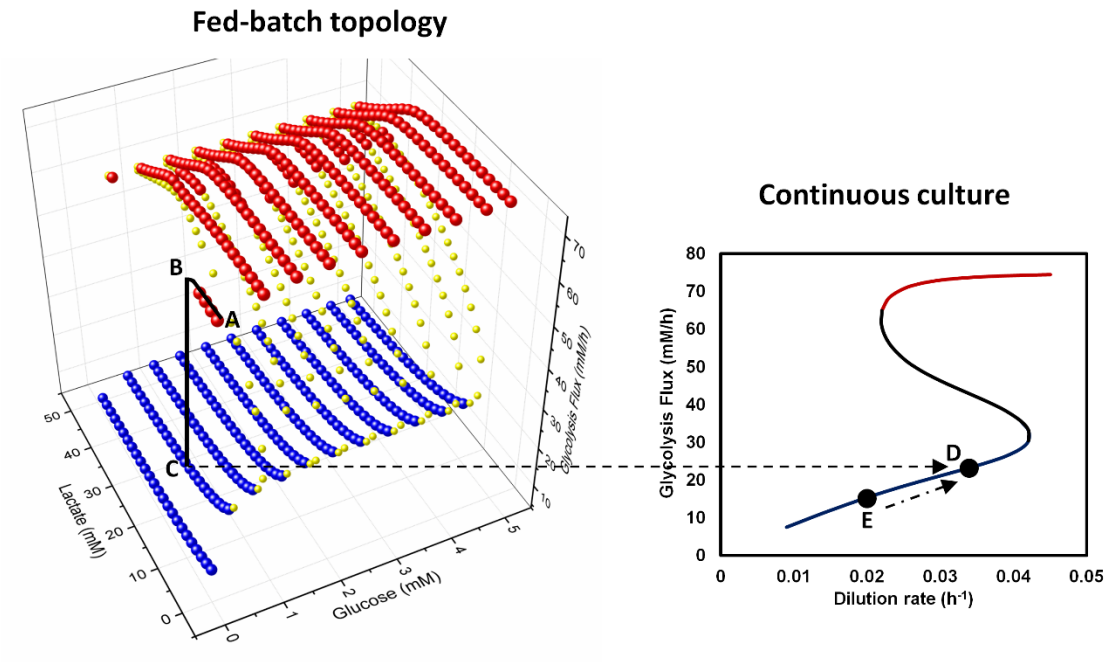

Appendix Figure 1. Strategies for guiding continuous culture to steady state with a low glycolysis flux.

Two strategies for directing a continuous culture to low flux state are depicted. (A-D) Cells cultured in fed-batch with glucose maintained at 0.5 mM undergo a metabolic shift to low flux state. Once a low flux state is reached, the culture can be switched to a continuous mode with a dilution rate located in the bistable region (0.033 h^{-1} in this example). The continuous culture will remain at low flux state and reaches steady state with a low metabolic flux and higher cell concentration. (E-D) Without controlling glucose at a low level, the continuous culture will reach steady state with low glycolysis flux only when it is operated at a low dilution rate (<0.021 h^{-1}). In the low dilution rate region, the only existing steady states are those with low glycolysis flux. The dilution rate can then be incrementally increased to a final dilution rate that is located in the bistable region (0.033 h^{-1} in this example). The culture will remain at low flux state and settles to steady state with a low flux and higher cell concentration. (Courtesy of Dr. Andrew Yongky)

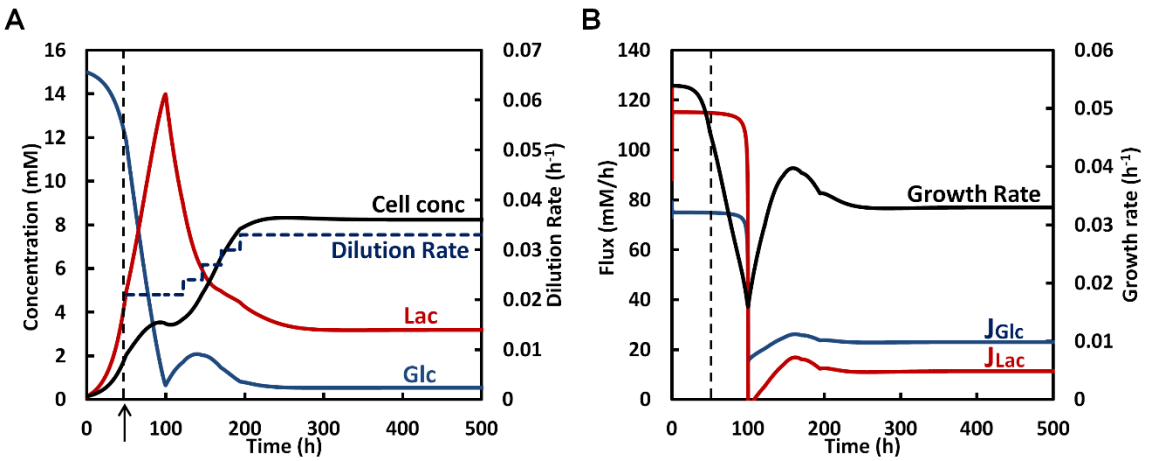

Appendix Figure 2. Directing continuous culture to steady state with a low glycolysis flux by controlling dilution rate.

The culture was started in batch mode and exhibits high metabolic flux. The culture is then switched to a continuous mode with a dilution rate of 0.021 h^{-1} and feed glucose concentration of 7 mM. By operating at a low dilution rate, the culture reaches a steady state with low metabolic flux. Incrementally increasing the dilution rate to a final rate of 0.033 h^{-1} allows the culture to remain at low flux and reaches a final steady state with higher cell concentration (compared to Figure 6.3A). Arrow (↑) indicates the time at which continuous mode is initiated (courtesy of Dr. Andrew Yongky).

Appendix Figure 3. Demonstration of the algorithm used to translate glycan strings from their SMILES format into the modified IUPAC condensed nomenclature.

Blue text indicates the portions of the input string that have been processed. Asterisks (*) indicate parentheses recorded by the algorithm. Underlined text indicates the paused position in the string.

Description of the algorithm:

The algorithm first preprocesses the SMILES format of a glycan to remove brackets enclosing monosaccharides, monosaccharide carbons, glycosidic bonds and polypeptide backbone. Next, the algorithm identifies the Ser/Thr residue of the polypeptide backbone and sets it as the starting point (step 1). It then steps from right to left in the SMILES string,

and at the same time, adds processed monosaccharides to the growing output string (step 2).

Branch search process: The algorithm pauses once a branch point of the glycan structure is reached, as indicated by an open parenthesis (step 2). The first monosaccharide on the left of the open parenthesis is the parent of upcoming branches (e.g. *GalNAc* in step 3). The algorithm then steps from left to right in the SMILES string to identify all the monosaccharides that are branched off from the parent monosaccharide (step 3, 4, 5 and 6). This process hereinafter will be referred to as "branch search". The branch search terminates when the corresponding close parenthesis is encountered. After the branch search finishes, all the processed branches are added to the output string. Any branch that was previously added to the output string while the algorithm stepped from right to left will be skipped (e.g. *c1a SerThr-pp-Pro* in step 3). The algorithm then returns to the parent monosaccharide and continues to step from right to left in the SMILES string (step 7). Another open parenthesis is encountered, indicating a potential branch point (e.g. *GlcNAc* in step 8). Here, the algorithm performs another branch search for GlcNAc (step 8, 9 and 10).

The branch search is carried out based on a recursive algorithm. During a branch search, if the algorithms identify any sub-branch point, indicated by another open parenthesis (step 4), the current search is paused, and another nested search begins to identify all sub-branches. After all the sub-branches are identified, the paused search resumes.

In addition to monosaccharides, monosaccharide carbons that are involved in glycosidic bonds formation are also added to the output string following the modified

IUPAC condensed nomenclature. Monosaccharide carbons that are not involved in glycosidic bond formations (i.e. not adjacent to ‘a’ or ‘b’, which represents for alpha or beta glycosidic bond) are ignored (e.g. carbons *c3* and *c6* of *Gal* in step 6).

The algorithm terminates after the leftmost monosaccharide (e.g. *GlcNAc* in step 10) in the SMILES string is added to the output string.

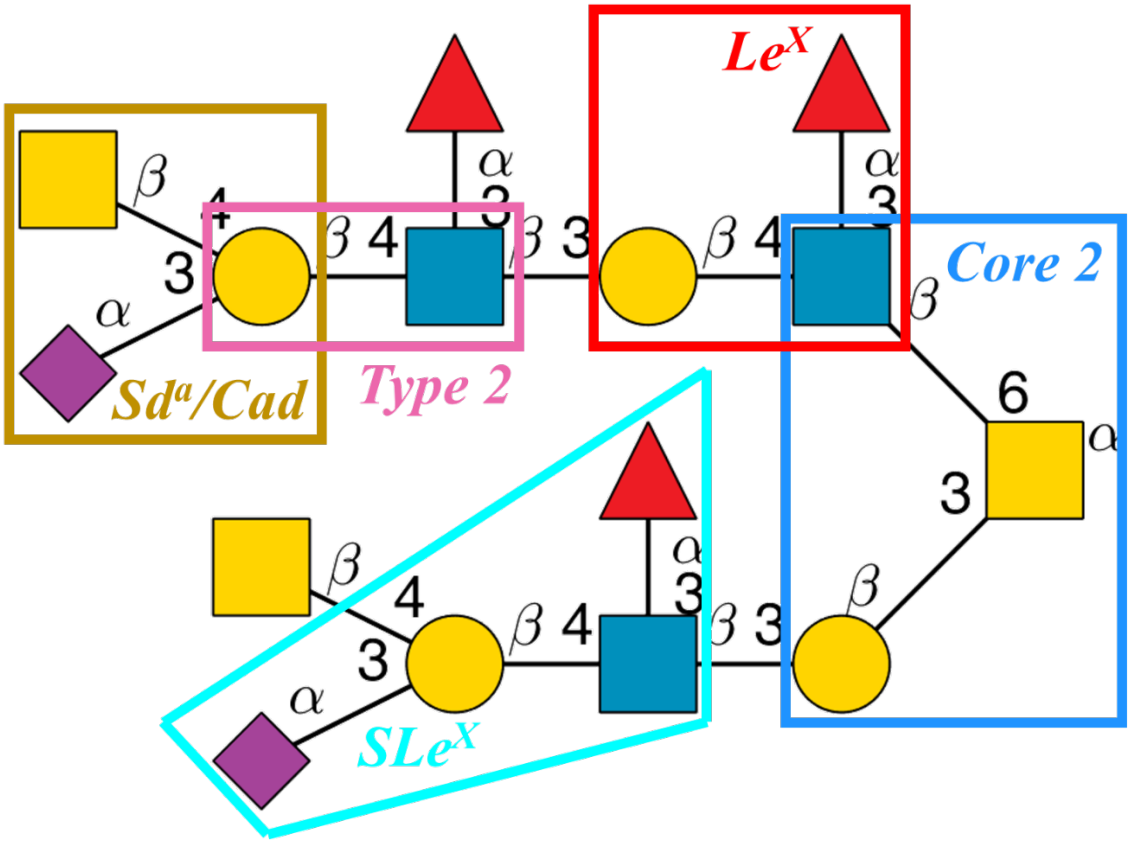

Appendix Figure 4. An example of an O-glycan that carries multiple epitopes on its structure.

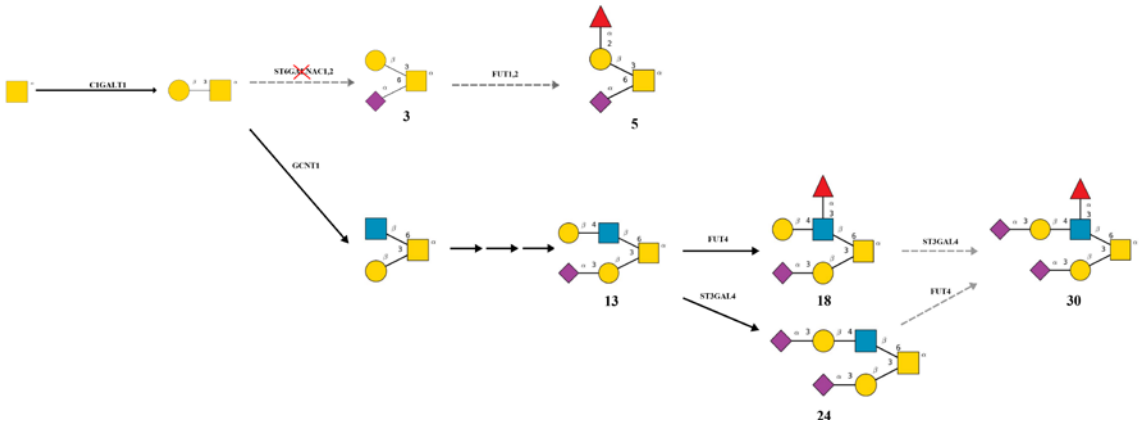

Appendix Figure 5. Potential reaction paths leading to the three glycans that were not predicted by the program.

The number under each glycan structure is the glycan ID used by Kudelka et al. 2016 (see Appendix Table 6). Glycan structures without IDs are those not reported in the paper. Solid arrows indicate reactions that were predicted by O-GlycoVis and dashed arrows represent unpredicted reactions. The red cross mark indicates enzymes that are not expressed in the HUVEC TERT2 cells.

8.3 APPENDIX MATERIALS

8.3.1 Rate Equations

Reproduced from: Mulukutla, B.C., et al., *Multiplicity of Steady States in Glycolysis and Shift of Metabolic State in Cultured Mammalian Cells.* Plos One, 2015. **10**(3).

GLYCOLYSIS

Hexokinase (HK): The rate equation for HK was taken from Mulquiney et al. [133]. The kinetic constants which correspond to those of the isozyme HK2 were adopted from previous literature [134-138]. The rate equation employs the partial rapid equilibrium random bi-bi mechanism with the assumption that all the steps in the mechanism, except for the reactive-ternary complexes, are fast reactions. The inhibitions by *g6p*, glucose-1,6-phosphate (*g16bp*), 2,3-bisphosphoglycerate (*2,3bpg*) and glutathione (*gsh*) were modeled as a mixed type of inhibition affecting both the activity (V_{max}) as well as the affinity (K_M) of the enzyme for glucose.

Equation S1. Hexokinase (HK)

$$r_{HK} = \left(V_{mf}^{HK} \frac{C_{MgATP}^{c} C_{glc}^{c}}{K_{MgATP}^{HK} K_{glc}^{HK}} - V_{mr}^{HK} \frac{C_{MgADP}^{c} C_{g6p}^{c}}{K_{i,MgADP}^{HK} K_{g6p}^{HK}} \right) \frac{1}{N_{HK}}$$

$$N_{HK} = \left(1 + \frac{C_{MgATP}^{c}}{K_{i,MgATP}^{HK}} + \frac{C_{g6p}^{c}}{K_{i,g6p}^{HK}} + \frac{C_{glc}^{c}}{K_{glc}^{HK}} + \frac{C_{MgATP}^{c} C_{glc}^{c}}{K_{MgATP}^{HK} K_{glc}^{HK}} + \frac{C_{MgADP}^{c}}{K_{i,MgADP}^{HK}} + \frac{C_{MgADP}^{c} C_{g6P}^{c}}{K_{i,MgADP}^{HK} K_{g6P}^{HK}} \right.$$
$$\left. + \frac{C_{glc}^{c} C_{g6P}^{c}}{K_{glc}^{HK} K_{g6P}^{HK}} + \frac{C_{glc}^{c} C_{g16bp}^{c}}{K_{glc}^{HK} K_{i,g16bp}^{HK}} + \frac{C_{glc}^{c} C_{2,3bpg}^{c}}{K_{glc}^{HK} K_{i,2,3bpg}^{HK}} + \frac{C_{glc}^{c} C_{gsh}^{c}}{K_{glc}^{HK} K_{i,gsh}^{HK}} \right)$$

$V_{mf}^{HK} = 9.59*10^{2}\ mM\ h^{-1}$
$V_{mr}^{HK} = 6.18\ mM\ h^{-1}$
$K_{MgATP}^{HK} = 1.0\ mM$
$K_{glc}^{HK} = 0.1\ mM$
$K_{i,MgADP}^{HK} = 1.0\ mM$
$K_{g6p}^{HK} = 0.47 mM$
$K_{i,g6p}^{"HK} = 2*10^{-2} mM$
$K_{i,g16bp}^{HK} = 3*10^{-2} mM$
$K_{i,gsh}^{HK} = 3.0\ mM$

The rate equations and kinetic constants for hexokinase isoforms. Isoform-specific parameters are colored blue.

$$r_{HK_i} = \left(V_{mf}^{HK} \frac{C_{MgATP}^c C_{glc}^c}{K_{MgATP}^{HK} K_{glc}^{HK_i}} - V_{mr}^{HK} \frac{C_{MgADP}^c C_{g6p}^c}{K_{i,MgADP}^{HK} K_{g6p}^{HK_i}} \right) \frac{1}{N_{HK}}$$

$$N_{HK_i} = \left(1 + \frac{C_{MgATP}^c}{K_{i,MgATP}^{HK}} + \frac{C_{glc}^c}{K_{glc}^{HK_i}} + \frac{C_{MgATP}^c C_{glc}^c}{K_{MgATP}^{HK} K_{glc}^{HK_i}} + \frac{C_{g6p}^c}{K_{i,g6p}^{"HK_i}} + \frac{C_{MgADP}^c}{K_{i,MgADP}^{HK}} + \frac{C_{MgADP}^c C_{g6P}^c}{K_{i,MgADP}^{HK} K_{g6P}^{HK_i}} + \frac{C_{glc}^c C_{g6P}^c}{K_{glc}^{HK_i} K_{g6p-glc}^{HK_i}} + \frac{C_{glc}^c C_{g16bp}^c}{K_{glc}^{HK_i} K_{i,g16bp}^{HK}} + \frac{C_{glc}^c C_{2,3bpg}^c}{K_{glc}^{HK_i} K_{i,2,3bpg}^{HK}} + \frac{C_{glc}^c C_{gsh}^c}{K_{glc}^{HK_i} K_{i,gsh}^{HK}} \right)$$

$$r_{HK} = \sum_{i=1}^{4} \rho_{HK_i} r_{HK_i}$$

$V_{mf}^{HK} = 9.59*10^{2} mM\ h^{-1}$

$V_{mr}^{HK} = 6.18\ mM\ h^{-1}$

$K_{MgATP}^{HK} = 1.0\ mM$

$K_{i,MgADP}^{HK} = 1.0\ mM$

$K_{g6p}^{HK} = 0.47 mM$

$K_{i,g6p}^{"HK} = 0.47 mM$

$K_{i,g16bp}^{HK} = 3*10^{-2} mM$

$K_{i,gsh}^{HK} = 3.0\ mM$

	$K_{glc}^{HK_i}$ [139]	$K_{g6p-glc}^{HK_i}$ [139]
HK1	0.47	0.021
HK2	0.26	0.016
HK3	0.007	0.092
HK4 (GCK)	7.7	No inhibition

	ρ_{HK_i}			
	D6	D10	D14	D20
HK1	0.60	0.26	0.42	0.51
HK2	0.25	0.26	0.23	0.32
HK3	0.07	0.08	0.08	0.07
HK4 (GCK)	0.08	0.08	0.08	0.07

Glucose Phosphate Isomerase (GPI): The rate equation for GPI was taken from Mulquiney et al. [133]. The kinetic constants were adopted from previous literature [140-142]. The rate equation employs the steady state uni uni reaction kinetics.

Equation S2. Glucose Phosphate Isomerase (GPI)

$$r_{GPI} = \frac{V_{mf}^{GPI}\frac{C_{g6p}^{c}}{K_{f}^{GPI}} - V_{mr}^{GPI}\frac{C_{f6p}^{c}}{K_{r}^{GPI}}}{1+\frac{C_{g6p}^{c}}{K_{f}^{GPI}}+\frac{C_{f6p}^{c}}{K_{r}^{GPI}}}$$

$$V_{mf}^{GPI} = 2.4*10^{3} mM\ h^{-1}$$
$$V_{mr}^{GPI} = 2.0*10^{3} mM\ h^{-1}$$
$$K_{f}^{GPI} = 9.6*10^{-1} mM$$
$$K_{r}^{GPI} = 1.23*10^{-1} mM$$

Phosphofructokinase (PFK): The rate equation for PFK was taken from Mulquiney et al. [133]. The kinetic constants were adopted from previous literature [143-147]. The rate kinetics was based on the two-state allosteric model using ordered bi bi mechanism. The two-state model considers that the enzyme can exist in the active or the non-active state as determined by the levels of the activity modulators. These include activators (*f16bp, f26bp, g16bp,* AMP etc) and inhibitors (ATP, Mg etc). These activity modulators are isozyme-specific. For example, *f16bp* only stimulates PFKM and PFKL. The fraction of the enzyme in the active state is represented by the nonlinear term N_{PFK} which is a function of the levels of the activity modulators. L_{PFK} represents the equilibrium constant between the two states of the enzyme in the absence of any substrates. The initial velocity expression for the enzyme fraction in the active state was modeled as partial rapid equilibrium random bi bi steady state equation similar to the HK kinetics.

Equation S3. Phosphofructokinase (PFK)

$$r_{PFK} = \frac{\frac{V_f^{PFK} C_{MgATP}^c C_{f6p}^c}{K_{f6p}^{PFK} K_{MgATP}^{PFK}} - \frac{V_r^{PFK} C_{MgADP}^c C_{f16bp}^c}{K_{f16bp}^{PFK} K_{MgADP}^{PFK}}}{\left(\left(1+\frac{C_{f6p}^c}{K_{f6p}^{PFK}}\right)\left(1+\frac{C_{MgATP}^c}{K_{MgATP}^{PFK}}\right)+\left(1+\frac{C_{f16bp}^c}{K_{f16bp}^{PFK}}\right)\left(1+\frac{C_{MgADP}^c}{K_{MgADP}^{PFK}}\right)-1\right)} \frac{1}{N_{PFK}}$$

$$N_{PFK} = 1 + \frac{L_{PFK}\left(1+\frac{C_{ATP}^c}{K_{ATP}^{PFK}}\right)^4\left(1+\frac{C_{Mg}^c}{K_{Mg}^{PFK}}\right)^4\left(1+\frac{C_{2,3bpg}^c}{K_{2,3bpg}^{PFK}}\right)^4\left(1+\frac{C_{Lac}^c}{K_{Lac}^{PFK}}\right)^4}{\left(1+\frac{C_{f6p}^c}{K_{f6p}^{PFK}}+\frac{C_{f16bp}^c}{K_{f16bp}^{PFK}}\right)^4\left(1+\frac{C_{AMP}^c}{K_{AMP}^{PFK}}\right)^4\left(1+\frac{C_{g16bp}^c}{K_{g16bp}^{PFK}}\right)^4\left(1+\frac{C_{Pi}^c}{K_{Pi}^{PFK}}\right)^4\left(1+\frac{C_{f26bp}^c}{K_{f26bp}^{PFK}}\right)^4}$$

$V_f^{PFK} = 2.63*10^2\ mM^{-1}h^{-1}$
$V_r^{PFK} = 11.53\ mM^{-1}h^{-1}$
$K_{f6p}^{PFK} = 6*10^{-2}\ mM$
$K_{MgATP}^{PFK} = 6.8*10^{-2}\ mM$
$K_{MgADP}^{PFK} = 0.54\ mM$
$K_{ATP}^{PFK} = 0.1\ mM$
$K_{AMP}^{PFK} = 0.3\ mM$
$K_{Mg}^{PFK} = 0.2\ mM$
$K_{Pi}^{PFK} = 30\ mM$
$K_{f16bp}^{PFK} = 0.3\ mM$
$K_{f26bp}^{PFK} = 5.5*10^{-3} mM$
$K_{g16bp}^{PFK} = 0.1\ mM$
$K_{23bpg}^{PFK} = 0.5\ mM$
$L_{PFK} = 2*10^{-3}$
$K_{Lac}^{PFK} = 30\ mM$

The rate equations and kinetic constants for phosphofructokinase isoforms. Isoform-specific parameters are colored blue.

$$r_{PFK_i} = \frac{\frac{V_f^{PFK} C_{MgATP}^c C_{f6p}^c}{K_{f6p}^{PFK} K_{MgATP}^{PFK}} - \frac{V_r^{PFK_i} C_{MgADP}^c C_{f16bp}^c}{K_{f16bp}^{PFK_i} K_{MgADP}^{PFK}}}{\left(\left(1+\frac{C_{f6p}^c}{K_{f6p}^{PFK}}\right)\left(1+\frac{C_{MgATP}^c}{K_{MgATP}^{PFK}}\right)+\left(1+\frac{C_{f16bp}^c}{K_{f16bp}^{PFK_i}}\right)\left(1+\frac{C_{MgADP}^c}{K_{MgADP}^{PFK}}\right)-1\right)} \frac{1}{N_{PFK}}$$

$$N_{PFK_i} = 1 + \frac{L_{PFK}\left(1+\frac{C_{ATP}^c}{K_{ATP}^{PFK}}\right)^4\left(1+\frac{C_{Mg}^c}{K_{Mg}^{PFK}}\right)^4\left(1+\frac{C_{2,3bpg}^c}{K_{2,3bpg}^{PFK}}\right)^4\left(1+\frac{C_{Lac}^c}{K_{Lac}^{PFK}}\right)^4}{\left(1+\frac{C_{f6p}^c}{K_{f6p}^{PFK}}+\frac{C_{f16bp}^c}{K_{f16bp}^{PFK_i}}\right)^4\left(1+\frac{C_{AMP}^c}{K_{AMP}^{PFK}}\right)^4\left(1+\frac{C_{g16bp}^c}{K_{g16bp}^{PFK}}\right)^4\left(1+\frac{C_{Pi}^c}{K_{Pi}^{PFK}}\right)^4\left(1+\frac{C_{f26bp}^c}{K_{f26bp}^{PFK}}\right)^4}$$

$$r_{PFK} = \sum_{i=1}^{3} \rho_{PFK_i} r_{PFK_i}$$

$V_f^{PFK} = 2.63*10^2\ mM^{-1}h^{-1}$

$V_r^{PFK} = 11.53\ mM^{-1}h^{-1}$

$K_{f6p}^{PFK} = 6*10^{-2}\ mM$ $\quad K_{Pi}^{PFK} = 30\ mM$

$K_{MgATP}^{PFK} = 6.8*10^{-2}\ mM$ $\quad K_{g16bp}^{PFK} = 0.1\ mM$

$K_{MgADP}^{PFK} = 0.54\ mM$ $\quad K_{23bpg}^{PFK} = 0.5\ mM$

$K_{ATP}^{PFK} = 0.1\ mM$ $\quad L_{PFK} = 2*10^{-3}$

$K_{AMP}^{PFK} = 0.3\ mM$ $\quad K_{Lac}^{PFK} = 30\ mM$

$K_{Mg}^{PFK} = 0.2\ mM$

	K_{f16bp}^{PFK} [148]	K_{f26bp}^{PFK} [149]
PFKL	0.65	$5.5*10^{-3}$
PFKM	0.35	$5.5*10^{-3}$
PFKP	N.A.	$4.5*10^{-2}$

	ρ_{PFK_i}			
	D6	D10	D14	D20
PFKL	0.17	0.18	0.15	0.19
PFKM	0.46	0.36	0.34	0.30
PFKP	0.37	0.51	0.96	1.11

6-Phosphofructo-2-Kinase/Fructose-2,6-Bisphosphatase (PFKFB): The rate equation for PFKFB and the kinetic constants were taken from previously reported studies [150, 151]. PFKFB is a bi-functional enzyme with kinase and bisphosphatase activities, each localized to either terminals of the enzyme and are independent of each other's activity. The kinase domain catalyzes the synthesis of fructose-2,6-bisphosphate (*f26bp*) from fructose-6-phoshate (*f6p*) and the bisphosphatase domain mediates the hydrolysis of *f26bp* to *f6p*. The reaction kinetics for the kinase domain (r_{PFK2}) follows the ordered bi bi steady state kinetics, with phosphoenolpyurvate (*pep*) inhibition of the kinase domain modeled as non-competitive inhibition. The bisphosphatase reaction kinetics ($r_{F2,6BPase}$) was modeled as simple Michaelis-Menten kinetics with non-competitive product inhibition by *f6p*. Isozymes of PFKFB vary in their kinase to bisphosphatase activity (K/P) [152]. The effect

of isozyme (or K/P) was modeled by changing the Vmax of r_{PFK2} and holding $r_{F2,6BPase}$ constant.

Equation S4. 6-Phosphofructo-2-Kinase/Fructose-2,6-Bisphosphatase (PFKFB)

$$r_{PFK2} = \frac{V_{f,PFK2}\left(C^c_{ATP}C^c_{f6p} - \frac{C^c_{ADP}C^c_{f26bp}}{K_{eq,PFK2}}\right)\left(0.2 + \frac{0.8}{1+\frac{K_{AKT}}{pAKT}}\right)}{\left(K^{PFK2}_{i,ATP}K^{PFK2}_{m,f6p} + K^{PFK2}_{m,f6p}C^c_{ATP} + K^{PFK2}_{m,ATP}C^c_{f6p} + \frac{K^{PFK2}_{m,ADP}C^c_{f26bp}}{K_{eq,PFK2}} + C^c_{ATP}C^c_{f6p} + \frac{K^{PFK2}_{m,f26bp}C^c_{ADP}}{K_{eq,PFK2}} + \frac{K^{PFK2}_{m,ADP}C^c_{ATP}C^c_{f26bp}}{K_{eq,PFK2}K^{PFK2}_{i,ATP}} + \frac{C^c_{ADP}C^c_{f26bp}}{K_{eq,PFK2}} + \frac{K^{PFK2}_{m,ATP}C^c_{ADP}C^c_{f6p}}{K^{PFK2}_{i,ADP}} + \frac{C^c_{ATP}C^c_{f6p}C^c_{f26bp}}{K^{PFK2}_{i,f26bp}} + \frac{C^c_{ADP}C^c_{f6p}C^c_{f26bp}}{K_{eq,PFK2}K^{PFK2}_{i,f6p}}\right)\left(1+\frac{C^c_{pep}}{K^{PFK2}_{i,pep}}\right)}$$

$V_{f,PFK2} = 300\ mM\ h^{-1}$
$K^{PFK2}_{m,ATP} = 0.15\ mM$
$K^{PFK2}_{m,f6p} = 0.032\ mM$
$K^{PFK2}_{m,f26bp} = 0.008\ mM$
$K^{PFK2}_{m,ADP} = 0.062\ mM$
$K^{PFK2}_{i,ATP} = 0.15\ mM$
$K^{PFK2}_{i,f6p} = 0.001\ mM$
$K^{PFK2}_{i,f26bp} = 0.02\ mM$
$K^{PFK2}_{i,ADP} = 0.23\ mM$
$K^{PFK2}_{i,pep} = 0.013\ mM$
$K^{PFK2}_{eq} = 16$
$K_{AKT} = 0.5$

$$r_{F2,6BPase} = \frac{V_{F2,6BPase}C^c_{f26bp}}{\left(1+\frac{C^c_{f6p}}{K^{F2,6BPase}_{i,f6p}}\right)\left(K^{F2,6BPase}_{m,f26bp} + C^c_{f26bp}\right)}$$

$V_{F2,6BPase} = 13.86\ mM^{-1}h^{-1}$
$K^{F2,6BPase}_{m,f26bp} = 10^{-3}\ mM$
$K^{F2,6BPase}_{i,f6p} = 25*10^{-3}\ mM$

<u>Aldolase</u> (ALDO): The rate equation for ALDO was taken from Mulquiney et al. [133]. The kinetic constants were adopted or estimated from previous literature [153-162]. The reaction kinetics of ALDO follows the ordered uni bi steady state kinetics. Inhibition due to *2,3bpg* as described in the original expression was retained in this study. However, since *2,3bpg* is not a reaction intermediate considered in the model, its concentration was held constant for the purpose of this study.

Equation S5. Aldolase (ALDO)

$$r_{ALD} = \frac{\frac{V_{mf}^{ALD} C_{f16bp}^{c}}{K_{f16bp}^{ALD}} - \frac{V_{mr}^{ALD} C_{gap}^{c} C_{dhap}^{c}}{K_{gap}^{ALD} K_{i,dhap}^{ALD}}}{\left(1 + \frac{C_{2,3bpg}^{c}}{K_{i,2,3bpg}^{ALD}} + \frac{C_{f16bp}^{c}}{K_{f16bp}^{ALD}} + \frac{K_{dhap}^{ALD} C_{gap}^{c}}{K_{gap}^{ALD} K_{i,dhap}^{ALD}}\left(1 + \frac{C_{2,3bpg}^{c}}{K_{i,2,3bpg}^{ALD}}\right) + \frac{C_{dhap}^{c}}{K_{i,dhap}^{ALD}} + \frac{K_{dhap}^{ALD} C_{F1,6P}^{c} C_{gap}^{c}}{K_{i,f16bp}^{ALD} K_{gap}^{ALD} K_{i,dhap}^{ALD}} + \frac{C_{dhap}^{c} C_{gap}^{c}}{K_{gap}^{ALD} K_{i,dhap}^{ALD}}\right)}$$

$V_{mf}^{ALD} = 1.33*10^{2}\, mM\ h^{-1}$
$V_{mr}^{ALD} = 4.57*10^{2}\, mM\ h^{-1}$
$K_{f16bp}^{ALD} = 5*10^{-2}\, mM$
$K_{i,f16bp}^{ALD} = 1.98*10^{-2}\, mM$
$K_{dhap}^{ALD} = 3.5*10^{-2}\, mM$
$K_{i,dhap}^{ALD} = 1.1*10^{-2}\, mM$
$K_{gap}^{ALD} = 0.189 mM$
$K_{i,2,3bpg}^{ALD} = 1.5 mM$

Triose Phosphate Isomerase (TPI): The rate equation for TPI was taken from Mulquiney et al. [133]. The kinetic constants were adopted from previous literature [154, 163-165]. The rate kinetics of TPI follows a simple steady state uni uni reaction kinetics.

Equation S6. Triose Phosphate Isomerase (TPI)

$$r_{TPI} = \frac{V_{mf}^{TPI} \frac{C_{dhap}^{c}}{K_{f}^{TPI}} - V_{mr}^{TPI} \frac{C_{gap}^{c}}{K_{r}^{TPI}}}{1 + \frac{C_{dhap}^{c}}{K_{f}^{TPI}} + \frac{C_{gap}^{c}}{K_{r}^{TPI}}}$$

$V_{mf}^{TPI} = 5.10*10^{2}\, mM\ h^{-1}$
$V_{mr}^{TPI} = 2.76*10^{3}\, mM\ h^{-1}$
$K_{f}^{TPI} = 1.62*10^{-1}\, mM$
$K_{r}^{TPI} = 4.30*10^{-1}\, mM$

Glyceraldehyde 3-Phosphate Dehydrogenase (GAPDH): The rate equation for GAPDH was taken from Mulquiney et al. [133]. The kinetic constants were adopted from previous literature [166-169]. The rate kinetics of GAPDH follows the ter ter (bi uni uni bi ping pong) steady state kinetics.

Equation S7. Glyceraldehyde 3-Phosphate Dehydrogenase (GAPDH)

$$r_{GAPD} = \frac{V_{mf}^{GAPD}\frac{C_{NAD^+}^{c}C_{Pi}^{c}C_{gap}^{c}}{K_{NAD^+}^{GAPD}K_{i,Pi}^{GAPD}K_{i,gap}^{GAPD}} - V_{mr}^{GAPD}\frac{C_{1,3bpg}^{c}C_{NADH}^{c}C_{H^+}^{c}}{K_{i,1,3bpg}^{GAPD}K_{NADH}^{GAPD}}}{\begin{aligned}&\frac{C_{gap}^{c}}{K_{i,gap}^{GAPD}}\left(1+\frac{C_{gap}^{c}}{K_{i,gap}^{'GAPD}}\right)+\frac{C_{1,3bpg}^{c}}{K_{i,1,3bpg}^{GAPD}}\left(1+\frac{C_{gap}^{c}}{K_{i,GAP}^{'GAPD}}\right)+\frac{K_{1,3bpg}^{GAPD}C_{NADH}^{c}C_{H^+}^{c}}{K_{i,1,3bpg}^{GAPD}K_{NADH}^{GAPD}}+\frac{K_{gap}^{GAPD}C_{NAD^+}^{c}C_{Pi}^{c}}{K_{NAD^+}^{GAPD}K_{i,Pi}^{GAPD}K_{i,gap}^{GAPD}}\\&+\frac{C_{NAD^+}^{c}C_{gap}^{c}}{K_{i,NAD^+}^{GAPD}K_{i,gap}^{GAPD}}+\frac{C_{Pi}^{c}C_{gap}^{c}}{K_{i,Pi}^{GAPD}K_{i,gap}^{GAPD}}\left(1+\frac{C_{gap}^{c}}{K_{i,gap}^{'GAPD}}\right)+\frac{C_{NAD^+}^{c}C_{1,3bpg}^{c}}{K_{i,NAD^+}^{GAPD}K_{i,1,3bpg}^{GAPD}}+\frac{K_{1,3bpg}^{GAPD}C_{Pi}^{c}C_{NADH}^{c}C_{H^+}^{c}}{K_{i,Pi}^{GAPD}K_{i,1,3bpg}^{GAPD}K_{NADH}^{GAPD}}\\&+\frac{C_{gap}^{c}C_{NADH}^{c}C_{H^+}^{c}}{K_{i,gap}^{GAPD}K_{i,NADH}^{GAPD}}+\frac{C_{1,3bpg}^{c}C_{NADH}^{c}C_{H^+}^{c}}{K_{i,1,3bpg}^{GAPD}K_{NADH}^{GAPD}}+\frac{C_{NAD^+}^{c}C_{Pi}^{c}C_{gap}^{c}}{K_{NAD^+}^{GAPD}K_{i,Pi}^{GAPD}K_{i,gap}^{GAPD}}+\frac{K_{gap}^{GAPD}C_{NAD^+}^{c}C_{Pi}^{c}C_{1,3bpg}^{c}}{K_{i,gap}^{GAPD}K_{NAD^+}^{GAPD}K_{i,Pi}^{GAPD}K_{i,1,3bpg}^{'GAPD}}\\&+\frac{C_{Pi}^{c}C_{gap}^{c}C_{NADH}^{c}C_{H^+}^{c}}{K_{i,Pi}^{GAPD}K_{i,gap}^{GAPD}K_{i,NADH}^{GAPD}}+\frac{C_{Pi}^{c}C_{1,3bpg}^{c}C_{NADH}^{c}C_{H^+}^{c}}{K_{i,1,3bpg}^{GAPD}K_{NADH}^{GAPD}K_{i,Pi}^{GAPD}K_{i,1,3bpg}^{'GAPD}}\end{aligned}}$$

$V_{mf}^{GAPD} = 5.317*10^{3}\,mMh^{-1}$ $K_{gap}^{GAPD} = 0.095mM$

$V_{mr}^{GAPD} = 3.919*10^{3}\,mMh^{-1}$ $K_{i,gap}^{GAPD} = 1.59*10^{-16}\,mM$

$K_{NAD^+}^{GAPD} = 0.045mM$ $K_{i,gap}^{'GAPD} = 0.031mM$

$K_{i,NAD^+}^{GAPD} = 0.045mM$ $K_{1,3bpg}^{GAPD} = 0.000671mM$

$K_{Pi}^{GAPD} = 2.5mM$ $K_{i,1,3bpg}^{GAPD} = 1.52*10^{-18}\,mM$

$K_{i,Pi}^{GAPD} = 2.5mM$ $K_{i,1,3bpg}^{'GAPD} = 0.001mM$

$K_{NADH}^{GAPD} = 0.0033mM$ $K_{eq}^{GAPD} = 1.9*10^{-8}$

$K_{i,NADH}^{GAPD} = 0.01mM$

<u>Phosphoglycerate Kinase</u> (PGK): The rate equation for PGK was taken from Mulquiney et al. [133]. The kinetic constants were adopted from previous literature [170-173]. The rate kinetics of PGK follows the partial rapid equilibrium random bi bi steady state kinetics.

Equation S8. Phosphoglycerate Kinase (PGK)

$$r_{PGK} = \frac{V_{mf}^{PGK}\frac{C_{1,3bpg}^{c}C_{MgADP}^{c}}{K_{i,MgADP}^{PGK}K_{1,3bpg}^{PGK}} - V_{mr}^{PGK}\frac{C_{3\,pg}^{c}C_{MgATP}^{c}}{K_{i,MgATP}^{PGK}K_{3\,pg}^{PGK}}}{1+\frac{C_{1,3bpg}^{c}}{K_{i,1,3bpg}^{PGK}}+\frac{C_{MgADP}^{c}}{K_{i,MgADP}^{PGK}}+\frac{C_{1,3bpg}^{c}C_{MgADP}^{c}}{K_{i,MgADP}^{PGK}K_{1,3bpg}^{PGK}}+\frac{C_{3\,pg}^{c}}{K_{i,3\,pg}^{PGK}}+\frac{C_{MgATP}^{c}}{K_{i,MgATP}^{PGK}}+\frac{C_{3\,pg}^{c}C_{MgATP}^{c}}{K_{i,MgATP}^{PGK}K_{3\,pg}^{PGK}}}$$

$V_{mf}^{PGK} = 5.96*10^{4} mM/h$
$V_{mr}^{PGK} = 2.39*10^{4} mM/h$
$K_{MgADP}^{PGK} = 0.1mM$
$K_{i,MgADP}^{PGK} = 0.08mM$
$K_{1,3bpg}^{PGK} = 0.002mM$
$K_{i,1,3bpg}^{PGK} = 1.6mM$
$K_{MgATP}^{PGK} = 1mM$
$K_{i,MgATP}^{PGK} = 0.186mM$
$K_{3\,pg}^{PGK} = 1.1mM$
$K_{i,3\,pg}^{PGK} = 0.205mM$
$K_{eq}^{PGK} = 3.2*10^{3}$

Phosphoglycerate Mutase (PGM): The rate equation for PGM was taken from Mulquiney et al. [133]. The kinetic constants were adopted from previous literature [174, 175]. The rate kinetics of PGM follows the uni uni steady state kinetics.

Equation S9. Phosphoglycerate Mutase (PGM)

$$r_{PGAM} = \frac{V_{mf}^{PGAM}\frac{C_{3\,pg}^{c}}{K_{3\,pg}^{PGAM}} - V_{mr}^{PGAM}\frac{C_{2\,pg}^{c}}{K_{2\,pg}^{PGAM}}}{1+\frac{C_{3\,pg}^{c}}{K_{3\,pg}^{PGAM}}+\frac{C_{2\,pg}^{c}}{K_{2\,pg}^{PGAM}}}$$

$V_{mf}^{PGAM} = 4.894*10^{5} mM\ h^{-1}$
$V_{mr}^{PGAM} = 4.395*10^{5} mM\ h^{-1}$
$K_{3\,pg}^{PGAM} = 0.168mM$
$K_{2\,pg}^{PGAM} = 0.0256mM$
$K_{eq}^{PGAM} = 0.17$

Enolase (ENO): The rate equation for ENO was taken from Mulquiney et al. [133]. The kinetic constants were adopted from previous literature [176-178]. The rate kinetics of ENO follows the partial rapid equilibrium random bi bi steady state kinetics.

Equation S10. Enolase (ENO)

$$r_{ENO} = \frac{V_{mf}^{ENO}\frac{C_{2pg}^{c}C_{Mg^{2+}}^{c}}{K_{i,Mg^{2+}}^{ENO}K_{2pg}^{ENO}} - V_{mr}^{ENO}\frac{C_{pep}^{c}C_{Mg^{2+}}^{c}}{K_{i,Mg^{2+}}^{ENO}K_{pep}^{ENO}}}{1+\frac{C_{2pg}^{c}}{K_{i,2pg}^{ENO}}+\frac{C_{Mg^{2+}}^{c}}{K_{i,Mg^{2+}}^{ENO}}+\frac{C_{2pg}^{c}C_{Mg^{2+}}^{c}}{K_{i,Mg^{2+}}^{ENO}K_{2pg}^{ENO}}+\frac{C_{pep}^{c}}{K_{i,pep}^{ENO}}+\frac{C_{Mg^{2+}}^{c}}{K_{i,Mg^{2+}}^{ENO}}+\frac{C_{pep}^{c}C_{Mg^{2+}}^{c}}{K_{i,Mg^{2+}}^{ENO}K_{pep}^{ENO}}}$$

$$V_{mf}^{ENO} = 2.106*10^{4} mM\ h^{-1}$$
$$V_{mr}^{ENO} = 5.542*10^{3} mM\ h^{-1}$$
$$K_{i,Mg^{2+}}^{ENO} = K_{Mg^{2+}}^{ENO} = 0.14 mM$$
$$K_{pep}^{ENO} = K_{PEP}^{ENO} = 0.11 mM$$
$$K_{2pg}^{ENO} = K_{2PG}^{ENO} = .046 mM$$
$$K_{eq}^{ENO} = 3.0$$

Pyruvate Kinase (PK): The rate equation for PK was taken from Mulquiney et al. [133]. The kinetic constants were adopted from previous literature [179-184]. Like PFK, the rate kinetics of PK was based on the two-state allosteric model using the ordered bi bi mechanism. The two-state model considers that the enzyme can exist in the active or non-active state determined by the levels of the activity modulators. These include activators (*f16bp*, *pep*, *pyr* etc) and inhibitors (ATP, *ala* etc). The fraction of the enzyme in the active state is represented by the nonlinear term N_{PK} which is a function of levels of activity modulators. L_{PK} represents the equilibrium constant between enzymes at the two states in the absence of any substrates. The initial velocity expression for the enzyme fraction in the active state is modeled as partial rapid equilibrium random bi bi steady state equation.

Equation S11. Pyruvate Kinase (PK)

$$r_{PK} = \left(\frac{V_{mf}^{PK} \frac{C_{pep}^{c}}{K_{pep}^{PK}} \frac{C_{MgADP}^{c}}{K_{MgADP}^{PK}} - V_{mr}^{PK} \frac{C_{pyr}^{c}}{K_{pyr}^{PK}} \frac{C_{MgATP}^{c}}{K_{MgATP}^{PK}}}{\left(1+\frac{C_{pep}^{c}}{K_{pep}^{PK}}\right)\left(1+\frac{C_{MgADP}^{c}}{K_{MgADP}^{PK}}\right)+\left(1+\frac{C_{pyr}^{c}}{K_{pyr}^{PK}}\right)\left(1+\frac{C_{MgATP}^{c}}{K_{MgATP}^{PK}}\right)-1} \right) \frac{1}{N_{PK}}$$

$$N_{PK} = 1 + L_{PK} \frac{\left(1+\frac{C_{ATP}^{c}}{K_{ATP}^{PK}}\right)^{4}\left(1+\frac{C_{ala}^{c}}{K_{ala}^{PK}}\right)^{4}}{\left(1+\frac{C_{pep}^{c}}{K_{pep}^{PK}}+\frac{C_{pyr}^{c}}{K_{pyr}^{PK}}\right)^{4}\left(1+\frac{C_{f16bp}^{c}}{K_{f16bp}^{PK}}+\frac{C_{g16bp}^{c}}{K_{g16bp}^{PK}}\right)^{4}}$$

$V_{mf}^{PK} = 2.02*10^{3} mM\ h^{-1}$
$V_{mf}^{PK} = 4.75 mM\ h^{-1}$
$K_{pep}^{PK} = 2.25*10^{-1} mM$
$K_{MgADP}^{PK} = 4.74*10^{-1} mM$
$K_{MgATP}^{PK} = 3\ mM$
$K_{ATP}^{PK} = 3.39\ mM$
$K_{pyr}^{PK} = 4\ mM$
$K_{f16bp}^{PK} = 5.0*10^{-3} mM$
$K_{g16bp}^{PK} = 0.1\ mM$
$L_{PK} = 0.398$
$K_{ala}^{PK} = 0.02\ mM$

The rate equations and kinetic constants for pyruvate kinase isoforms. Isoform-specific parameters are colored blue.

$$r_{PK} = \left(\frac{V_{mf}^{PK} \frac{C_{pep}^{c}}{K_{pep}^{PK}} \frac{C_{MgADP}^{c}}{K_{MgADP}^{PK}} - V_{mr}^{PK} \frac{C_{pyr}^{c}}{K_{pyr}^{PK}} \frac{C_{MgATP}^{c}}{K_{MgATP}^{PK}}}{\left(1+\frac{C_{pep}^{c}}{K_{pep}^{PK}}\right)\left(1+\frac{C_{MgADP}^{c}}{K_{MgADP}^{PK}}\right)+\left(1+\frac{C_{pyr}^{c}}{K_{pyr}^{PK}}\right)\left(1+\frac{C_{MgATP}^{c}}{K_{MgATP}^{PK}}\right)-1} \right) \frac{1}{N_{PK}}$$

$$N_{PK} = 1 + L_{PK} \frac{\left(1+\frac{C_{ATP}^{c}}{K_{ATP}^{PK}}\right)^{4}\left(1+\frac{C_{ala}^{c}}{K_{ala}^{PK}}\right)^{4}}{\left(1+\frac{C_{pep}^{c}}{K_{pep}^{PK}}+\frac{C_{pyr}^{c}}{K_{pyr}^{PK}}\right)^{4}\left(1+\frac{C_{f16bp}^{c}}{K_{f16bp}^{PK}}+\frac{C_{g16bp}^{c}}{K_{g16bp}^{PK}}\right)^{4}}$$

$$r_{PK} = \sum_{i=1}^{4} \rho_{PK_i} r_{PK_i}$$

$V_{mf}^{PK} = 2.02*10^{3}\, mM\ \ h^{-1}$

$V_{mf}^{PK} = 4.75 mM\ \ h^{-1}$

$K_{pep}^{PK} = 2.25*10^{-1}\, mM$

$K_{MgADP}^{PK} = 4.74*10^{-1}\, mM$

$K_{MgATP}^{PK} = 3\ mM$

$K_{ATP}^{PK} = 3.39\ mM$

$K_{pyr}^{PK} = 4\ mM$

$K_{f16bp}^{PK} = 5.0*10^{-3}\, mM$

$K_{g16bp}^{PK} = 0.1\ mM$

$L_{PK} = 0.398$

$K_{ala}^{PK} = 0.02\ mM$

	$K_{pep}^{PK}[185]$	$K_{ATP}^{PK}[185]$	$K_{f16bp}^{PK}[185]$
PKM2	0.4	2.5	0.25
PKM1	0.08	3.25	N.A.
PKL	0.6	0.125	0.08
PKR	1.2	0.05	0.4

	ρ_{PK_i}			
	D6	D10	D14	D20
PKM1	0.46	0.24	0.29	0.51
PKM2	0.46	0.24	0.29	0.51
PKL	0.08	0.09	0.09	0.08
PKR	0.08	0.09	0.09	0.08

Lactate Dehydrogenase (LDH): The rate equation for LDH and the kinetic constants were adopted from previous literature [133, 186-188]. The kinetics of LDH was modeled as ordered bi bi steady state kinetics, with substrate inhibition by pyruvate.

Equation S12. Lactate Dehydrogenase (LDH)

$$r_{LDH}=\frac{V_{mf}^{LDH}\frac{C_{NADH}^{c}C_{pyr}^{c}}{K_{i,NADH}^{LDH}K_{pyr}^{LDH}}-V_{mr}^{LDH}\frac{C_{NAD}^{c}C_{lac}^{c}}{K_{i,NAD}^{LDH}K_{lac}^{LDH}}}{\left(1+\frac{K_{NADH}^{LDH}C_{pyr}^{c}}{K_{i,NADH}^{LDH}K_{pyr}^{LDH}}+\frac{K_{NAD}^{LDH}C_{lac}^{c}}{K_{i,NAD}^{LDH}K_{lac}^{LDH}}\right)\left(1+\frac{C_{pyr}^{c}}{K_{i,pyr}^{"LDH}}\right)+\frac{C_{NADH}^{c}}{K_{i,NADH}^{LDH}}+\frac{C_{NAD}^{c}}{K_{i,NAD}^{LDH}}}$$
$$+\frac{C_{NADH}^{c}C_{pyr}^{c}}{K_{i,NADH}^{LDH}K_{pyr}^{LDH}}+\frac{K_{NAD}^{LDH}C_{NADH}^{c}C_{lac}^{c}}{K_{i,NAD}^{LDH}K_{i,NADH}^{LDH}K_{lac}^{LDH}}+\frac{K_{NADH}^{LDH}C_{NAD}^{c}C_{pyr}^{c}}{K_{i,NAD}^{LDH}K_{i,NADH}^{LDH}K_{pyr}^{LDH}}+\frac{C_{NAD}^{c}C_{lac}^{c}}{K_{i,NAD}^{LDH}K_{lac}^{LDH}}$$
$$+\frac{C_{NADH}^{c}C_{pyr}^{c}C_{lac}^{c}}{K_{i,NADH}^{LDH}K_{pyr}^{LDH}K_{i,lac}^{LDH}}+\frac{C_{NAD}^{c}C_{pyr}^{c}C_{lac}^{c}}{K_{i,NAD}^{LDH}K_{i,pyr}^{LDH}K_{lac}^{LDH}}$$

$V_{mf}^{LDH}=8.66*10^{2}\,mM\ h^{-1}$
$V_{mr}^{LDH}=2.17*10^{2}\,mM\ h^{-1}$
$K_{pyr}^{LDH}=0.2\ mM$
$K_{i,pyr}^{LDH}=0.228\ mM$
$K_{NAD}^{LDH}=0.107\ mM$
$K_{i,NAD}^{LDH}=0.503\ mM$
$K_{lac}^{LDH}=10.1\ mM$
$K_{i,lac}^{LDH}=30\ mM$
$K_{i,NADH}^{LDH}=2.45*10^{-3}\ mM$
$K_{NADH}^{LDH}=8.44*10^{-3}\ mM$
$K_{i,pyr}^{"LDH}=0.101\ mM$

The rate equations and kinetic constants for lactate dehydrogenase isoforms. Isoform-specific parameters are colored blue.

$$r_{LDH}=\frac{V_{mf}^{LDH}\frac{C_{NADH}^{c}C_{pyr}^{c}}{K_{i,NADH}^{LDH}K_{pyr}^{LDH}}-V_{mr}^{LDH}\frac{C_{NAD}^{c}C_{lac}^{c}}{K_{i,NAD}^{LDH}K_{lac}^{LDH}}}{\left(1+\frac{K_{NADH}^{LDH}C_{pyr}^{c}}{K_{i,NADH}^{LDH}K_{pyr}^{LDH}}+\frac{K_{NAD}^{LDH}C_{lac}^{c}}{K_{i,NAD}^{LDH}K_{lac}^{LDH}}\right)\left(1+\frac{C_{pyr}^{c}}{K_{i,pyr}^{"LDH}}\right)+\frac{C_{NADH}^{c}}{K_{i,NADH}^{LDH}}+\frac{C_{NAD}^{c}}{K_{i,NAD}^{LDH}}}$$
$$+\frac{C_{NADH}^{c}C_{pyr}^{c}}{K_{i,NADH}^{LDH}K_{pyr}^{LDH}}+\frac{K_{NAD}^{LDH}C_{NADH}^{c}C_{lac}^{c}}{K_{i,NAD}^{LDH}K_{i,NADH}^{LDH}K_{lac}^{LDH}}+\frac{K_{NADH}^{LDH}C_{NAD}^{c}C_{pyr}^{c}}{K_{i,NAD}^{LDH}K_{i,NADH}^{LDH}K_{pyr}^{LDH}}+\frac{C_{NAD}^{c}C_{lac}^{c}}{K_{i,NAD}^{LDH}K_{lac}^{LDH}}$$
$$+\frac{C_{NADH}^{c}C_{pyr}^{c}C_{lac}^{c}}{K_{i,NADH}^{LDH}K_{pyr}^{LDH}K_{i,lac}^{LDH}}+\frac{C_{NAD}^{c}C_{pyr}^{c}C_{lac}^{c}}{K_{i,NAD}^{LDH}K_{i,pyr}^{LDH}K_{lac}^{LDH}}$$

$V_{mf}^{LDH}=8.66*10^{2}\,mM\ h^{-1}$
$V_{mr}^{LDH}=2.17*10^{2}\,mM\ h^{-1}$
$K_{i,NADH}^{LDH}=2.45*10^{-3}\ mM$
$K_{i,pyr}^{"LDH}=0.101\,mM$
$r_{LDH}=\sum_{i=1}^{3}\rho_{LDH_i}r_{LDH_i}$

	K_{pyr}^{LDH}	$K_{i,pyr}^{LDH}$	K_{lac}^{LDH}	$K_{i,lac}^{LDH}$	K_{NAD}^{LDH}	$K_{i,NAD}^{LDH}$	K_{NADH}^{LDH}
LDH-A4 (LDH-5) [189, 190]	0.35	0.280	23	130	0.085	0.467	0.00743
LDH-B4 (LDH-1) [191]	0.1	0.180	9.340	26	0.169	0.5028	0.00844

	ρ_{LDH_i}			
	D6	D10	D14	D20
LDHA	0.51	0.17	0.20	0.65
LDHB	0.48	0.50	0.41	0.47

PENTOSE PHOSPHATE PATHWAY

<u>Glucose 6-phosphate Dehydrogenase</u> (G6PD)

G6PD is part of oxidative pentose phosphate pathway. Kinetics of G6PD was modeled as ordered bi bi steady state kinetics [192]. The rate equation for G6PD was taken from [193]. The kinetic constants were adopted from previous literature [194, 195].

Equation S13. Glucose 6-phosphate Dehydrogenase (G6PD)

$$r_{G6PD}=\frac{V_{mf}^{G6PD}C_{NADP}^{c}C_{g6p}^{c}-V_{mr}^{G6PD}C_{6pg}^{c}C_{NADPH}^{c}}{D_{G6PD}}$$

$$V_{mf}^{G6PD}=4.39*10^{20}\,mM^{-1}h^{-1}$$

$$V_{mr}^{G6PD}=7.48*10^{19}\,mM^{-1}h^{-1}$$

$$D_{G6PD}=1.45*10^{15}+2.04*10^{20}C_{NADPH}^{c}+1.83*10^{20}C_{NADP}^{c}+$$
$$C_{g6p}^{c}\left(4.29*10^{19}+6.01*10^{24}C_{NADPH}^{c}+6.84*10^{24}C_{NADP}^{c}\right)+$$
$$C_{6pg}^{c}\left(5.74*10^{17}+5.01*10^{24}C_{NADPH}^{c}+7.26*10^{22}C_{NADP}^{c}+C_{g6p}^{c}\left(1.10*10^{29}C_{NADPH}^{c}+8.65*10^{27}C_{NADP}^{c}\right)\right)$$

<u>6-Phosphogluconate Dehydrogenase</u> (6PGD):

6PGD is part of oxidative pentose phosphate pathway. Kinetics of 6PGD was modeled as ordered sequential bi ter steady state kinetics [196]. The rate equation for 6PGD was taken from [193]. The kinetic constants were adopted from previous literature [197, 198].

Equation S14. 6-Phosphogluconate Dehydrogenase (6PGD)

$$r_{6PGD}=\frac{V_{mf}^{6PGD}C_{NADP}^{c}C_{6pg}^{c}-V_{mr}^{6PGD}C_{ru5p}^{c}C_{NADPH}^{c}CO_{2}}{D_{6PGD}}$$

$$V_{mf}^{6PGD}=1.83*10^{19}\,mM^{-1}h^{-1}$$

$$V_{mr}^{6PGD}=9.0*10^{19}\,mM^{-2}h^{-1}$$

$$D_{6PGD}=5.38*10^{15}+7.86*10^{19}C_{NADPH}^{c}+6.97*10^{18}C_{NADP}^{c}+$$
$$C_{ru5p}^{c}\left(1.04*10^{18}+3.99*10^{23}C_{NADPH}^{c}+3.03*10^{21}C_{NADP}^{c}\right)+$$
$$C_{6pg}^{c}\left(7.26*10^{18}+2.40*10^{23}C_{NADPH}^{c}+4.46*10^{23}C_{NADP}^{c}+C_{ru5p}^{c}\left(2.63*10^{27}C_{NADPH}^{c}+3.19*10^{27}C_{NADP}^{c}\right)\right)$$

Ribulose Phosphate Epimerase (RPE)

RPE is part of non-oxidative pentose phosphate pathway. Kinetics of RPE was modeled as steady state uni uni mechanism. The kinetic constants were adopted from previous literature [199-202].

Equation S15. Ribulose Phosphate Epimerase (RPE)

$$r_{RPE} = \frac{V_{mf}^{RPE}\frac{C_{ru5p}^{c}}{K_{f}^{RPE}} - V_{mr}^{RPE}\frac{C_{xyl5p}^{c}}{K_{r}^{RPE}}}{1 + \frac{C_{ru5p}^{c}}{K_{f}^{RPE}} + \frac{C_{xyl5p}^{c}}{K_{r}^{RPE}}}$$

$$V_{mf}^{RPE} = 4.642 * 10^{4}\, mM\ h^{-1}$$
$$V_{mr}^{RPE} = 6.667 * 10^{4}\, mM\ h^{-1}$$
$$K_{f}^{RPE} = 1.90 * 10^{-1}\, mM$$
$$K_{r}^{RPE} = 5.00 * 10^{-1}\, mM$$

Ribose Phosphate Isomerase (RPI)

RPI is part of non-oxidative pentose phosphate pathway. Kinetics of RPI was modeled as steady state uni uni mechanism. The kinetic constants were adopted from previous literature [199, 200, 203, 204].

Equation S16. Ribose Phosphate Isomerase (RPI)

$$r_{RPI} = \frac{V_{mf}^{RPI}\frac{C_{ru5p}^{c}}{K_{f}^{RPI}} - V_{mr}^{RPI}\frac{C_{r5p}^{c}}{K_{r}^{RPI}}}{1 + \frac{C_{ru5p}^{c}}{K_{f}^{RPI}} + \frac{C_{r5p}^{c}}{K_{r}^{RPI}}}$$

$$V_{mf}^{RPI} = 2.56 * 10^{4}\, mM\ h^{-1}$$
$$V_{mr}^{RPI} = 1.09 * 10^{4}\, mM\ h^{-1}$$
$$K_{f}^{RPI} = 7.80 * 10^{-1}\, mM$$
$$K_{r}^{RPI} = 2.20\ mM$$

Phosphoribosylpyrophosphate Synthetase (PRPPS)

PRPPS channels ribose-5-phosphate (*r5p*) towards nucleotide synthesis. The rate is a relatively small portion of total PPP flux. Kinetics of PRPPS was modeled as a rapid equilibrium random bi reactant system. The kinetic constants were adopted from previous literature [205].

Equation S17. Phosphoribosylpyrophosphate Synthetase (PRPPS)

$$r_{PRPPS} = V_m^{PRPPS} \frac{C^c_{MgATP} C^c_{r5p}}{\left(K^{PRPPS}_{MgATP} + C^c_{MgATP}\right)\left(K^{PRPPS}_{r5p} + C^c_{r5p}\right)}$$

$V_m^{PRPPS} = 25.3\ mM\ h^{-1}$
$K^{PRPPS}_{MgATP} = 0.01\ mM$
$K^{PRPPS}_{r5p} = 0.57\ mM$

Transketolase1 (TK1)

TK1 is part of non-oxidative pentose phosphate pathway. Kinetics of TK1 was modeled as steady state bi bi ping pong mechanism. The kinetic constants were adopted from previous literature [199, 200, 206].

Equation S18. Transketolase1 (TK1)

$$r_{TK1} = \frac{V^{TK1}_{mf} C^c_{xyl5p} C^c_{r5p} - V^{TK1}_{mr} C^c_{s7p} C^c_{gap}}{D_{TK1}}$$

$$D_{TK1} = 2.63*10^{16} C^c_{s7p} + C^c_{r5p}\left(4.40*10^{16} + 4.92*10^{16} C^c_{s7p}\right) + 5.96*10^{16} C^c_{gap} + 6.94*10^{16} C^c_{s7p} C^c_{gap} + C^c_{xyl5P}\left(7.35*10^{16} + 2.44*10^{17} C^c_{r5p} + 3.38*10^{17} C^c_{gap}\right)$$

$V^{TK1}_{mf} = 5.3210^{18}\ mM^{-1}h^{-1}$
$V^{TK1}_{mr} = 2.58*10^{18}\ mM^{-1}h^{-1}$

Transaldolase (TA)

TA is part of non-oxidative pentose phosphate pathway. Kinetics of TA was modeled as steady state bi bi ping pong mechanism. The rate equation for TA was taken from [199]. The kinetic constants were adopted from previous literature [200, 207-209].

Equation S19. Transaldolase (TA)

$$r_{TA} = \frac{V^{TA}_{mf} C^c_{s7p} C^c_{gap} - V^{TA}_{mr} C^c_{f6p} C^c_{e4p}}{D_{TA}}$$

$$D_{TA} = 3.4*10^{16} C^c_{s7p} + 2.38*10^{16} C^c_{gap} + 1.64*10^{17} C^c_{e4p} + 2.72*10^{15} C^c_{f6p} + 4.41*10^{17} C^c_{s7p} C^c_{gap} + 7.83*10^{16} C^c_{e4p} C^c_{F6P} + 2.21*10^{16} C^c_{gap} C^c_{f6p} + 2.1*10^{18} C^c_{s7p} C^c_{e4p}$$

$V^{TA}_{mf} = 1.36*10^{20}\ mM^{-1}h^{-1}$
$V^{TA}_{mr} = 7.53*10^{19}\ mM^{-1}h^{-1}$

Transketolase2 (TK2)

TK2 is part of non-oxidative pentose phosphate pathway. Kinetics of TK2 was modeled as steady state bi bi ping pong mechanism. The kinetic constants were adopted from previous literature [199, 200, 206, 210].

Equation S20. Transketolase2 (TK2)

$$r_{TK2}=\frac{V_{mf}^{TK2}C_{xyl5p}^{c}C_{e4p}^{c}-V_{mr}^{TK2}C_{f6p}^{c}C_{gap}^{c}}{D_{TK2}}$$

$$D_{TK2}=\left(3.01*10^{17}C_{e4p}^{c}+5.96*10^{16}C_{gap}^{c}+C_{f6p}^{c}\left(1.25*10^{16}+1.60*10^{17}C_{e4p}^{c}+3.31*10^{16}C_{gap}^{c}\right)\right)+$$
$$C_{xyl5p}^{c}\left(7.35*10^{16}+1.67*10^{18}C_{e4p}^{c}+3.38*10^{17}C_{gap}^{c}\right)$$

$$V_{mf}^{TK2}=3.64*10^{19}\,mM^{-1}h^{-1}$$
$$V_{mr}^{TK2}=1.23*10^{18}\,mM^{-1}h^{-1}$$

Glutathione Peroxidase (GPX)

GPX oxidizes the reduced form of glutathione (*gsh*) into glutathione disulfide (*gssg*) while hydrogen peroxide (H_2O_2) is reduced into the water. Thus this reaction plays an important role in preventing cells from oxidative stress. The kinetics of GPX was modeled as first-order reaction kinetics.

Equation S21. Glutathione Peroxidase (GPX)

$$r_{GPX}=V_{f}^{GPX}C_{gsh}^{c}$$

$$V_{f}^{GPX}=1.56*10^{4}\,mM^{-1}h^{-1}$$

Glutathione Reductase (GSSGR)

The enzyme GSSGR converts *gssg* back into *gsh* while NADPH produced in the pentose phosphate pathway is oxidized into NADP. The kinetics of GSSGR was modeled as ordered sequential steady state kinetics [211]. The rate equation for GSSGR was taken from [193]. The kinetic constants were adopted from previous literature [212, 213].

Equation S22. Glutathione Reductase (GSSGR)

$$r_{GSSGR}=\frac{V_{mf}^{GSSGR}C_{NADPH}^{c}C_{gssg}^{c}-V_{mr}^{GSSGR}C_{gsh}^{c}C_{NADP}^{c}}{D_{GSSGR}}$$

$$V_{mf}^{GSSGR}=5.5*10^{44}\,mM^{-1}h^{-1}$$

$$V_{mr}^{GSSGR}=1.05*10^{40}\,mM^{-1}h^{-1}$$

$$D_{GSSGR}=1.73*10^{40}+2.88*10^{42}C_{NADPH}^{c}+3.43*10^{41}C_{gssg}^{c}+7.77*10^{35}C_{gsh}^{c}+2.47*10^{41}C_{NADP}^{c}$$
$$+4.02*10^{43}C_{NADPH}^{c}C_{gssg}^{c}+1.3*10^{38}C_{NADPH}^{c}C_{gsh}^{c}+4.90*10^{42}C_{gssg}^{c}C_{NADP}^{c}+5.55*10^{36}C_{gsh}^{c}C_{gsh}^{c}$$
$$+1.11*10^{37}C_{gsh}^{c}C_{NADP}^{c}+1.24*10^{40}C_{gsh}^{c}C_{NADP}^{c}+3.26*10^{39}C_{NADPH}^{c}C_{gssg}^{c}C_{gsh}^{c}$$
$$+2.08*10^{41}C_{NADPH}^{c}C_{gssg}^{c}C_{gsh}^{c}+9.25*10^{38}C_{NADPH}^{c}C_{gsh}^{c}C_{gsh}^{c}+2.45*10^{41}C_{gssg}^{c}C_{gsh}^{c}C_{NADP}^{c}$$
$$+1.78*10^{39}C_{gsh}^{c}C_{gsh}^{c}C_{NADP}^{c}+2.32*10^{40}C_{NADPH}^{c}C_{gssg}^{c}C_{gsh}^{c}C_{gsh}^{c}+2.74*10^{40}C_{gssg}^{c}C_{gsh}^{c}C_{NADP}^{c}C_{gsh}^{c}$$

TCA CYCLE

<u>Pyruvate Dehydrogenase</u> (PDH)

The rate equation for PDH was taken from [214]. The kinetics of PDH was modeled as hexa uni ping pong mechanism. The kinetic constants were adopted from previous literature [215, 216].

Equation S23. Pyruvate Dehydrogenase (PDH)

$$r_{PDH}=\frac{V_{f,PDH}\left(C_{pyr}^{m}C_{CoASH}^{m}C_{NAD^{+}}^{m}-\frac{C_{AcCoA}^{m}C_{NADH}^{m}C_{CO_2}^{m}}{K_{eq,PDH}}\right)}{K_{NAD^{+}}^{PDH}\alpha_{PDH,i2}C_{pyr}^{m}C_{CoASH}^{m}+K_{CoASH}^{PHD}\alpha_{PDH,i1}C_{pyr}^{m}C_{NAD^{+}}^{m}+K_{pyr}^{PDH}C_{CoASH}^{m}C_{NAD^{+}}^{m}+C_{pyr}^{m}C_{CoASH}^{m}C_{NAD^{+}}^{m}}$$

$$\alpha_{PDH,i1}=\left(1+\frac{C_{AcCoA}^{m}}{K_{i,AcCoA}^{c}}\right)$$

$$\alpha_{PDH,i2}=\left(1+\frac{C_{NADH}^{m}}{K_{i,NADH}^{PDH}}\right)$$

$$V_{f,PDH}=189.7\,mMh^{-1}$$
$$K_{eq,PDH}=1.2*10^{4}$$
$$K_{pyr}^{PDH}=38.8*10^{-3}\,mM$$
$$K_{CoASH}^{PDH}=9.9*10^{-3}\,mM$$
$$K_{NAD^{+}}^{PDH}=60.7*10^{-3}\,mM$$
$$K_{i,AcCoA}^{PDH}=40.0*10^{-3}\,mM$$
$$K_{i,NADH}^{PDH}=40.2*10^{-3}\,mM$$

<u>Citrate Synthase</u> (CS)

The rate equation for CS was taken from [214]. The kinetic constants were adopted from previous literature [217-220]. The kinetics of CS was modeled as an ordered bi bi mechanism.

Equation S24. Citrate Synthase (CS)

$$r_{CS} = \frac{V_{f,CS}\left(C^m_{OAA}C^m_{AcCoA} - \frac{C^m_{CoASH}C^m_{cit}}{K_{eq,CS}}\right)}{K^{CS}_{i,OAA}K^{CS}_{i,AcCoA}\alpha_{CS,i1} + K^{CS}_{OAA}\alpha_{CS,i1}C^m_{AcCoA} + K^{CS}_{AcCoA}\alpha_{CS,i2}C^m_{OAA} + C^m_{OAA}C^m_{AcCoA}}$$

$$\alpha_{CS,i1} = \left(1 + \frac{C^m_{cit} \diagup P_{cit}}{K^{CS}_{i,cit}}\right)$$

$$\alpha_{CS,i2} = \left(1 + \frac{C^m_{ATP} \diagup P_{ATP}}{K^{CS}_{i,ATP}} + \frac{C^m_{ADP} \diagup P_{ADP}}{K^{CS}_{i,ADP}} + \frac{C^m_{AMP} \diagup P_{AMP}}{K^{CS}_{i,AMP}} + \frac{C^m_{CoASH}}{K^{CS}_{i,CoASH}} + \frac{C^m_{scoa}}{K^{CS}_{i,scoA}}\right)$$

$V_{f,CS} = 1804\ mMh^{-1}$
$K^0_{eq,CS} = 6.22*10^{12}$
$K^{CS}_{OAA} = 4*10^{-3}mM$
$K^{CS}_{AcCoA} = 1.4*10^{-3}mM$
$K^{CS}_{i,OAA} = 3.33*10^{-3}mM$
$K^{CS}_{i,cit} = 1600*10^{-3}mM$
$K^{CS}_{i,ATP} = 900*10^{-3}mM$
$K^{CS}_{i,ADP} = 1800*10^{-3}mM$
$K^{CS}_{i,AMP} = 6000*10^{-3}mM$
$K^{CS}_{i,CoASH} = 67*10^{-3}mM$
$K^{CS}_{i,scoa} = 140*10^{-3}mM$

Aconitase (ACON)

The rate equation for ACON was taken from [214]. The kinetics of ACON employs the steady state uni uni reaction kinetics. The kinetic constants were adopted from previous literature [217, 218, 221].

Equation S25. Aconitase (ACON)

$$r_{ACON} = \frac{V_{f,ACON}\left(C^m_{cit} - \frac{C^m_{icit}}{K_{eq,ACON}}\right)}{K^{ACON}_{cit} + C^m_{cit} + \frac{K^{ACON}_{cit}C^m_{icit}}{K^{ACON}_{icit}}}$$

$V_{f,ACON} = 1*10^5 mMh^{-1}$
$K_{eq,ACON} = 2.7*10^{-2}$
$K^{ACON}_{cit} = 1161*10^{-3}mM$
$K^{ACON}_{icit} = 434*10^{-3}mM$

\

Isocitrate Dehydrogenase (IDH)

The rate equation for IDH was taken from [214]. The kinetics of IDH was modeled as ordered bi ter mechanism. The kinetic constants were adopted from previous literature [217, 218, 222, 223].

Equation S26. Isocitrate Dehydrogenase (IDH)

$$r_{IDH} = \frac{V_{f,IDH}\left(1-\frac{1}{K_{eq,IDH}}\frac{C^m_{akg}C^m_{NADH}C^m_{CO_2}}{C^m_{NAD^+}C^m_{icit}}\right)}{1+\left(\frac{K^{IDH}_{m,icit}}{C^m_{icit}}\right)^{n_H}\alpha_{IDH,i1}+\frac{K^{IDH}_{m,NAD^+}}{C^m_{NAD^+}}\left(1+\left(\frac{K^{IDH}_{i,icit}}{C^m_{icit}}\right)^{n_H}\alpha_{IDH,i1}+\frac{C^m_{NADH}}{K^{IDH}_{i,NADH}}\alpha_{IDH,i1}\right)}$$

$$\alpha_{IDH,i1} = \left(1+\frac{K^{IDH}_{a,ADP}P_{ADP}}{C^m_{ADP}P_{fADP}}\left(1+\frac{C^m_{ATP}P_{fATP}}{K^{IDH}_{i,ATP}P_{ATP}}\right)\right)$$

$V_{f,AKG} = 2.75*10^4\ mMh^{-1}$
$K_{eq,IDH} = 30.5$
$K^{IDH}_{m,NAD^+} = 74*10^{-3}\ mM$
$K^{IDH}_{m,icit} = 183*10^{-3}\ mM$
$K^{IDH}_{a,ADP} = 50*10^{-3}\ mM$
$K^{IDH}_{i,ATP} = 91*10^{-3}\ mM$
$K^{IDH}_{i,icit} = 23.8*10^{-3}\ mM$
$K^{IDH}_{i,NADH} = 29*10^{-3}\ mM$
$n_H = 3$

α-Ketoglutarate Dehydrogenase (AKGD)

The rate equation for AKGD was taken from [214]. The kinetics of AKGD was modeled as hexa uni ping pong ter ter mechanism. The kinetic constants were adopted from previous literature [217, 218, 224, 225].

Equation S27. α-Ketoglutarate Dehydrogenase (AKGD)

$$r_{AKGD} = \frac{V_{f,AKGD}\left(1-\frac{1}{K_{eq,AKGD}}\frac{C^m_{SCoA}C^m_{NADH}C^m_{CO_2}}{C^m_{akg}C^m_{CoASH}C^m_{NAD^+}}\right)}{1+\left(\frac{K^{AKGD}_{m,akg}}{C^m_{akg}}\right)\alpha_{AKGD,i1}+\frac{K^{AKGD}_{m,CoASH}}{C^m_{CoASH}}\left(1+\frac{C^m_{SCoA}}{K^{AKGD}_{i,SCoA}}\right)+\frac{K^{AKGD}_{m,NAD^+}}{C^m_{NAD^+}}\left(1+\frac{C^m_{NADH}}{K^{AKGD}_{i,NADH}}\right)}$$

$$\alpha_{AKGD,i1} = \left(1+\frac{K^{AKGD}_{a,ADP}P_{ADP}}{C^m_{ADP}P_{fADP}}\left(1+\frac{C^m_{ATP}P_{fATP}}{K^{AKGD}_{i,ATP}P_{ATP}}\right)\right)$$

$V_{f,AKGD} = 2495\ mMh^{-1}$
$K_{eq,AKGD} = 1.66*10^{8}$
$K^{AKGD}_{m,akg} = 120*10^{-3}mM$
$K^{AKGD}_{m,CoaSH} = 55*10^{-3}mM$
$K^{AKGD}_{m,NAD^+} = 21*10^{-3}mM$
$K^{AKGD}_{a,ADP} = 100*10^{-3}mM$
$K^{AKGD}_{i,ATP} = 50*10^{-3}mM$
$K^{AKGD}_{i,SCoA} = 6.9*10^{-3}mM$
$K^{AKGD}_{i,NADH} = 0.60*10^{-3}mM$

Succinyl-CoA Synthetase (SCOAS)

The rate equation for SCOAS was taken from [214]. The kinetics of SCOAS follows the ordered ter ter mechanism. The kinetic constants were adopted from previous literature [217, 218, 226].

Equation S28. Succinyl-CoA Synthetase (SCOAS)

$$r_{SCoAS} = \frac{V_{f,SCoAS}\left(C^m_{GDP}C^m_{SCoA}C^m_{Pi} - \frac{C^m_{CoASH}C^m_{suc}C^m_{GTP}}{K_{eq,SCoAS}}\right)}{K^{SCoAS}_{i,GDP}K^{SCoAS}_{i,SCoA}K^{SCoAS}_{m,Pi} + K^{SCoAS}_{i,SCoA}K^{SCoAS}_{m,Pi}C^m_{GDP} + K^{SCoAS}_{i,GDP}K^{SCoAS}_{m,SCoA}C^m_{Pi} + K^{SCoAS}_{m,Pi}C^m_{GDP}C^m_{SCoA} + K^{SCoAS}_{m,SCoA}C^m_{GDP}C^m_{Pi}$$
$$K^{SCoAS}_{m,GDP}C^m_{SCoA}C^m_{Pi} + C^m_{GDP}C^m_{SCoA}C^m_{Pi} + \left(\frac{K^{SCoAS}_{i,GDP}K^{SCoAS}_{i,SCoA}K^{SCoAS}_{m,Pi}}{K^{SCoAS}_{i,suc}K^{SCoAS}_{i,GTP}K^{SCoAS}_{m,CoASH}}\right)\left(K^{SCoAS}_{i,GTP}K^{SCoAS}_{m,suc}C^m_{CoASH} + K^{SCoAS}_{i,suc}K^{SCoAS}_{m,CoASH}C^m_{GTP} + \right.$$
$$K^{SCoAS}_{m,GTP}C^m_{CoASH}C^m_{suc} + K^{SCoAS}_{m,suc}C^m_{CoASH}C^m_{GTP} + K^{SCoAS}_{m,CoASH}C^m_{suc}C^m_{GTP} + C^m_{CoASH}C^m_{suc}C^m_{GTP} + \frac{K^{SCoAS}_{m,suc}K^{SCoAS}_{i,GTP}C^m_{GDP}C^m_{SCoA}C^m_{suc}}{K^{SCoAS}_{i,GDP}K^{SCoAS}_{i,SCoA}}$$
$$+\frac{K^{SCoAS}_{m,GTP}C^m_{GDP}C^m_{CoASH}C^m_{suc}}{K^{SCoAS}_{i,GDP}} + \frac{K^{SCoAS}_{i,GTP}K^{SCoAS}_{m,suc}C^m_{GDP}C^m_{SCoA}C^m_{Pi}C^m_{CoASH}}{K^{SCoAS}_{i,GDP}K^{SCoAS}_{i,SCoA}K^{SCoAS}_{i,Pi}} + \frac{K^{SCoAS}_{m,suc}K^{SCoAS}_{i,GTP}C^m_{GDP}C^m_{CoASH}}{K^{SCoAS}_{i,GDP}}$$
$$\left.+\frac{K^{SCoAS}_{i,CoASH}K^{SCoAS}_{m,GTP}C^m_{GDP}C^m_{SCoA}C^m_{Pi}C^m_{suc}}{K^{SCoAS}_{i,GDP}K^{SCoAS}_{i,SCoA}K^{SCoAS}_{i,Pi}} + \frac{K^{SCoAS}_{m,GTP}C^m_{GDP}C^m_{SCoA}C^m_{CoASH}C^m_{suc}}{K^{SCoAS}_{i,GDP}K^{SCoAS}_{i,SCoA}} + \frac{K^{SCoAS}_{m,GTP}C^m_{GDP}C^m_{SCoA}C^m_{Pi}C^m_{CoASH}C^m_{suc}}{K^{SCoAS}_{i,GDP}K^{SCoAS}_{i,SCoA}K^{SCoAS}_{i,Pi}}\right)$$
$$+\frac{K^{SCoAS}_{i,GDP}K^{SCoAS}_{m,SCoA}C^m_{Pi}C^m_{suc}C^m_{GTP}}{K^{SCoAS}_{i,suc}K^{SCoAS}_{i,GTP}} + \frac{K^{SCoAS}_{m,GDP}K^{SCoAS}_{i,Pi}C^m_{SCoA}C^m_{CoASH}C^m_{suc}C^m_{GTP}}{K^{SCoAS}_{i,CoASH}K^{SCoAS}_{i,suc}K^{SCoAS}_{i,GTP}} + \frac{K^{SCoAS}_{i,GDP}K^{SCoAS}_{m,SCoA}C^m_{Pi}C^m_{CoASH}C^m_{suc}C^m_{GTP}}{K^{SCoAS}_{i,CoASH}K^{SCoAS}_{i,suc}K^{SCoAS}_{i,GTP}} +$$
$$+\frac{K^{SCoAS}_{m,GDP}C^m_{SCoA}C^m_{Pi}C^m_{GTP}}{K^{SCoAS}_{i,GTP}} + \frac{K^{SCoAS}_{i,GDP}K^{SCoAS}_{m,SCoA}C^m_{Pi}C^m_{GTP}}{K^{SCoAS}_{i,GTP}} + \frac{K^{SCoAS}_{m,GDP}C^m_{SCoA}C^m_{Pi}C^m_{suc}C^m_{GTP}}{K^{SCoAS}_{i,suc}K^{SCoAS}_{i,GTP}} + \frac{K^{SCoAS}_{m,GDP}C^m_{SCoA}C^m_{Pi}C^m_{CoASH}C^m_{suc}C^m_{GTP}}{K^{SCoAS}_{i,GDP}K^{SCoAS}_{i,SCoA}K^{SCoAS}_{i,Pi}}$$

$V_{f,SCoAS} = 362\ mMh^{-1}$ $\quad$ $K^{SCoAS}_{m,GTP} = 11.1*10^{-3}\ mM$

$K_{eq,SCOAS} = 7.43$ $\quad$ $K^{SCoAS}_{i,GDP} = 5.5*10^{-3}\ mM$

$K^{SCoAS}_{m,GDP} = 16*10^{-3}\ mM$ $\quad$ $K^{SCoAS}_{i,SCoA} = 100*10^{-3}\ mM$

$K^{SCoAS}_{m,SCoA} = 55*10^{-3}\ mM$ $\quad$ $K^{SCoAS}_{i,Pi} = 2000*10^{-3}\ mM$

$K^{SCoAS}_{m,Pi} = 660.0*10^{-3}\ mM$ $\quad$ $K^{SCoAS}_{i,CoaSH} = 20*10^{-3}\ mM$

$K^{SCoAS}_{m,CoaSH} = 20*10^{-3}\ mM$ $\quad$ $K^{SCoAS}_{i,suc} = 3000*10^{-3}\ mM$

$K^{SCoAS}_{m,suc} = 880*10^{-3}\ mM$ $\quad$ $K^{SCoAS}_{i,GTP} = 11.1*10^{-3}\ mM$

<u>Succinate Dehydrogenase</u> (SDH)

The rate equation for SDH was taken from [214]. The kinetics of SDH was modeled as Theorell-Chance bi bi mechanism. The kinetic constants were adopted from previous literature [217, 218, 227-229].

Equation S29. Succinate Dehydrogenase (SDH)

$$r_{SDH} = \frac{V_{f,SDH}\left(C^m_{suc}C^m_{COQ} - \frac{C^m_{QH_2}C^m_{fum}}{K_{eq,SDH}}\right)}{K^{SDH}_{i,suc}K^{SDH}_{m,COQ}\alpha_{SDH,i1} + K^{SDH}_{m,COQ}C^m_{suc} + K^{SDH}_{m,suc}\alpha_{SDH,i1}C^m_{COQ} + C^m_{suc}C^m_{COQ} + \frac{K^{SDH}_{m,suc}}{K^{SDH}_{i,fum}}C^m_{COQ}C^m_{fum}} + \left(\frac{K^{SDH}_{i,suc}K^{SDH}_{m,COQ}}{K^{SDH}_{i,fum}K^{SDH}_{m,QH_2}}\right)\left(K^{SDH}_{m,fum}\alpha_{SDH,i1}C^m_{QH_2} + K^{SDH}_{m,QH_2}C^m_{fum} + \frac{K^{SDH}_{m,fum}}{K^{SDH}_{i,suc}}C^m_{suc}C^m_{QH_2} + C^m_{QH_2}C^m_{fum}\right)}$$

$$\alpha_{SDH,i1} = \frac{\left(1 + \frac{C^m_{OAA}}{K^{SDH}_{i,OAA}} + \frac{C^m_{suc}}{K^{SDH}_{a,suc}} + \frac{C^m_{fum}}{K^{SDH}_{a,fum}}\right)}{\left(1 + \frac{C^m_{suc}}{K^{SDH}_{a,suc}} + \frac{C^m_{fum}}{K^{SDH}_{a,fum}}\right)}$$

$V_{f,SDH} = 5.81*10^4\ mMh^{-1}$
$K_{eq,SDH} = 1.21$
$K^{SDH}_{m,suc} = 467*10^{-3}\ mM$
$K^{SDH}_{m,COQ} = 480*10^{-3}\ mM$
$K^{SDH}_{m,QH_2} = 2.45*10^{-3}\ mM$
$K^{SDH}_{m,fum} = 1200*10^{-3}\ mM$
$K^{SDH}_{i,suc} = 120*10^{-3}\ mM$
$K^{SDH}_{i,fum} = 1275*10^{-3}\ mM$
$K^{SDH}_{i,OAA} = 1.5*10^{-3}\ mM$
$K^{SCoAS}_{a,suc} = 450*10^{-3}\ mM$
$K^{SCoAS}_{a,fum} = 375*10^{-3}\ mM$

Fumarase (FUM)

The rate equation for FUM was taken from [214]. The kinetics of FUM was modeled as ordered uni uni mechanism. The kinetic constants were adopted from previous literature [217, 218, 227, 230, 231].

Equation S30. Fumarase (FUM)

$$r_{FUM} = \frac{V_{f,FUM}\left(C^m_{fum} - \frac{C^m_{mal}}{K_{eq,FUM}}\right)}{K^{FUM}_{m,fum}\alpha_{FUM,i1} + C^m_{fum} + \frac{K^{FUM}_{m,fum}C^m_{mal}}{K^{FUM}_{m,mal}}}$$

$$\alpha_{FUM,i1} = 1 + \frac{C^m_{cit}}{K^{FUM}_{i,cit}} + \frac{C^m_{ATP}P_{fATP}}{K^{FUM}_{i,ATP}P_{ATP}} + \frac{C^m_{ADP}P_{fADP}}{K^{FUM}_{i,ADP}P_{ADP}} + \frac{C^m_{GTP}P_{fGTP}}{K^{FUM}_{i,GTP}P_{GTP}} + \frac{C^m_{GDP}P_{fGDP}}{K^{FUM}_{i,GDP}P_{GDP}}$$

$V_{f,FUM} = 2.21*10^4\ mMh^{-1}$
$K_{eq,FUM} = 4.56$
$K^{FUM}_{m,fum} = 44.7*10^{-3}\ mM$
$K^{FUM}_{m,mal} = 197.7*10^{-3}\ mM$
$K^{FUM}_{i,cit} = 3500*10^{-3}\ mM$
$K^{FUM}_{i,ATP} = 40*10^{-3}\ mM$
$K^{SDH}_{i,ADP} = 400*10^{-3}\ mM$
$K^{SDH}_{i,GTP} = 80*10^{-3}\ mM$
$K^{SDH}_{i,GDP} = 330*10^{-3}\ mM$

Malate Dehydrogenase 2 (MDH2)

MDH2 is the isoform that is present in the mitochondria. The rate equation for MDH2 was taken from [214]. The kinetics of MDH2 employs the ordered bi bi mechanism. The kinetic constants were adopted from previous literature [217, 218, 232, 233].

Equation S31. Malate Dehydrogenase 2 (MDH2)

$$r_{MDH2} = \frac{V_{f,MDH2}\left(C^m_{NAD^+}C^m_{mal} - \frac{C^m_{OAA}C^m_{NADH}}{K_{eq,MDH2}}\right)}{K^{MDH2}_{i,NAD^+}K^{MDH2}_{m,mal}\alpha_{MDH2,i} + K^{MDH2}_{m,mal}C^m_{NAD^+} + K^{MDH2}_{m,NAD^+}\alpha_{MDH2,i}C^m_{mal} + C^m_{NAD^+}C^m_{mal} + \frac{K^{MDH2}_{m,NAD^+}C^m_{mal}C^m_{NADH}}{K^{MDH2}_{i,NADH}} + \frac{C^m_{NAD^+}C^m_{mal}C^m_{OAA}}{K^{MDH2}_{i,OAA}} + \left(\frac{K^{MDH2}_{i,NAD^+}K^{MDH2}_{m,mal}}{K^{MDH2}_{i,NADH}K^{MDH2}_{m,OAA}}\right)\left(K^{MDH2}_{m,NADH}\alpha_{MDH2,i}C^m_{OAA} + K^{MDH2}_{m,OAA}C^m_{NADH} + \frac{K^{MDH2}_{mNADH}}{K^{MDH2}_{i,NAD^+}}C^m_{NAD^+}C^m_{OAA} + C^m_{OAA}C^m_{NADH} + \frac{C^m_{mal}C^m_{OAA}C^m_{NADH}}{K^{MDH2}_{i,mal}}\right)}$$

$$\alpha_{MDH2,i} = \left(1 + \frac{C^m_{ATP}P_{fATP}}{K^{MDH2}_{i,ATP}P_{ATP}} + \frac{C^m_{ADP}P_{fADP}}{K^{MDH2}_{i,ADP}P_{ADP}} + \frac{C^m_{AMP}P_{fAMP}}{K^{MDH2}_{i,AMP}P_{AMP}}\right)$$

$V_{f,MDH2} = 3.53*10^{8}\ mMh^{-1}$
$K_{eq,MDH2} = 4.02*10^{-4}$
$K^{MDH2}_{m,NAD^+} = 90.55*10^{-3}mM$
$K^{MDH2}_{m,mal} = 250*10^{-3}mM$
$K^{MDH2}_{m,OAA} = 6.128*10^{-3}mM$
$K^{MDH2}_{m,NADH} = 2.58*10^{-3}mM$
$K^{MDH2}_{i,NAD^+} = 279*10^{-3}mM$
$K^{MDH2}_{i,mal} = 360*10^{-3}mM$
$K^{MDH2}_{i,OAA} = 5.5*10^{-3}mM$
$K^{MDH2}_{i,NADH} = 3.18*10^{-3}mM$
$K^{MDH2}_{i,ATP} = 183.2*10^{-3}mM$
$K^{MDH2}_{i,ADP} = 394.4*10^{-3}mM$
$K^{MDH2}_{i,AMP} = 420.0*10^{-3}mM$

NAD/NADH SHUTTLES

Glutamate Oxaloacetate Transaminase 2 (GOT2)

GOT2 is the isoform that is present in the mitochondria. The rate equation for GOT2 was taken from [214]. The kinetics of GOT2 is modeled as ping pong bi bi mechanism. The kinetic constants were adopted from previous literature [234].

Equation S32. Glutamate Oxaloacetate Transaminase 2 (GOT2)

$$r_{GOT2} = \frac{V_{f,GOT2}\left(C^m_{asp}C^m_{akg} - \frac{C^m_{OAA}C^m_{glu}}{K_{eq,GOT2}}\right)}{K^{GOT2}_{m,akg}C^m_{asp} + K^{GOT2}_{m,asp}\alpha_{GOT2,i}C^m_{akg} + C^m_{asp}C^m_{akg} + \frac{K^{GOT2}_{m,asp}C^m_{akg}C^m_{glu}}{K^{GOT2}_{i,glu}} + \left(\frac{K^{GOT2}_{i,asp}K^{GOT}_{m,akg}}{K^{GOT2}_{m,OAA}K^{GOT2}_{i,glu}}\right)\left(\frac{K^{GOT2}_{m,glu}C^m_{asp}C^m_{OAA}}{K^{GOT2}_{i,asp}} + C^m_{OAA}C^m_{glu} + K^{GOT2}_{m,glu}\alpha_{GOT2,i}C^m_{OAA} + K^{GOT2}_{m,OAA}C^m_{glu}\right)}$$

$$\alpha_{GOT2,i} = \left(1 + \frac{C^m_{akg}}{K^{GOT2}_{i,akg}}\right)$$

$V_{f,GOT} = 3.87*10^6\ mMh^{-1}$
$K_{eq,GOT} = 1.56$
$K^{GOT}_{m,asp} = 0.89\ mM$
$K^{GOT}_{m,akg} = 3.22\ mM$
$K^{GOT}_{m,OAA} = 88*10^{-3}\ mM$
$K^{GOT}_{m,glu} = 32.5\ mM$
$K^{GOT}_{i,asp} = 3.9\ mM$
$K^{GOT}_{i,akg} = 0.73\ mM$
$K^{GOT}_{i,OAA} = 48*10^{-3}\ mM$
$K^{GOT}_{i,glu} = 10.7\ mM$
$K^{GOT}_{i,AKG} = 26.5\ mM$

<u>Malate Dehydrogenase 1</u> (MDH1)

MDH1 is the isoform that is present in the mitochondria. The rate equation and kinetic constants for MDH1 were taken from [235]. The kinetics of MDH1 was modeled as ordered bi bi mechanism.

Equation S33. Malate Dehydrogenase 1 (MDH1)

$$r_{MDH1} = \frac{V_{mf,MDH1}\left(C^c_{OAA}C^c_{NADH} - \frac{C^c_{NAD^+}C^c_{mal}}{K_{eq,MDH1}}\right)}{K^{MDH1}_{i,NADH}K^{MDH1}_{m,OAA} + K^{MDH1}_{m,OAA}C^c_{NADH} + K^{MDH1}_{m,NADH}C^c_{OAA} + C^c_{OAA}C^c_{NADH} + \frac{K^{MDH1}_{m,NADH}C^c_{OAA}C^c_{NAD^+}}{K^{MDH1}_{i,NAD^+}} + \frac{C^c_{OAA}C^c_{NADH}C^c_{mal}}{K^{MDH1}_{i,mal}} + \frac{K^{MDH1}_{i,NADH}K^{MDH1}_{m,OAA}}{K^{MDH1}_{i,NAD^+}K^{MDH1}_{m,mal}}\left(K^{MDH1}_{m,NAD^+}C^c_{mal} + K^{MDH1}_{m,mal}C^c_{NAD^+} + \frac{K^{MDH1}_{m,NAD^+}C^c_{Mal}C^c_{NADH}}{K^{MDH1}_{i,NADH}} + C^c_{NAD^+}C^c_{Mal} + \frac{C^c_{Mal}C^c_{OAA}C^c_{NAD^+}}{K^{MDH1}_{i,OAA}}\right)}$$

$V_{mf,MDH1} = 3.59*10^7 mM\ h^{-1}$
$K_{eq,MDH1} = 2.67*10^4$
$K^{MDH1}_{m,NAD^+} = 0.114\ mM$
$K^{MDH1}_{m,mal} = 1.1\ mM$
$K^{MDH1}_{m,OAA} = 0.088\ mM$
$K^{MDH1}_{m,NADH} = 0.026\ mM$
$K^{MDH1}_{i,NADH} = 4.9*10^{-3}\ mM$
$K^{MDH1}_{i,OAA} = 63*10^{-3}\ mM$
$K^{MDH1}_{i,mal} = 7.1\ mM$
$K^{MDH1}_{i,NAD^+} = 0.94\ mM$

Glutamate Oxaloacetate Transaminase 1 (GOT1)

GOT1 is the isoform that is present in the cytosol. The rate equation for GOT1 was taken from [214]. The kinetics of GOT1 was modeled as ping pong bi bi mechanism. The kinetic constants were adopted from previous literature [234].

Equation S34. Glutamate Oxaloacetate Transaminase 1 (GOT1)

$$r_{GOT1} = \frac{V_{mf,GOT1}\left(C^c_{asp}C^c_{akg} - \frac{C^c_{OAA}C^c_{glu}}{K_{eq,GOT1}}\right)}{K^{GOT1}_{m,akg}C^c_{asp} + K^{GOT1}_{m,asp}\alpha_{GOT1,i}C^c_{akg} + C^c_{asp}C^c_{akg} + \frac{K^{GOT1}_{m,asp}C^c_{akg}C^c_{glu}}{K^{GOT1}_{i,glu}} + \left(\frac{K^{GOT1}_{i,asp}K^{GO1}_{m,akg}}{K^{GOT1}_{m,OAA}K^{GOT1}_{i,glu}}\right)\left(\frac{K^{GOT1}_{m,glu}C^c_{asp}C^c_{OAA}}{K^{GOT1}_{i,asp}} + C^c_{OAA}C^c_{glu} + K^{GOT1}_{m,glu}\alpha_{GOT1,i}C^c_{OAA} + K^{GOT1}_{m,OAA}C^c_{glu}\right)}$$

$$\alpha_{GOT1,i} = \left(1 + \frac{C^c_{akg}}{K^{GOT1}_{i,akg}}\right)$$

$V_{mf,GOT1} = 2.36 * 10^3\ mMh^{-1}$
$K_{eq,GOT} = 1.56$
$K^{GOT}_{m,asp} = 4.4mM$
$K^{GOT}_{m,akg} = 0.38mM$
$K^{GOT}_{m,OAA} = 95 * 10^{-3}mM$
$K^{GOT}_{m,glu} = 9.6mM$
$K^{GOT}_{i,asp} = 3.9mM$
$K^{GOT}_{i,akg} = 0.73mM$
$K^{GOT}_{i,OAA} = 48 * 10^{-3}mM$
$K^{GOT}_{i,glu} = 8.4mM$
$K^{GOT}_{i,akg} = 26.5mM$

α-Ketoglutarate –Malate shuttle (AKGMAL)

The rate equation for AKGMAL was taken from [214]. The kinetics of AKGMAL was modeled as rapid equilibrium random bi bi mechanism. The kinetic constants were adopted from previous literature [236].

Equation S35. α-Ketoglutarate –Malate shuttle (AKGMAL)

$$r_{AKGMAL} = \frac{V_{mf,AKGMAL}\left(C^c_{akg}C^m_{mal} - C^m_{akg}C^c_{mal}\right)}{K^{AKGMAL}_{m,akgi}K^{AKGMAL}_{m,malx}\left(2 + \frac{C^c_{mal}}{K^{AKGMAL}_{m,mali}} + \frac{C^m_{mal}}{K^{AKGMAL}_{m,malx}} + \frac{C^c_{akg}}{K^{AKGMAL}_{m,akgi}} + \frac{C^m_{akg}}{K^{AKGMAL}_{m,akgx}} + \frac{C^c_{mal}C^m_{akg}}{K^{AKGMAL}_{m,mali}K^{AKGMAL}_{m,akgx}} + \frac{C^m_{mal}C^c_{akgi}}{K^{AKGMAL}_{m,malx}K^{AKGMAL}_{m,akgi}}\right)}$$

$$V_{mf,AKGMAL} = 3.19*10^{6}\ mM\ h^{-1}$$
$$K_{m,mali}^{AKGMAL} = 0.4\ mM$$
$$K_{m,malx}^{AKGMAL} = 10\ mM$$
$$K_{m,akgi}^{AKGMAL} = 1.3\ mM$$
$$K_{m,akgx}^{AKGMAL} = 0.17\ mM$$

<u>Aspartate –Glutamate shuttle</u> (ASPGLU)

The rate equation for ASPGLU was taken from [214]. The kinetics of ASPGLU was modeled as rapid equilibrium random bi bi with charge translocation mechanism. The kinetic constants were adopted from previous literature [237].

Equation S36. Aspartate –Glutamate shuttle (ASPGLU)

$$r_{ASPGLU} = \frac{V_{mf,ASPGLU}\left(K_{eq,ASPGLU}C_{asp}^{c}C_{glu}^{m}C_{H^+}^{m} - C_{asp}^{m}C_{glu}^{c}C_{H^+}^{c}\right)}{K_{eq,ASPGLU}K_{i,aspi}^{ASPGLU}K_{i,glux}^{ASPGLU}K_{H^+}^{ASPGLU}\left(2m + m\frac{C_{asp}^{c}}{K_{i,aspi}^{ASPGLU}} + \frac{C_{asp}^{c}C_{glu}^{m}C_{H^+}^{m}}{K_{i,aspi}^{ASPGLU}K_{i,glux}^{ASPGLU}K_{H^+}^{ASPGLU}} + m\frac{C_{asp}^{m}C_{H^+}^{c}}{K_{i,aspx}^{ASPGLU}K_{H^+}^{ASPGLU}} + m\frac{C_{asp}^{m}}{K_{i,aspx}^{ASPGLU}} + \frac{C_{asp}^{m}C_{glu}^{c}C_{H^+}^{c}}{K_{i,aspx}^{ASPGLU}K_{i,glui}^{ASPGLU}K_{H^+}^{ASPGLU}} + m\frac{C_{asp}^{c}C_{H^+}^{m}}{K_{i,aspi}^{ASPGLU}K_{H^+}^{ASPGLU}} + m\frac{C_{H^+}^{m}}{K_{H^+}^{ASPGLU}} + m\frac{C_{glu}^{c}C_{H^+}^{c}}{K_{i,glui}^{ASPGLU}K_{H^+}^{ASPGLU}} + m\frac{C_{H^+}^{c}}{K_{H^+}^{ASPGLU}} + m\frac{C_{glu}^{m}C_{H^+}^{m}}{K_{i,glux}^{ASPGLU}K_{H^+}^{ASPGLU}}\right)}$$

$$V_{mf,ASPGLU} = 2.49*10^{4}\ mM\ h^{-1}$$
$$K_{eq,ASPGLU} = 0.6$$
$$K_{i,aspi}^{ASPGLU} = 0.028\ mM$$
$$K_{i,aspx}^{ASPGLU} = 2.8\ mM$$
$$K_{i,glui}^{ASPGLU} = 0.18\ mM$$
$$K_{i,glux}^{ASPGLU} = 1.6\ mM$$
$$K_{H^+}^{ASPGLU} = 10^{-6.5}\ mM$$
$$m = 1.8$$

TRANSPORTERS

<u>Glucose Transporter</u> (GLUT): Glucose transporters mediate transport of glucose across plasma membranes. Till date, fourteen glucose transporters (isozymes) have been

identified which perform the same function but have very different kinetic properties [238]. Kinetics of the GLUT1 isozyme was considered in the model and was modeled as uni uni steady state kinetics.

Equation S37. Glucose Transporter (GLUT):

$$r_{GlcTr} = \frac{V_{mf}^{GlcTr}\frac{C_{glc}^{e}}{K_{glc}^{GlcTr}} - V_{mr}^{GlcTr}\frac{C_{glc}^{c}}{K_{glc}^{GlcTr}}}{1 + \frac{C_{glc}^{e}}{K_{glc}^{GlcTr}} + \frac{C_{glc}^{c}}{K_{glc}^{GlcTr}}}$$

$V_{mf}^{GlcTr} = 7.67\ \text{mM}h^{-1}$

$V_{mr}^{GlcTr} = 0.767\ \text{mM}h^{-1}$

$K_{glc}^{GlcTr} = 1.50\ mM$

The rate equations and kinetic constants for GLUT isoforms. Isoform-specific parameters are colored blue.

$$r_{GLUT_i} = \frac{V_{mf}^{GLUT}\frac{C_{glc}^{e}}{K_{e,glc}^{GLUT_i}} - V_{mr}^{GLUT}\frac{C_{glc}^{c}}{K_{c,glc}^{GLUT_i}}}{1 + \frac{C_{glc}^{e}}{K_{e,glc}^{GLUT_i}} + \frac{C_{glc}^{c}}{K_{c,glc}^{GLUT_i}}}$$

$V_{mf}^{GLUT} = 7.27\ mM\ h^{-1}$

$V_{mr}^{GLUT} = 7.27\ mM\ h^{-1}$

$$r_{GLUT} = \sum_{i=1}^{4} \rho_{GLUT_i} r_{GLUT_i}$$

	$K_{e,glc}^{GLUT_i}$	$K_{c,glc}^{GLUT_i}$ [10]	Refs.
GLUT1	3	0.3	[239]
GLUT2	17	1.7	[239, 240]
GLUT3	1.4[11]	0.14	[241]
GLUT4	6.6	0.66	[239]

	ρ_{GLUT_i}			
	D6	D10	D14	D20
GLUT1	0.13	0.08	0.12	0.30
GLUT2	0.005	0.005	0.007	0.008
GLUT3	0.86	0.85	0.73	0.68

[10] $K_{c,glc}^{GLUT_i}$ was estimated as 10% of $K_{e,glc}^{GLUT_i}$

[11] For deoxyglucose

GLUT4	0.006	0.005	0.005	0.005

Pyruvate –Hydrogen shuttle (PYRH)

PYRH was modeled as reversible mass action kinetics. The rate equation was taken from [246].

Equation S38. Pyruvate –Hydrogen shuttle (PYRH)

$$r_{PYRH} = V_{m,PYRH}\left(C^{c}_{pyr}C^{c}_{H^+} - C^{m}_{pyr}C^{m}_{H^+}\right) \qquad V_{m,PYRH}=1*10^{13}\ mM\ h^{-1}$$

Citrate –Malate shuttle (CITMAL)

CITMAL was modeled as reversible mass action kinetics. The rate equation was taken from [246].

Equation S39. Citrate –Malate shuttle (CITMAL)

$$r_{CITMAL} = V_{m,CITMAL}\left(C^{c}_{cit}C^{m}_{mal} - C^{m}_{cit}C^{c}_{mal}\right) \qquad V_{m,CITMAL} = 296.6\,mM\ h^{-1}$$

Malate-Phosphate shuttle (MALPi)

MALPi was modeled as reversible mass action kinetics. The rate equation was taken from [246].

Equation S40. Malate-Phosphate shuttle (MALPi)

$$r_{MALPi} = V_{m,MALPi}\left(C^{c}_{mal}C^{m}_{Pi} - C^{m}_{mal}C^{c}_{Pi}\right) \qquad V_{m,MALPi} = 17.3\,mM\ h^{-1}$$

Glutamate-Hydrogen shuttle (GLUH)

GLUH was modeled as reversible mass action kinetics. The rate equation was taken from [246].

Equation S41. Glutamate-Hydrogen shuttle (GLUH)

$$r_{GLUH} = V_{m,GLUH}\left(C^{c}_{glu}C^{c}_{H^+} - C^{m}_{glu}C^{m}_{H^+}\right) \qquad V_{m,GLUH} = 3.87*10^{8}\ mM\ h^{-1}$$

OTHER REACTIONS

<u>Glutaminase</u> (GLS)

The kinetics of GLS was modeled as simple Michaelis-Menten kinetics with non-competitive inhibition by glutamate. The kinetic constants for GLS were taken from [242].

Equation S42. Glutaminase (GLS)

$$r_{GLS} = \frac{V_{m,GLS}\left(C^{c}_{gln} - \frac{C^{m}_{glu}}{K_{eq,GLS}}\right)}{K^{GLS}_{m,gln}\left(1+\frac{C^{m}_{glu}}{K^{GLS}_{i,glu}}\right)+C^{c}_{gln}}$$

$$V_{m,GLS} = 38.8\,mM\ h^{-1}$$
$$K_{eq,GLS} = 1$$
$$K^{GLS}_{m,gln} = 12\,mM$$
$$K^{GLS}_{i,glu} = 55\,mM$$

<u>Glutamate Dehydrogenase</u> (GDH)

The kinetic constants for GDH were taken from [243, 244]. The kinetics of GDH was modeled as random bi bi mechanism.

Equation S43. Glutamate Dehydrogenase (GDH)

$$r_{GDH} = \frac{V_{f,GDH}\left(C^{m}_{NAD}C^{m}_{Glu} - \frac{C^{m}_{AKG}C^{m}_{NADH}C^{m}_{NH3}}{K_{eq,GDH}}\right)}{\begin{aligned}
&K^{GDH}_{i,NAD}K^{GDH}_{Glu} + K^{GDH}_{m,Glu}C^{m}_{NAD} + K^{GDH}_{m,NAD}C^{m}_{Glu} + C^{m}_{Glu}C^{m}_{NAD} + \frac{C^{m}_{Glu}C^{m}_{NAD}C^{m}_{NH3}}{K^{GDH}_{i,AKG}} + \frac{K^{GDH}_{i,NAD}K^{GDH}_{m,Glu}C^{m}_{NADH}}{K^{GDH}_{i,NADH}} \\
&+\frac{K^{GDH}_{m,Glu}C^{m}_{NAD}C^{m}_{NH3}}{K^{GDH}_{i,NH3}} + \frac{K^{GDH}_{i,NAD}K^{GDH}_{m,Glu}K^{GDH}_{m,NADH}C^{m}_{AKG}C^{m}_{NH3}}{K^{GDH}_{m,NH3}K^{GDH}_{i,AKG}K^{GDH}_{i,NADH}} + \frac{K^{GDH}_{m,NAD}C^{m}_{Glu}C^{m}_{NADH}}{K^{GDH}_{i,NADH}} + \frac{C^{m}_{Glu}C^{m}_{AKG}C^{m}_{NAD}C^{m}_{NH3}}{K^{GDH}_{i,NH3}K^{GDH}_{i,AKG}} \\
&+\frac{K^{GDH}_{i,NAD}K^{GDH}_{m,Glu}K^{GDH}_{m,AKG}C^{m}_{NADH}C^{m}_{NH3}}{K^{GDH}_{m,NH3}K^{GDH}_{i,AKG}K^{GDH}_{i,NADH}} + \frac{K^{GDH}_{i,NAD}K^{GDH}_{m,Glu}K^{GDH}_{m,AKG}C^{m}_{NH3}C^{m}_{AKG}C^{m}_{NADH}}{K^{GDH}_{m,NH3}K^{GDH}_{i,AKG}K^{GDH}_{i,NADH}} + \frac{C^{m}_{Glu}C^{m}_{NAD}C^{m}_{AKG}}{K^{GDH}_{i,AKG}} \\
&+\frac{K^{GDH}_{i,NAD}K^{GDH}_{m,Glu}K^{GDH}_{m,AKG}C^{m}_{NH3}}{K^{GDH}_{m,NH3}K^{GDH}_{i,AKG}} + \frac{K^{GDH}_{i,NAD}K^{GDH}_{m,Glu}C^{m}_{Glu}C^{m}_{NADH}C^{m}_{AKG}}{K^{GDH}_{i,Glu}K^{GDH}_{i,AKG}K^{GDH}_{i,NADH}} + \frac{K^{GDH}_{i,NAD}K^{GDH}_{m,Glu}C^{m}_{AKG}C^{m}_{NADH}}{K^{GDH}_{i,AKG}K^{GDH}_{i,NADH}} \\
&+\frac{K^{GDH}_{m,NADH}K^{GDH}_{m,Glu}C^{m}_{NH3}C^{m}_{AKG}C^{m}_{NAD}}{K^{GDH}_{m,NH3}K^{GDH}_{i,AKG}K^{GDH}_{i,NADH}} + \frac{K^{GDH}_{i,NAD}K^{GDH}_{m,Glu}C^{m}_{Glu}C^{m}_{AKG}C^{m}_{NADH}C^{m}_{NH3}}{K^{GDH}_{m,NH3}K^{GDH}_{i,Glu}K^{GDH}_{i,AKG}K^{GDH}_{i,NADH}}
\end{aligned}}$$

$V_{f,GDH} = 5.55*10^{3}\ mM^{-1}h^{-1}$
$K_{m,Glu}^{GDH} = 3.5\ mM$
$K_{m,NADH}^{GDH} = 0.04\ mM$
$K_{m,AKG}^{GDH} = 1.1\ mM$
$K_{m,NH3}^{GDH} = 6\ mM$
$K_{i,AKG}^{GDH} = 0.25\ mM$
$K_{i,NH3}^{GDH} = 6\ mM$
$K_{i,Glu}^{GDH} = 3.5\ mM$
$K_{i,NADH}^{GDH} = 0.004\ mM$
$K_{i,NAD}^{GDH} = 1\ mM$
$K_{eq,GDH} = 0.003$

ATP-Citrate Lyase (CLY)

The kinetics of CLY was modeled as ordered bi bi mechanism. The kinetic constants were adopted from previous literature [245-248].

Equation S44. ATP-Citrate Lyase (CLY)

$$r_{CLY} = \frac{V_{m,CLY} C_{cit}^{c} C_{CoASH}^{c}}{K_{i,cit}^{CLY} K_{m,CoASH}^{CLY} + K_{m,cit}^{CLY} C_{CoASH}^{c} + K_{m,AcCoA}^{CLY} C_{cit}^{c} + C_{cit}^{c} C_{CoASH}^{c} + \frac{K_{m,cit}^{CLY} C_{CoASH}^{c} C_{AcCoA}^{c}}{K_{i,AcCoA}^{CLY}} + \frac{C_{cit}^{c} C_{CoASH}^{c} C_{OAA}^{c}}{K_{i,OAA}^{CLY}} + \frac{K_{i,cit}^{CLY} K_{m,CoASH}^{CLY}}{K_{m,OAA}^{CLY} K_{i,AcCoA}^{CLY}} \left(K_{m,AcCoA}^{CLY} C_{OAA}^{c} + K_{m,OAA}^{CLY} C_{AcCoA}^{c} + \frac{K_{m,AcCoA}^{CLY} C_{cit}^{c} C_{OAA}^{c}}{K_{i,cit}^{CLY}} + C_{OAA}^{c} C_{AcCoA}^{c} + \frac{C_{CoASH}^{c} C_{OAA}^{c} C_{AcCoA}^{c}}{K_{i,CoASH}^{CLY}} \right)}$$

$V_{m,CLY} = 17.5\ mM^{-1}h^{-1}$
$K_{m,cit}^{CLY} = 0.0493\ mM$
$K_{i,cit}^{CLY} = 0.0475\ mM$
$K_{m,CoASH}^{CLY} = 4.4*10^{-3}\ mM$
$K_{i,CoASH}^{CLY} = 6.1*10^{-3}\ mM$
$K_{m,OAA}^{CLY} = 0.177\ mM$
$K_{i,OAA}^{CLY} = 0.177\ mM$
$K_{m,AcCoA}^{CLY} = 9.8*10^{-3}\ mM$
$K_{i,AcCoA}^{CLY} = 9.8*10^{-3}\ mM$

Mitochondrial Malic Enzyme (MMALIC)

The rate equation and kinetic constants for CMALIC were adopted from [249]. The kinetics of CMALIC was modeled as ordered bi ter mechanism.

Equation S45. Mitochondrial Malic Enzyme (MMALIC)

$$r_{mmalic} = \frac{V_{mmalic}\left(C^m_{mal}C^m_{NAD^+} - \frac{C^m_{pyr}C^m_{NADH}C^m_{CO_2}}{K_{eq,mmalic}}\right)}{K^{mmalic}_{mal}C^m_{NAD^+}\left(1+\frac{C^m_{ATP}}{K^{mmalic}_{i,ATP}}\right) + K^{mmalic}_{NAD^+}C^m_{mal} + K^{mmalic}_{mal}K^{mmalic}_{NAD^+}}$$

$V_{mmalic} = 46.3\ mM^{-1}h^{-1}$
$K_{eq,mmalic} = 34.4$
$K^{mmalic}_{mal} = 1.7\ mM$
$K^{mmalic}_{NAD} = 0.16\ mM$
$K^{mmalic}_{i,ATP} = 0.5\ mM$

<u>Cytosolic Malic Enzyme</u> (CMALIC)

The rate equation and kinetic constants for CMALIC were taken from [250]. The kinetics of CMALIC was modeled as ordered bi ter mechanism.

Equation S46. Cytosolic Malic Enzyme (CMALIC)

$$r_{cmalic} = \frac{V_{f,cmalic}\left(C^c_{mal}C^c_{NADP} - \frac{C^c_{CO_2}C^c_{pyr}C^c_{NADPH}}{K_{eq,cmalic}}\right)}{K^{cmalic}_{i,NADP}K^{cmalic}_{m,mal} + K^{cmalic}_{m,mal}C^c_{NADP} + K^{cmalic}_{m,NADP}C^c_{mal} + C^c_{mal}C^c_{NADP} + \frac{K^{cmalic}_{i,NADP}K^{cmalic}_{m,mal}K^{cmalic}_{m,pyr}C^c_{CO_2}}{K^{cmalic}_{m,CO_2}K^{cmalic}_{i,pyr}}}$$
$$+ \frac{K^{cmalic}_{i,NADP}K^{cmalic}_{m,mal}C^c_{NADPH}}{K^{cmalic}_{i,NADPH}} + \frac{K^{cmalic}_{m,mal}K^{cmalic}_{m,NADPH}C^c_{NADP}C^c_{pyr}}{K^{cmalic}_{i,pyr}K^{cmalic}_{i,NADPH}}\left(\frac{C^c_{CO_2}}{K^{cmalic}_{m,CO_2}} + \frac{K^{cmalic}_{i,CO_2}C^c_{mal}}{K^{cmalic}_{i,mal}K^{cmalic}_{m,CO_2}} + \frac{C^c_{mal}C^c_{CO_2}}{K^{cmalic}_{i,mal}K^{cmalic}_{m,CO_2}}\right)$$
$$+ \frac{K^{cmalic}_{m,NADP}C^c_{mal}C^c_{NADPH}}{K^{cmalic}_{i,NADPH}}\left(1+\frac{C^c_{pyr}}{K^{cmalic}_{i,pyr}} + \frac{C^c_{CO_2}C^c_{pyr}}{K^{cmalic}_{i,CO_2}K^{cmalic}_{i,pyr}}\right) + \frac{K^{cmalic}_{m,mal}K^{cmalic}_{i,NADP}K^{cmalic}_{m,pyr}C^c_{NADPH}}{K^{cmalic}_{i,pyr}K^{cmalic}_{i,NADPH}}\left(\frac{C^c_{pyr}}{K^{cmalic}_{m,pyr}} + \frac{C^c_{CO_2}}{K^{cmalic}_{m,CO_2}}\right)$$
$$+ \frac{K^{cmalic}_{m,mal}K^{cmalic}_{i,NADP}K^{cmalic}_{m,NADPH}C^c_{CO_2}C^c_{pyr}}{K^{cmalic}_{m,CO_2}K^{cmalic}_{i,pyr}K^{cmalic}_{i,NADPH}}\left(1+\frac{C^c_{NADPH}}{K^{cmalic}_{m,NADPH}}\right) + \frac{K^{cmalic}_{m,mal}K^{cmalic}_{m,pyr}C^c_{NADP}C^c_{CO_2}}{K^{cmalic}_{m,CO_2}K^{cmalic}_{i,pyr}}\left(1+\frac{C^c_{mal}}{K^{cmalic}_{i,mal}}\right)$$

$V_{f,cmalic} = 174\ mM^{-1}h^{-1}$
$K^{cmalic}_{i,NADP} = 9.6*10^{-4}\ mM$
$K^{cmalic}_{m,mal} = 120*10^{-3}\ mM$
$K^{cmalic}_{i,mal} = 0.22\ mM$
$K^{cmalic}_{m,NADP} = 1.4*10^{-3}\ mM$
$K^{cmalic}_{i,CO_2} = 11.7*10^{-3}\ mM$
$K^{cmalic}_{m,CO_2} = 13*10^{-3}\ mM$
$K^{cmalic}_{i,pyr} = 7.8\ mM$
$K^{cmalic}_{m,pyr} = 6.4*10^{-3}\ mM$
$K^{cmalic}_{i,NADPH} = 2*10^{-3}\ mM$
$K^{cmalic}_{m,NADPH} = 2.1*10^{-3} mM$
$K_{eq,cmalic} = 34.4$

<u>Glutamate Alanine Transaminase</u> (GPT)

The rate equation and kinetic constants for GPT were taken from [251]. The kinetics of GPT was modeled as ping pong bi bi mechanism.

Equation S47. Glutamate Alanine Transaminase (GPT)

$$r_{GPT} = \frac{V_{f,GPT}\left(C^m_{Ala}C^m_{AKG} - \frac{C^m_{Pyr}C^m_{Glu}}{K_{eq,GPT}}\right)}{K^{GPT}_{Ala}C^m_{AKG} + K^{GPT}_{AKG}C^m_{Ala} + C^m_{AKG}C^m_{Ala} + \frac{K^{GPT}_{Ala}C^m_{AKG}C^m_{Glu}}{K^{GPT}_{i,Glu}} + \frac{K^{GPT}_{AKG}C^m_{Ala}C^m_{Ala}}{K^{GPT}_{IA}} + \frac{K^{GPT}_{AKG}C^m_{Ala}C^m_{Glu}}{K^{GPT}_{RG}} + \frac{V_{f,GPT}}{V_{r,GPT}K_{eq,GPT}}\left(K^{GPT}_{Pyr}C^m_{Glu} + K^{GPT}_{Glu}C^m_{Pyr} + C^m_{Pyr}C^m_{Glu} + \frac{K^{GPT}_{AKG}C^m_{Ala}C^m_{Pyr}}{K^{GPT}_{i,Pyr}} + \frac{K^{GPT}_{Pyr}C^m_{Glu}C^m_{Glu}}{K^{GPT}_{IG}}\right)}$$

$V_{f,GPT} = 66.4\ mM^{-1}h^{-1}$
$V_{r,GPT} = 3.97*10^{7}\ mM^{-1}h^{-1}$
$K^{GPT}_{Ala} = 3\ mM$
$K^{GPT}_{AKG} = 0.12\ mM$
$K^{GPT}_{Pyr} = 0.23\ mM$
$K^{GPT}_{Glu} = 8.1\ mM$
$K^{GPT}_{i,Pyr} = 0.23\ mM$
$K^{GPT}_{i,Glu} = 2.8\ mM$
$K^{GPT}_{IA} = 470\ mM$
$K^{GPT}_{IG} = 96\ mM$
$K^{GPT}_{RG} = 79.16\ mM$
$K_{eq,GPT} = 2.2$

Pyruvate Carboxylase (PC)

The kinetics of PC was modeled as bi uni mechanism. The kinetic constants for PC were taken from [252].

Equation S48. Pyruvate Carboxylase (PC)

$$r_{PC} = \frac{V_{PC}\left(C^m_{pyr}C^m_{CO_2} - \frac{C^m_{OAA}}{K_{eq,PC}}\right)}{K^{PC}_{m,pyr}K^{PC}_{m,CO_2} + K^{PC}_{m,pyr}C^m_{CO_2} + K^{PC}_{m,CO_2}C^m_{pyr} + C^m_{pyr}C^m_{CO_2}}$$

$V_{PC} = 718.2\ mM^{-1}h^{-1}$
$K^{PC}_{m,pyr} = 0.22\ mM$
$K^{PC}_{m,CO_2} = 3.2\ mM$
$K_{eq,PC} = 1$

Mono Carboxylate Transporter (MCT)

The kinetics of MCT was modeled as ordered bi bi mechanism. The kinetic constants for MCT were adopted from [253, 254].

Equation S49. Mono Carboxylate Transporter (MCT)

$$r_{MCT} = \frac{V_{m,MCT}\left(C^c_{H^+}C^c_{lac} - C^e_{H^+}C^e_{lac}\right)}{K^{MCT}_{m,laci}K^{MCT}_{i,H^+} + K^{MCT}_{m,H^+}C^c_{lac} + K^{MCT}_{m,laci}C^c_{H^+} + K^{MCT}_{m,H^+}C^e_{lac} + K^{MCT}_{m,laci}C^e_{H^+} + C^c_{H^+}C^c_{lac}}$$
$$C^e_{H^+}C^e_{lac} + \frac{K^{MCT}_{m,H^+}C^c_{lac}C^e_{H^+}}{K^{MCT}_{i,H^+}} + \frac{K^{MCT}_{m,H^+}C^e_{lac}C^c_{H^+}}{K^{MCT}_{i,H^+}} + \frac{C^c_{lac}C^c_{H^+}C^e_{H^+}}{K^{MCT}_{ii,H^+}} + \frac{C^e_{lac}C^c_{H^+}C^e_{H^+}}{K^{MCT}_{ii,H^+}}$$

$V_{MCT} = 2.73*10^{3}\ mM^{-1}h^{-1}$
$K^{MCT}_{m,H^+} = 10^{-4}\ mM$
$K^{MCT}_{m,laci} = 2.5\ mM$
$K^{MCT}_{i,H^+} = 2*10^{-4}\ mM$
$K^{MCT}_{ii,H^+} = 2*10^{-4}\ mM$

$P_{ATP} = 1 + \frac{C^m_{H^+}}{K_{HATP}} + \frac{C^m_{Mg}}{K_{MgATP}} + \frac{C^m_K}{K_{KATP}}$	$K_{HATP} = 2.57*10^{-7}M$ $K_{MgATP} = 1.51*10^{-4}M$ $K_{KATP} = 1.35*10^{-2}M$
$P_{ADP} = 1 + \frac{C^m_{H^+}}{K_{HADP}} + \frac{C^m_{Mg}}{K_{MgADP}} + \frac{C^m_K}{K_{KADP}}$	$K_{HADP} = 3.8*10^{-7}M$ $K_{MgADP} = 1.62*10^{-3}M$ $K_{KADP} = 2.95*10^{-2}M$
$P_{AMP} = 1 + \frac{C^m_{H^+}}{K_{HAMP}} + \frac{C^m_{Mg}}{K_{MgAMP}} + \frac{C^m_K}{K_{KAMP}}$	$K_{HAMP} = 6.03*10^{-7}M$ $K_{MgAMP} = 1.38*10^{-2}M$ $K_{KAMP} = 8.91*10^{-2}M$
$P_{GTP} = P_{ATP}$	
$P_{GDP} = P_{ADP}$	
$P_{CoASH} = 1 + \frac{C^m_{H^+}}{K_{HCoASH}}$	$K_{HCoASH} = 7.41*10^{-9}M$
$P_{cit} = 1 + \frac{C^m_{H^+}}{K_{Hcit}} + \frac{C^m_{Mg}}{K_{Mgcit}} + \frac{C^m_K}{K_{Kcit}}$	$K_{Hcit} = 2.34*10^{-6}M$ $K_{Mgcit} = 4.27*10^{-4}M$ $K_{Kcit} = 4.58*10^{-1}M$
$P_{scoa} = 1 + \frac{C^m_{H^+}}{K_{Hscoa}}$	$K_{Hscoa} = 1.1*10^{-4}M$
$P_{fATP} = 1 + \frac{C^m_{H^+}}{K_{HATP}} + \frac{C^m_{K^+}}{K_{KATP}}$	

$P_{fADP} = 1 + \frac{C_{H^+}^m}{K_{HADP}} + \frac{C_{K^+}^m}{K_{KADP}}$ $P_{fAMP} = 1 + \frac{C_{H^+}^m}{K_{HAMP}} + \frac{C_{K^+}^m}{K_{KAMP}}$ $P_{fGTP} = P_{fATP}$ $P_{fGDP} = P_{fGDP}$	

8.3.2 Differential Equations

Mulukutla, B.C., et al., *Multiplicity of Steady States in Glycolysis and Shift of Metabolic State in Cultured Mammalian Cells.* Plos One, 2015. **10**(3).

GLYCOLYSIS

1. Glucose: $\frac{dC_{glc}^c}{dt} = r_{GlcTr} - r_{HK}$
2. Glucose 6-phosphate: $\frac{dC_{g6p}^c}{dt} = r_{HK} - r_{GPI} - r_{G6PD}$
3. Fructose 6-phosphate: $\frac{dC_{f6p}^c}{dt} = r_{PGI} + r_{TA} + r_{TK2} - r_{PFK2} + r_{F2,6BPase} - r_{PFK}$
4. Fructose 1,6-bisphosphate: $\frac{dC_{f16bp}^c}{dt} = r_{PFK} - r_{ALD}$
5. Fructose 2,6-bisphosphate: $\frac{dC_{f26bp}^c}{dt} = r_{PFK2} - r_{F2,6BPase}$
6. Dihydroxyacetone phosphate: $\frac{dC_{dhap}^c}{dt} = r_{ALD} - r_{TPI}$

7. Glyceraldehyde 3-phosphate: $\frac{dC^c_{gap}}{dt} = r_{ALD} + r_{TPI} + r_{TK1} + r_{TK2} - r_{TA} - r_{GAPDH}$

8. 1,3-bisphosphoglycerate: $\frac{dC^c_{1,3bpg}}{dt} = r_{GAPDH} - r_{PGK}$

9. 3-phosphoglycerate: $\frac{dC^c_{3pg}}{dt} = r_{PGK} - r_{PGM}$

10. 2-phosphoglycerate: $\frac{dC^c_{2pg}}{dt} = r_{PGM} - r_{EN}$

11. Phosphoenolpyruvate: $\frac{dC^c_{pep}}{dt} = r_{EN} - r_{PK}$

12. Pyruvate: $\frac{dC^c_{pyr}}{dt} = r_{PK} - r_{LDH} - r_{PYRH} + r_{CMALIC}$

13. Lactate: $\frac{dC^c_{lac}}{dt} = r_{LDH} - r_{MCT}$

PENTOSE PHOSPHATE PATHWAY

14. 6-phosphogluconate: $\frac{dC^c_{6pg}}{dt} = r_{G6PD} - r_{6PGD}$

15. Ribulose 5-phosphate: $\frac{dC^c_{ru5p}}{dt} = r_{6PGD} - r_{RPE} - r_{RPI}$

16. Xylulose 5-phosphate: $\frac{dC^c_{xyl5p}}{dt} = r_{RPE} - r_{TK1} - r_{TK2}$

17. Ribose 5-phosphate: $\frac{dC^c_{r5p}}{dt} = r_{RPI} - r_{PRPPS} - r_{TK1}$

18. Erythrose 4-phosphate**:** $\frac{dC^c_{e4p}}{dt} = r_{TA} - r_{TK2}$

19. Sedoheptulose 7-phosphate: $\frac{dC^c_{s7p}}{dt} = r_{TK1} - r_{TA}$

20. Glutathione: $\frac{dC^{c}_{glutathione}}{dt} = r_{GSSGR} - r_{GSHOX}$

TCA CYCLE

21. Mitochondrial pyruvate: $\frac{dC^{m}_{pyr}}{dt} = r_{PYRH} * \frac{V_c}{V_m} - r_{PDH} + r_{mmalic} - r_{PC} + r_{GPT1}$

22. Mitochondrial Acetyl-CoA: $\frac{dC^{m}_{AcCoA}}{dt} = r_{PDH} - r_{CS}$

23. Mitochondrial Citrate: $\frac{dC^{m}_{cit}}{dt} = r_{CS} - r_{ACON} + r_{CITMAL}$

24. Mitochondrial Isocitrate: $\frac{dC^{m}_{icit}}{dt} = r_{ACON} - r_{IDH}$

25. Mitochondrial Alpha-ketoglutarate: $\frac{dC^{m}_{akg}}{dt} = r_{IDH} - r_{AKGD} + r_{AKGMAL} - r_{GOT2} + r_{GDH} - r_{GPT1}$

26. Mitochondrial Succinyl-CoA: $\frac{dC^{m}_{SCoA}}{dt} = r_{AKGD} - r_{SCOAS}$

27. Mitochondrial Succinate: $\frac{dC^{m}_{suc}}{dt} = r_{SCOAS} - r_{SDH}$

28. Mitochondrial Fumarate: $\frac{dC^{m}_{fum}}{dt} = r_{SDH} - r_{FUM}$

29. Mitochondrial Malate: $\frac{dC^{m}_{mal}}{dt} = r_{FUM} - r_{mmalic} - r_{MDH2} - r_{AKGMAL} - r_{CITMAL} + r_{MALPi}$

30. Mitochondrial Oxaloacetate: $\frac{dC^{m}_{OAA}}{dt} = -r_{CS} + r_{MDH2} + r_{GOT2} + r_{PC}$

NAD/NADH SHUTTLES

31. Mitochondrial Aspartate: $\frac{dC^{m}_{asp}}{dt} = r_{ASPGLU} - r_{GOT2}$

32. Mitochondrial Glutamate: $\frac{dC_{glu}^{m}}{dt} = r_{GOT2} - r_{ASPGLU} - r_{GDH} - r_{GLUH} + r_{GPT1}$

33. Aspartate: $\frac{dC_{asp}^{c}}{dt} = -r_{GOT1} - r_{ASPGLU} * \frac{V_m}{V_c}$

34. Glutamate: $\frac{dC_{glu}^{c}}{dt} = r_{GOT1} + r_{ASPGLU} * \frac{V_m}{V_c} - r_{GLUH} * \frac{V_m}{V_c} + r_{GLS}$

35. Oxaloacetate: $\frac{dC_{OAA}^{c}}{dt} = r_{GOT1} - r_{MDH1} + r_{CLY}$

36. Malate: $\frac{dC_{mal}^{c}}{dt} = r_{MDH1} + r_{AKGMAL} * \frac{V_m}{V_c} + r_{CITMAL} * \frac{V_m}{V_c} - r_{MALPi} * \frac{V_m}{V_c} - r_{cmalic}$

37. Alpha-ketoglutarate: $\frac{dC_{akg}^{c}}{dt} = -r_{AKGMAL} * \frac{V_m}{V_c} - r_{GOT1}$

OTHER EQUATIONS

38. Citrate: $\frac{dC_{cit}^{c}}{dt} = -r_{CITMAL} * \frac{V_m}{V_c} - r_{CLY}$

39. NAD: $\frac{dC_{NAD}^{c}}{dt} = r_{LDH} - r_{GAPDH} + r_{MDH1}$

40. NADP: $\frac{dC_{NADP}^{c}}{dt} = r_{GSSGR} - r_{G6PD} - r_{6PGD} - r_{cmalic}$